Demonstration of the spatial self-trapping of a plasmonic wave

Tintu Kuriakose

To cite this version:

Tintu Kuriakose. Demonstration of the spatial self-trapping of a plasmonic wave. Optics [physics.optics]. Université Bourgogne Franche-Comté, 2018. English. ⟨NNT : 2018UBFCD029⟩. ⟨tel-01987707⟩

HAL Id: tel-01987707
https://theses.hal.science/tel-01987707v1

Submitted on 21 Jan 2019

THÈSE DE DOCTORAT DE L'ÉTABLISSEMENT UNIVERSITÉ BOURGOGNE FRANCHE-COMTÉ

PREPARÉE A L'UNIVERSITÉ DE FRANCHE-COMTÉ

Ecole doctorale n°37

Sciences Pour l'Ingénieur et Microtechniques

Spécialité : **Optique et Photonique**

Par

Tintu KURIAKOSE

Demonstration of the spatial self-trapping of a plasmonic wave

Soutenue publiquement le 12 juillet 2018 devant le jury composé de :

Maria-Pilar BERNAL	Directeur de recherche CNRS, FEMTO-ST	Président
Rachel GRANGE	Professeur, ETH Zurich	Rapporteur
Georges BOUDEBS	Professeur, Université d'Angers	Rapporteur
Gilles RENVERSEZ	Professeur, Université d'Aix-Marseille	Examinateur
Mathieu CHAUVET	Professeur, Université de Franche-Comté	Directeur de thèse

ACKNOWLEDGEMENTS

I would like to express my heartfelt thanks and deep sense of humble gratitude to all those who provided me the possibility to complete my doctoral research at Femto-ST.

First of all I would like to express my deep and sincere gratitude to my thesis advisor, Prof. Mathieu Chauvet, for his guidance, constant support and encouragements. I feel totally indebted to him for introducing me to the field of nonlinear plasmonics and sharing his knowledge and ideas with me. I am extremely thankful to him for being the kind and considerate mentor, providing me all the necessary facilities to conduct experiments and helping me in matters relating to the career and personal life. I am also thankful to him for the confidence he had in me towards the completion of this project and for being the super cool guide!

Besides my advisor I would like to thank rest of my committee members, Prof. Rachel Grange, Prof. Georges Boudebs, Prof. Gilles Renversez, and Dr. Maria-Pilar Bernal, for accepting to be a member of my thesis committee and for their encouragements, insightful comments and questions.

A very special gratitude also goes to my collaborators, Prof. Gilles Renversez and Dr. Virginie Nazabal, for helping me with the theory and the material part of this project. I thank them a lot for being always available for discussions and result analysis. Without their immense support and advices it would not be possible to successfully complete this research project. I am very grateful to Dr. Miguel Angel Suarez and Dr. Jérome Salvi, who worked actively to help me with the SNOM measurements. I am also grateful to Mr. Emmanuel Dordor and Mr. Ludovic Gauthier-Manuel, for the various technical helps rendered.

I am very much indebted to my previous mentors, Prof. Reji Philip of Raman Research Institute, Bangalore and Prof. Chandrasekharan Keloth of National institute of Technology, Calicut for showing me the way to research and for preparing me to do a doctoral study. I am also grateful for the time spent with my NITC and RRI friends. I am specially thanking my friend Suneesh, for his supportive nature and good advices. I wish to thank in addition Priya chechi, Sarayu, Ambili and Shafikka who have willingly helped me out with their abilities during my stay at RRI.

I would like to thank a lot my friends at Femto-ST, Joël, Shanti, Ravinder, Béatrice, Anu-

rupa, Severine, Stefania, Gautier, Phong, Chapal, Raya, Mengjia, Ali, Coffy, Xiaolong, Paul-Antoine, Zhihua, Wentao, Bicky, Venan, Luca, Souleymane, Etienne, Guoping, Alok, Guillaume, Adrien, Moïse and many others. They were more like my family in France. All of them helped me in many situations and were always available for me to enjoy, to discuss problems, and to do a lot of crazy things. I wish to all of them the best to their future endeavours.

I would also like to extend my thanks to the members of the NLO team, Femto-ST. Special thanks to Dr. Thibaut Sylvestre, Dr. Damien Bigourd, and Dr. Hervé Maillotte for useful advices and discussions. It is also my great pleasure to thank Dr. Chauvet's family for their great hospitality and making me feel like at home on the very first day of my stay in France.

My big thanks to Xavier for being a pillar of constant support, for pushing me to think positively, and for helping to improve my technical as well as software skills. I also thank Romain's family for providing a loving environment for me.

Lastly and most importantly, I would like to express my deepest appreciation to my parents, dear sister, and Manish chetai whose unconditional love, care and support have been accompanying me along my life. Without their help and blessings, I would not have reached here.

CONTENTS

3 Nonlinear optical characterization of Ge-Sb-Se planar waveguides 51

4 Demonstration of enhanced self-focusing by plasmons 77

INTRODUCTION

Nonlinear optical effects have a great significance in modern photonic device functionalities including all-optical signal processing, ultra-short pulse generation, wavelength conversion, amplification and many more [1]. One of the nonlinear phenomena that gained considerable attention is the formation of optical solitons [2]. These shape preserving waves have been studied for more than 50 years [3], and it is still an active research field. Though optical nonlinearities and solitons have potential applications in various area, it did not yet become competitive for practical applications. One reason is that the nonlinear effects are weak in nature as they are governed by a photon-photon interactions. Hence very high field intensities or highly nonlinear materials are required to generate significant nonlinear effects [4].

Plasmonics is another flourishing research field that has attracted a lot of attention during the past two decades [5]. A Surface Plasmon Polariton (SPP) [6] at a metal-dielectric interface is one of the most basic encountered plasmonic wave. It is associated with both a collective oscillation of free charges in the metal and an extremely confined electromagnetic wave at optical frequency propagating at the interface. This latter property allows very strong electromagnetic fields to be formed even if the SPP is excited with a moderate power light beam. Plasmons already found applications in various areas such as in ultrasensitive molecular detection and cancer treatment [7]. They are also very promising candidates for the next generation integrated optical devices, generation of new superfast computer chips and invisibility cloak [8].

Merging the fields of plasmonics and nonlinear optics let envision a variety of fascinating and original physical phenomena along with great potential. On the one hand, the strong confinement of light resulting from plasmonic structures can enhance nonlinear effects [4, 9]. In addition, plasmonic excitations would allow a size reduction of devices. On the other hand, the diffraction management property of spatial solitons for which diffraction is compensated by nonlinear focussing effect can be used as an alternative to various geometrical methods for providing lateral confinement of SPPs [10]. Principally, combining plasmon and nonlinear self-focusing is an original concept that has to be demonstrated. Our goal is to realize the first experimental observation of a self-focused plasmonic wave.

Though nonlinear plasmonics is a field of research that has been growing over the past years with foreseen applications [4] such as frequency conversion [11], switching and modulation [12], this field of research is still in its infancy. In particular, first descriptions of one-dimensional nonlinear plasmon–soliton and surface waves at metal/dielectric and dielectric/dielectric interfaces were unveiled more than 35 years ago [13, 14, 15, 16]. A number of theoretical articles deals with plasmon-soliton waves using various modelling methods. For instance, the model for field localization at the metal/dielectric interface predicted in Ref. [13] only applied to a defocusing type of nonlinearity. It was later improved by considering focusing and defocusing Kerr-type nonlinearity as well as TE and TM polarized waves by Maradudin *et al.* [17] and Stegeman *et al.* [18]. Subsequently, a model based on the resonant interaction between a linear plasmon and a spatial soliton was developed [19].

Recent studies considered more elaborated waveguiding structures such as a thin metal film sandwiched between two nonlinear dielectrics [16], nonlinear slot waveguides [20] and strip waveguides [21]. Among them, slot waveguides are favourable configuration to support plasmon-soliton waves. The concept of two-dimensional plasmon-soliton waves in a slot waveguides was first introduced by Feigenbaum *et al.* in 2007 [22]. Most of these studies examine the transverse dimension localization of nonlinear guided waves in metal-dielectric structures. As an improvement to these studies, the localization of plasmon-soliton waves in both transverse and longitudinal directions were theoretically predicted and confirmed numerically by different groups [23, 24, 25]. For our study we have a special interest in structures with an additional dielectric layer between the nonlinear dielectric and the metal film [26, 27, 28]. A detailed theoretical work on such structures can be found in the PhD thesis of Wiktor Walasik [29].

Currently several models based on analytic and numeric calculations proposed to achieve realistic structures [30, 31, 32]. Despite this constant and extensive work on modelling, no experimental evidence has yet been revealed. One reason is that the proposed configurations to generate plasmon-solitons often request a nonlinear refractive index change amplitude too high to be reached in available material. Another practical limitation is due to the large propagation losses associated with plasmons.

In the present study, a specific architecture has been designed, fabricated and studied allowing the first experimental observation of the hybrid coupling between a spatial soliton and a SPP. Precisely, the mechanism that we want to demonstrate experimentally has the following characteristics: i) it offers the formation of self-trapped beam at low power, ii) It represents a new way of SPPs generation, iii) It allows the optical control of plasmon using the nonlinearity. Apart from the fundamental demonstration, plasmon-solitons are potential candidates for important applications.

THESIS OBJECTIVES AND CONTEXT

The main aim of this PhD thesis is to demonstrate the plasmon-soliton coupling that constitutes a new type of hybrid wave. The idea is to form a plasmon polariton wave in a nonlinear material in order to induce an exalted Kerr self-focusing effect so that the plasmon wave is self-trapped. This experimental work is a crucial step towards the demonstration of plasmon-soliton that have been predicted in many publications. The designed structure is based on the fundamental paper of Walasik *et al.* [26] and was developed in partnership with the group of Prof. Gilles Renversez from the Fresnel institute in Marseille. The multilayer structures made of high index chalcogenide glasses were fabricated at the Institute of Chemical Sciences of Rennes in the group of Dr. Virginie Nazabal. The experimental characterizations have been performed at the Femto-st institute under the supervision of Prof. Mathieu Chauvet. Results have also been analysed with models developed in collaboration with the Fresnel Institute.

THESIS ORGANIZATION

The organization of the thesis is as follows. An introduction to nonlinear optics and plasmonics is presented in chapter 1. The first part of this chapter is mainly devoted to nonlinear optics and specifically to the Kerr induced beam self-action effects. Kerr spatial solitons and for completeness, other kinds of spatial solitons are presented. The basic concepts of plasmonics are explained in the second part. This includes historical development of plasmonics, characteristics of SPPs, different excitation mechanisms, applications and challenges. Finally, we introduce the central subject of this PhD thesis - the hybrid plasmon-soliton waves.

The nonlinear material that we chose for our studies is introduced in chapter 2. This chapter begins with a brief introduction of the properties and the applications of chalcogenide glasses. The following section presents the Ge-Sb-Se chalcogenide composition that we considered for this thesis along with its synthesis process. Towards the end of this chapter, fabrication and first optical characterizations of the planar chalcogenide waveguides are presented.

Nonlinear optical characterization of Ge-Sb-Se planar waveguides is described in chapter 3. We investigate the two-photon absorption coefficients of the planar waveguides by the transmission method. An original experimental technique to measure optical nonlinearities in planar waveguides is described in the following section. This technique is based on the beam self-action analysis. The proposed technique applied to characterize the fabricated waveguides at the wavelengths of 1200 nm and 1550 nm is detailed.

We found that the measured Kerr coefficients obtained by this method agree well with the values obtained by other techniques. Moreover, experimental observation of the Kerr spatial solitons, their wavelength dependence and photosensitivity studied in the Ge-Sb-Se waveguides are also discussed in this chapter. Measured large Kerr nonlinearity with low nonlinear and linear absorption losses reveal the great characteristics of our waveguides for plasmon-soliton coupling as well as for integrated photonic devices.

Chapter 4 presents the developments and results on the plasmon-soliton coupling. The design and fabrication of the nonlinear plasmonic structure are presented in the first part. This includes the impact of various parameters of the structure on the hybrid wave. The profile of the plasmonic modes are calculated. A five-layer planar structure designed to limit propagation losses while exhibiting efficient Kerr self-focusing at moderate power is fabricated. The first experimental demonstration of plasmon-soliton coupling is then presented in the second part. The observations reveal an enhanced self-focusing undergone by a self-trapped beam that propagates inside the plasmonic structure. As expected, only TM polarized waves exhibit such a behavior. To provide a better understanding of the underlying mechanism different arrangements are tested. (1+1)-D nonlinear BPM simulations are also performed to back up the experimental results.

At the end of this thesis, a summary of the results and the contributions to the field of research are presented. We also provide some suggestions for future research.

1

FUNDAMENTALS OF NONLINEAR OPTICS AND PLASMONICS

This chapter will provide a general introduction to the topics of nonlinear optics and plasmonics as well as a detailed descriptions of the underlying physics of solitons and surface plasmons. It is divided into two main parts. In the first part, we will introduce the basic concepts of nonlinear optics, optical spatial solitons and its applications. The second part will focus mainly on plasmonics and its applications and more specifically to the characteristics of surface plasmons. Finally, the chapter will conclude by introducing hybrid plasmon-soliton waves as that is at the crossroad of nonlinear optics and plasmonics and is the heart of this subject.

PART I

1.1/ INTRODUCTION TO NONLINEAR OPTICS AND SPATIAL SOLITONS

The invention of laser in 1960 gave birth to a new field of optics called nonlinear optics (NLO) [1] which deals with the study of intense light-matter interactions. Typically, the optical response of a material under low light intensity scales linearly with the amplitude of the electric field. However, at high intensity, the response has a nonlinear behaviour. This leads to a variety of nonlinear optical phenomena's such as the generation of new light frequencies, beam self-focusing, stimulated brillouin scattering, phase conjugation and many more. The applications of NLO can be found in spectroscopic areas to study the physical properties of material and in photonic device functionalities including all-optical signal processing, generation of ultrashort pulses, optical switching, supercontinuum generation, optical computing etc. [33]. Note that nonlinear effects are not only restricted to the field of optics. It plays a significant role in other frequency range such as in electronics (e.g., rectification, modulation, inversion, and harmonic generation), in accoustics (e.g., influence on the propagation of high amplitude jet noise, amplifier or speaker), and in the microwave range [34].

One intriguing physical mechanism offered by the propagation of intense pulses in a nonlinear medium is the formation of optical spatial solitons. These are localized electromagnetic excitation for which the diffraction is balanced by the nonlinear effects [2]. Spatial solitons have potential applications in integrated optics and in communication systems due to its properties such as strong localization and ability to propagate undistorted. However, the formation of spatial solitons based on the Kerr effect necessitates higher peak power since optical nonlinearities are weak in nature. The goal of this thesis is also to limit this drawback by taking advantage of the plasmonic effect.

The primary development of this thesis is focused on the observation and characterization of Kerr spatial solitons formation in nonlinear media. In order to take a closer look at the main principles of beam self-trapping and soliton formation, one has to examine the effects of intensity dependent refractive index in a nonlinear media. We first describe the basic concepts of nonlinear polarization and Kerr effect. Then the following sections present the beam self-action effects, Kerr spatial soliton and some applications.

1.1.1/ MAXWELL'S EQUATIONS

Since nonlinear optical effects belong to a broader class of electromagnetic phenomena, it is useful to start with the Maxwell's equations.

The general form of Maxwell's equations is [35, 36]:

$$\nabla \times E = -\frac{\partial B}{\partial t} \tag{1.1}$$

$$\nabla \times H = J + \frac{\partial D}{\partial t} \tag{1.2}$$

$$\nabla \cdot D = \rho \tag{1.3}$$

$$\nabla \cdot B = 0 \tag{1.4}$$

where E and H are the electric and magnetic field vectors, respectively, and D and B are the corresponding electric displacement vector and the magnetic field induction. J is the current density vector and ρ is the charge density that are sources for the electromagnetic field. In our studies, we will assume $J = 0$ and $\rho = 0$ because we are considering dielectric media. Additionally to Maxwell's equations, the four vector fields are related by the constitutive relations [35]:

$$D = \varepsilon_0 E + P \tag{1.5}$$

$$B = \mu_0 H + M \tag{1.6}$$

where ε_0 is the vaccum permittivity, μ_0 is the vacuum permeability, and P and M are the induced electric and magnetic polarizations. $M = 0$, in an non-magnetic materials. Assuming an instantaneous response of the materials, the polarization describes the electronic response of the materials to the applied electric field. It can be described by the relationship in a linear medium:

$$P = \varepsilon_0 \chi^{(1)} E(t) \tag{1.7}$$

where $\chi^{(1)}$ is the linear susceptibility. This linear description (Eq. (1.7)) is no more accurate when the field intensities become sufficiently high to induce nonlinear effects.

1.1.2/ NONLINEAR POLARIZATION AND KERR EFFECT

In the present section, we introduce briefly the nonlinear polarization equations and describe the type of nonlinearity considered in this thesis.

For high field strengths, the material response to the electromagnetic field become nonlinear, the propagation can be described by a Taylor-series expansion [1]:

$$P = \varepsilon_0[\chi^{(1)} E(t) + \chi^{(2)} E^2(t) + \chi^{(3)} E^3(t) + ...] \tag{1.8}$$

The quantities $\chi^{(2)}$ and $\chi^{(3)}$ are called second and third order nonlinear optical susceptibilities, respectively. As a consequence, the relation between the induced electric polarization and the electric field in a linear and nonlinear dielectric medium is illustrated in the Fig. 1.1. Typically relation between P and E can be considered linear for smaller values of E and becomes nonlinear as E acquires values as high as 10^5 to 10^8 V/m [37]. Depending on the nonlinear optical process $\chi^{(2)}$ or $\chi^{(3)}$ coefficients are requested. For instance, $\chi^{(2)}$ is exploited for second-harmonic generation, sum-and difference frequency generation, optical parametric oscillation, and $\chi^{(3)}$ is used for third- harmonic generation, kerr effect. The details of the process arising from the nonlinear contribution to the polarizations can be found in many textbooks [38, 1]. In this work, we limited ourselves to the study of third order nonlinear optical process and in particular to the Kerr effect which is exploited to induce beam self-trapping.

The nonlinearities of the third order are usually studied in centrosymmetric media, in

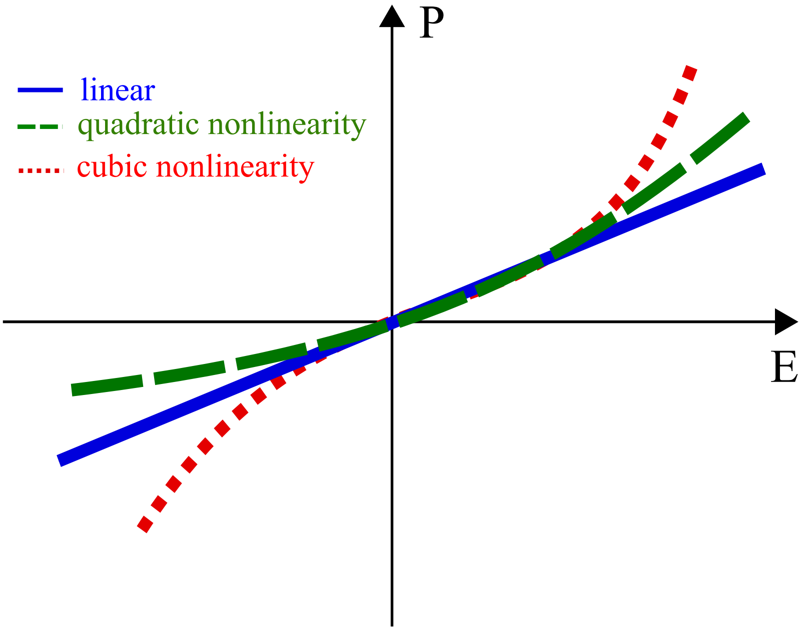

Figure 1.1: Illustration of the relation between P and E in a linear (blue line), quadratic (green dashed line), and cubic (red dotted line) medium.

which $\chi^{(2)}$ is equal to zero. Then the polarization can be denoted as:

$$P = \varepsilon_0[\chi^{(1)}E(t) + \chi^{(3)}E^3(t)] \tag{1.9}$$

From Eq. (1.9), the third order contribution to the polarization is given by:

$$p^{(3)}(t) = \varepsilon_0\chi^{(3)}E^3(t) \tag{1.10}$$

In a general case the field $E(t)$ is composed of several frequency components, but for simplicity, we first consider the case in which the applied field is monochromatic, and is expressed as:

$$E(t) = E_0 cos(\omega t) \tag{1.11}$$

Here E_0 is the amplitude of the wave and ω is its angular frequency. Then, by using the identity $cos^3\omega t = \frac{1}{4}cos3\omega t + \frac{3}{4}cos\omega t$, the third order polarization is given by:

$$p^{(3)}(t) = \frac{1}{4}\varepsilon_0\chi^{(3)}E_0^3 cos3\omega t + \frac{3}{4}\varepsilon_0\chi^{(3)}E_0^3 cos\omega t \tag{1.12}$$

The first term in Eq. (1.12) describes the process of third harmonic generation and the second term in Eq. (1.12) describes a nonlinear contributions at ω to the polarization. This latter contribution leads to an equivalent induce charge experienced by a wave at frequency ω. Combining equations 1.12, 1.11 with the equation for the polarization (Eq.

(1.9)), we get [39]:

$$p \simeq \varepsilon_0(\chi^{(1)} + \frac{3}{4}\chi^{(3)}|E_0|^2)E_0 cos\omega t \tag{1.13}$$

which is similar to the linear relationship between polarization and an electric field of a wave with an additional nonlinear term proportional to the square of the amplitude of the external field, that is the intensity:

$$\chi = \chi_{linear} + \chi_{nonlinear} = \chi^{(1)} + \frac{3\chi^{(3)}}{4}|E_0|^2 \tag{1.14}$$

and:

$$n = (1+\chi)^{1/2} = (1+\chi_{linear}+\chi_{nonlinear})^{1/2} \simeq n_0\Big(1 + \frac{1}{2n_0^2}\chi_{nonlinear}\Big) \tag{1.15}$$

where $n_0 = (1+\chi_{linear})^{1/2}$ is the linear refractive index. The intensity dependent refractive index can be described by a Taylor expansion since $\chi << n_0^2$ and leads to:

$$n = n_0 + \frac{3\chi^{(3)}}{8n_0}|E_0|^2 \tag{1.16}$$

The modification of the refractive index in the presence of a cubic nonlinearity by the following relation [38, 1]:

$$n = n_0 + n_2 I \tag{1.17}$$

where I is the intensity of the incident wave, denoted as $I = \frac{1}{2}n_0\varepsilon_0 c|E_0|^2$, n_2 is the Kerr coefficient and the change in refractive index $(n_2 I)$ can be positive or negative. The order of magnitude of n_2 (in units of cm^2/W) is 10^{-16} to 10^{-14} in glasses, 10^{-14} to 10^{-7} in doped glasses, 10^{-10} to 10^{-8} in organic materials and 10^{-10} to 10^{-2} in semiconductors [37]. The n_2 values are thus small, high beam intensities are then required to observe significant effects. Moreover, a number of physical mechanisms can give rise to the quadratic change in refractive index of a medium: reorientation and redistribution of molecules, electrostriction, deformation of electronic clouds, heating etc. [40].

As we can see in Eq. (1.17), the nonlinear refractive index change is proportional to the intensity of the light which characterizes the Kerr effect or the quadratic electro-optic effect. The Kerr effect can be of two types: 1) in the electro-optic or DC Kerr effect, a DC field induces the refractive index change, 2) for an optical field or AC Kerr effect, the modification of the refractive index is induced by an optical field.

In the time domain, the Kerr effect leads to a phase shift and consequently a frequency shift, and in the spatial domain it leads to beam self-action. If the n_2 coefficient is positive, the Kerr effect leads to beam self-focusing while a self-defocusing is observed if $n_2 < 0$. A further analysis of this kind of intensity dependent refractive index can be found in chapter 4 of Ref. [1]. In this thesis, we will exploit the optical Kerr effect in nonlinear chalcogenide waveguides for beam self-action. This particular configuration is detailed below.

1.1.3/ BEAM SELF-ACTION IN NONLINEAR MEDIA

Beam self-action is an effect in which a beam of light modifies its own propagation by means of the nonlinear response of the medium [1]. Several studies have been demonstrated that when a laser beam irradiates a nonlinear medium many self-action effects such as self-focusing, self-defocusing, self-phase modulation or self-induced transparency can modify the beam propagation [41]. The consequences of these nonlinear effects have an important significance. In beam propagation, self-focusing and self-trapping lead to a lowering of the threshold for other nonlinear process such as stimulated Raman and Brillouin scattering, self-phase modulation, and optical damage [42]. Nonlinear index modification due to the self-action effects impact the design of very high energy laser systems and long distance fibre optical communication systems. In our work, the aim is to manipulate self-accused beams which are detailed in the next subsection.

1.1.3.1/ SELF-FOCUSING AND SELF-DEFOCUSING OF LIGHT

Beam self-focusing is the process in which an intense beam of light modifies the optical properties of a material medium in such a manner that the beam is focused within the nonlinear medium [43]. Materials with large third order nonlinear optical susceptibilities (χ^3) are good candidates for self-focusing experiments. Typically, self-focusing effect compensates the beam divergence due to diffraction. Since the nonlinear variations of the refractive index is mainly dependent on the type of material and on the intensity of radiation, several mechanisms can results in self-focusing. The main cases are Kerr-induced self-focusing [42, 2], plasma self-focusing [44, 45] and accumulated self-focusing [46]. We are interested in the case of Kerr-induced self-focusing.

An example of self-focusing is shown in Fig. 1.2. Consider a monochromatic beam of light travelling from a linear medium (air) to a medium with significant nonlinearity. While initially the wave front is plane parallel, it starts changing shape as the beam propagates in the medium. This is due to the non homogeneous index change induced by the non uniform beam intensity profile. For instance, in a medium with $n_2 > 0$, the refractive index of the medium increases as the light intensity increases. Thus the index value is maximum at the center of the beam and minimum at the periphery areas. The phase velocity is lower in the center than at the edge. Consequently, as the beam traverses the medium, the initial plane wave front gets more and more distorted. With a simple

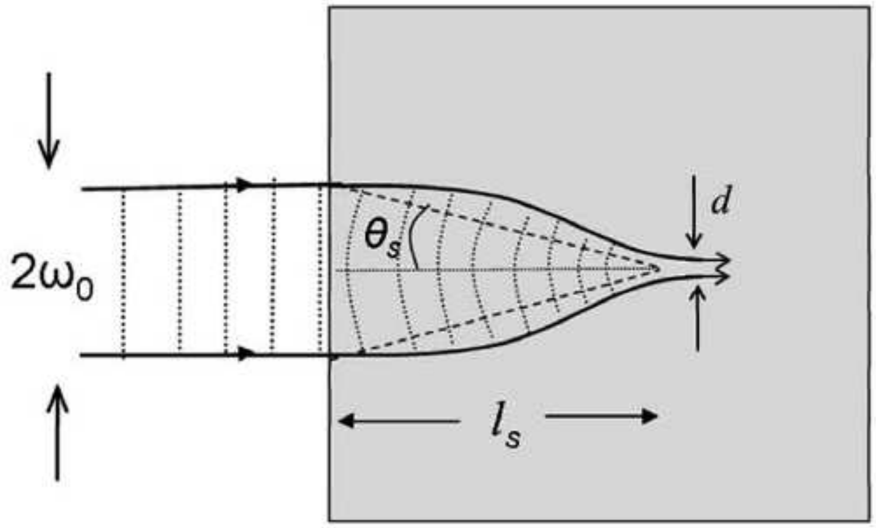

Figure 1.2: Schematic of the self-focusing of a beam with an initial Gaussian profile [43].

ray model, rays propagation direction is always perpendicular to the wave front, as a consequence the beam appears to focus by itself in a medium with $n_2 > 0$.

Since a beam with finite cross section also undergoes diffraction, if the self-focusing action is weaker than the diffracting action, the beam will diffract. Moreover index change being proportional to $n_2|E|^2$, and the diffraction being inversely proportional to the square of the beam radius, as the beam shrinks, both the focusing and diffracting actions become stronger.

Due to the focusing of an initial parallel beam in media with Kerr nonlinearity, the medium can play the role of a collecting lens. This effect has a positive feedback; the increasing intensity in a certain area of the light beam leads to a concentration of the beam in this area and consequently the optical intensities become even higher and hence the self-focusing effect increases further. Note that, an extremely high intensity light resulting from the self-focusing effect can cause possible damages to the optical medium.

Fig. 1.2 also shows the distortion of the wave front inside the nonlinear medium. The parameters that characterize self-focusing are (i) θ_s, the angle of self-focusing (as defined in Fig. 1.2), (ii) linear refractive index n_0, (iii) the nonlinear refractive index $n_2 I$ where I is the beam intensity distribution. The angle θ_s is defined as [1, 43]:

$$\theta_s = \sqrt{\frac{2n_2 I}{n_0}} \tag{1.18}$$

This quantity is known as self-focusing angle and can be interpreted as the angle through which a beam of light deviates as a consequence of self-action effects. In terms of self-focusing angle, we can calculate the distance l_s at which the beam focuses:

$$l_s = \frac{\omega_0}{\theta_s} = \omega_0 \sqrt{\frac{n_0}{2n_2 I}} \tag{1.19}$$

where ω_0 is the beam waist before it enters the nonlinear medium. From Eq. (1.18), we can see that the beam convergence due to self-focusing expressed by θ_s is directly proportional to the square root of the non-linear refractive index. It can be assimilated as focal length l_s and is inversely proportional to the square root of the nonlinear index.

One can use the properties of Kerr induced focusing effect in laser physics. It is the major mechanism behind Kerr lens mode-locking, laser amplification in transparent media, parametric generation and many areas of laser-matter interactions in general. Self-focusing is used in white light generation to achieve high intensities and large interaction lengths at the same time, which is more efficient than a simple focusing with a lens [47]. In addition, focussing effect can be used to measure the magnitude of the Kerr nonlinearity.

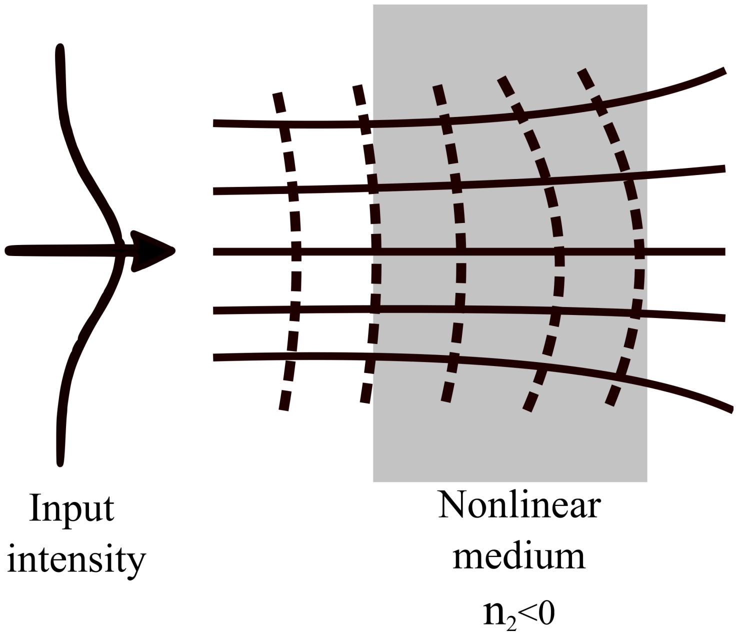

Figure 1.3: Self-defocusing of a beam Gaussian profile in a negative nonlinear medium.

In the case of a negative n_2 nonlinearity a self-defocusing effect (Fig. 1.3) is obtained. Indeed when $n_2 < 0$ the refractive index of the medium decreases with increasing intensity. Thus beam broadening occurrs and hence the nonlinear medium can play the role of a negative lens. This thesis is dedicated to the observation of self-focusing nonlinearity in a Kerr dielectric slab waveguides, the detailed explanations of self-defocusing effect can be found in [3, 43].

1.1.3.2/ SELF-TRAPPING OF LIGHT AND SOLITON FORMATION

A special case of self-action effect is the self-trapping of light. It occurs when a beam of light propagates with a constant diameter as a consequence of an exact balance between self-focusing and diffraction effects [3].

We have seen in the previous section that the beam tends to spread transversely due to diffraction while self-focusing leads to a reduction of the beam diameter. The angular spread θ_d due to linear diffraction for a beam of diameter d is given by [43]:

$$\theta_{dif} = \frac{0.61\lambda_0}{n_0 d} \tag{1.20}$$

The beam divergence due to diffraction is exactly compensated by the beam nonlinear convergent effect due to self-focusing when

$$\theta_{dif} = \theta_s \tag{1.21}$$

By introducing the expressions given by Eq. (1.18) and Eq. (1.20) into this equality, we find that self-trapping occurs if the intensity of the light of the beam is equal to:

$$I_{cr} = \frac{0.37\lambda_0^2}{2n_0 n_2 d^2} \tag{1.22}$$

The corresponding beam power is given by $P_{cr} = \frac{\pi}{4} d^2 I_{cr}$ and the critical power for self-trapping is thus expressed as:

$$P_{cr} = \frac{\pi(0.61)^2\lambda_0^2}{8n_0 n_2} \simeq \frac{\lambda_0^2}{8n_0 n_2} \tag{1.23}$$

The beams of intensity less than this critical value diverges whereas a higher intensity I leads to beam self-focusing that may give beam breakup, where the beam is split up into several narrow beams. When intensity matches the critical value, compensation of diffraction and self-focusing occurs and the resulting beam can maintain its profile undistorted for long distances within the medium and is said to be self-trapped. It act as if the beam generates its own waveguide [43] as depicted in Fig. 1.4. Such beams are also termed as spatial solitons [3].

These localized beams have been demonstrated not only in optics [48] but in many branches of physics including plasma waves [49], sound waves in ^{3}He [50] and Bose-Einstein condensates [51]. The term soliton can also be associated to any solution of a nonlinear equation which represents a wave with an unchanging profile. The signif-

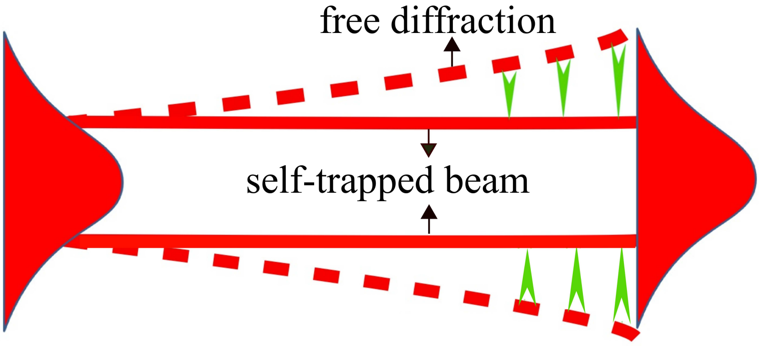

Figure 1.4: Formation of spatial solitons: beam diffraction is compensated by nonlinear self-focusing.

icant properties of solitons are: the maintenance of a constant profile along propagation, possible interaction with other solitons while retaining its identity. Though many nonlinear dispersive partial differential equations can provide soliton solution Korteweg-de Vries equation [52] (describing waves on shallow water surfaces) and the nonlinear Schrödinger equation [53, 2] (describing waves on deep water surfaces and more importantly light waves in optical fibers/ waveguides) are the most important ones. Apart from optical solitons that will be at the center of our work, I would like to mention soliton phenomena that naturally form: solitary water waves, on the surface or undersea-internal waves (Fig. 1.5(a)) and atmospheric solitons such as Morning glory clouds that can form vast linear roll clouds produced by pressure solitons travelling in a temperature inversion [54] (Fig. 1.5(b).

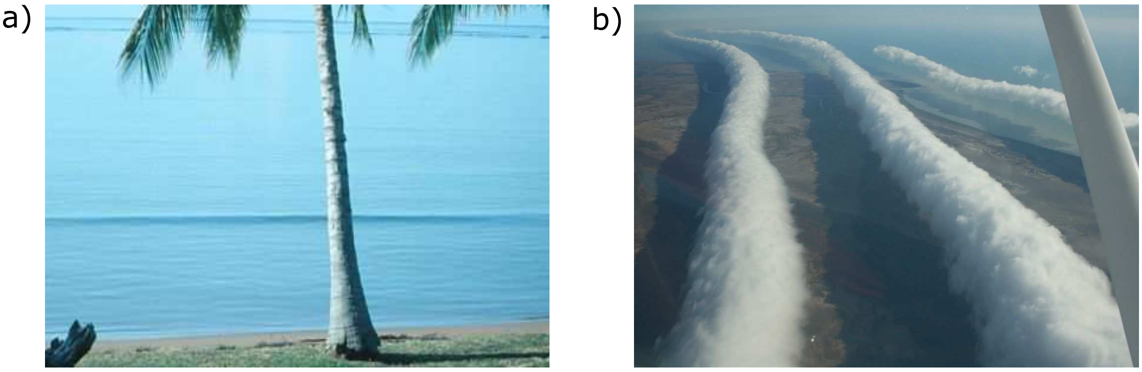

Figure 1.5: Examples of solitons found in nature, (a) solitary wave approaching the beach in the lagoon of Molokai, Hawaii [55], (b) Morning glory cloud formation in the Gulf of Carpentaria, Australia [54].

A temporal solitons can also be formed when group velocity dispersion is counteracted by self-phase modulation effects. The pulse or the beam then propagates without change in its shape and is said to be self-localized or self-trapped.

While optical solitons have been intensively studied in both spatial and temporal domain, soliton research in spatial domain has attracted a lot of attention due to its ease to conduct sophisticated experiments in a laboratory environment that offers a precise control over almost every parameter. In addition, these localized waves in space can exhibit many fascinating features such as particle like interactions during collisions. Apart from the fundamental applications, spatial solitons have been proposed for variety of applications including waveguiding and beam splitting, optical interconnects, frequency conversion, image transmission, gateless computing, and soliton based navigation [56].

A number of nonlinear mechanisms can support spatial solitons, for example: photorefractive effect, parametric $\chi^{(2)}$ mixing phenomena, non-linearities in liquid crystals and polymers and also the saturable non-linearities of two level systems [57]. Such diversity of non-linear effects and the discoveries of spatial solitons in different systems and associated phenomena have stimulated the interest in spatial solitons. This thesis concentrates on spatial optical solitons in media exhibiting Kerr non-linearity, readers interested in temporal solitons can refer to Agrawal [38] and Trillo [3].

1.1.4/ KERR SPATIAL SOLITONS

The first optical solitons observed in gases [58], fluids [48], and solids [59] are based on the third order nonlinear effect. The propagation in a Kerr medium can be represented by the Eq. (1.17). Since Kerr nonlinearity is weak, high peak power lasers are necessary to induce sufficient perturbations in the material. Peak power is on the order of 1 GW/cm^2 [59]. The high peak intensity required somehow limits the possibility to employ such effect in optical communication system. This can be reduced by using a proper material with a large Kerr nonlinearity. It is worth mentioning that the self-trapped beams are unstable in bulk media (represented by the Eq. (1.23)) and leads to catastrophic self-focusing. However, the stability can be achieved when diffraction is limited to one spatial dimension (1-D solitons) such as in planar waveguides. This thesis devoted to the characterization and observation of spatial solitons in planar waveguides.

For the theoretical solution of a 1-D soliton, we thus consider the condition where the beam is allowed to vary only in one transverse dimension, x. A planar waveguide is suitable in that point. The nonlinear Schrödinger equation model the propagation in the z direction of an optical beam in the presence of an intensity dependent refractive index [60]:

$$2ik\frac{\partial E}{\partial z} + \frac{\partial^2 E}{\partial x^2} + 2k^2\frac{n_2}{n_0}|E^2|E = 0 \qquad (1.24)$$

where E is the amplitude of the electric field, n_0 and n_2 are the linear and nonlinear index coefficients defined by Eq. (1.17) and k is the wave vector in the medium. The first term accounts for the diffraction and the second term describes the nonlinear contribution to the refractive index. The solution of a fundamental soliton propagating along the z axis is given by [59]:

$$E(x,z) = \frac{1}{ka_0}\Big(\frac{n_0}{n_2}\Big)^{1/2} exp\Big(\frac{iz}{2ka_0^2}\Big) sech\Big(\frac{x}{a_0}\Big) \tag{1.25}$$

where a_0 is the beam width. The sech profile is typical of fundamental solitons.

The integrated intensity over the beam leads to soliton power p_s and denoted as:

$$p_s = \int |E|^2 dx = \frac{n_0}{n_2}\frac{2}{a_0k^2} \tag{1.26}$$

The total power required to form a fundamental soliton is given by :

$$p_t = \frac{2n_0\omega}{n_2a_0k^2} \tag{1.27}$$

where ω denotes the transverse mode size. This result is valid if ω is much smaller than the soliton width a_0. At this power level, an effective soliton propagation can be observed in a planar waveguide which is restricted to only x dimension. Higher order soliton solutions can also exist when the beam is the square of an integer number (N) times the fundamental soliton power (N^2P_t) [61]. Such beam don't have a constant shape, but have a profile that varies periodically along propagation. The period of this evolution is the so-called soliton period.

1.1.5/ OTHER KINDS OF SPATIAL SOLITONS

A) CONTINUOUS, DISCRETE AND CAVITY SOLITONS

Spatial solitons can be classified according to the configurations in which they exist. Such a way one can distinguish solitons in continuous, in discrete media and in optical cavities.

Solitons in continuous medium such as in optical crystals, liquid or even in gas [48] are the first who have been discovered. They encompass the one studied in this work.

In the second case, discrete solitons form in a medium in which periodic modulation of the refractive index is present such as waveguide arrays and photonic crystals [62]. They form due to a balance between discrete diffraction and nonlinear effect. The pioneering experimental results of 1-D discrete solitons observed in an AlGaAs waveguide arrays by Einsenberg *et al*. [63] is shown in Fig. 1.6. One of the special property of discrete medium is that complete diffraction management is possible (diffraction can be cancelled, diminished or reversed). As a consequence either focusing or defocusing nonlinearities can be exploited to form such solitons.

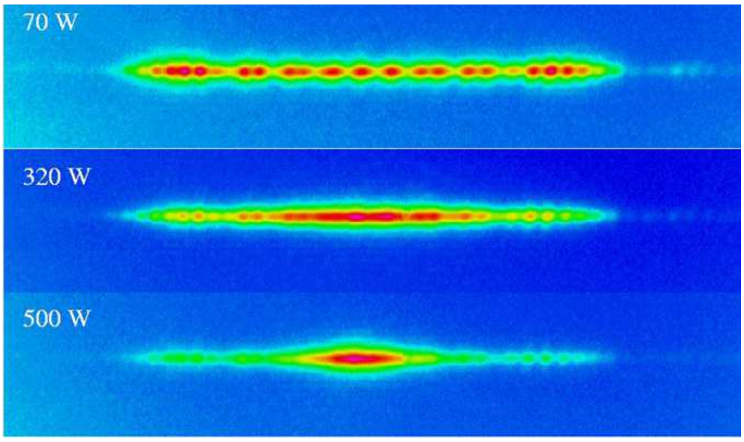

Figure 1.6: Experimental demonstration of a 1-D discrete optical soliton in a 4 mm long AlGaAs semiconductor waveguide arrays for different powers. At low power, the beam undergoes linear diffraction, but at high power, formation of a descrete soliton occurs. Images taken from Ref. [56].

Finally, optical cavities can also support solitons [64] which are peaks of self-localized light in an optical cavity (Fig. 1.7). The main features of cavity solitons are bistability (on/off), independent on each other and their position on the transverse plane of the cavity can be controlled. In addition, these localized bright spots driven in optical cavities could be bits for parallel processing of optical communication system [3].

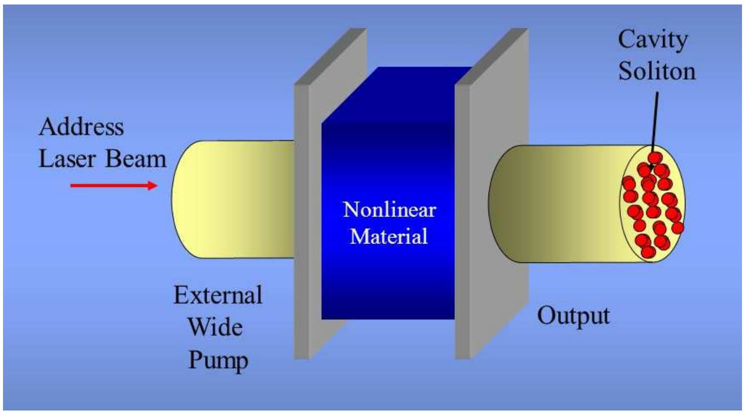

Figure 1.7: Cavity solitons: the injection of laser pulses into an optical cavity containing a nonlinear material creates localized intensity peaks at the output. Figure taken from Ref. [65].

B) BRIGHT, DARK AND VORTEX SOLITONS

Spatial solitons are also classified depending on their transversal shape (Fig. 1.8): bright spatial solitons propagate as non-diffracting bright spots developed as earlier in the document.

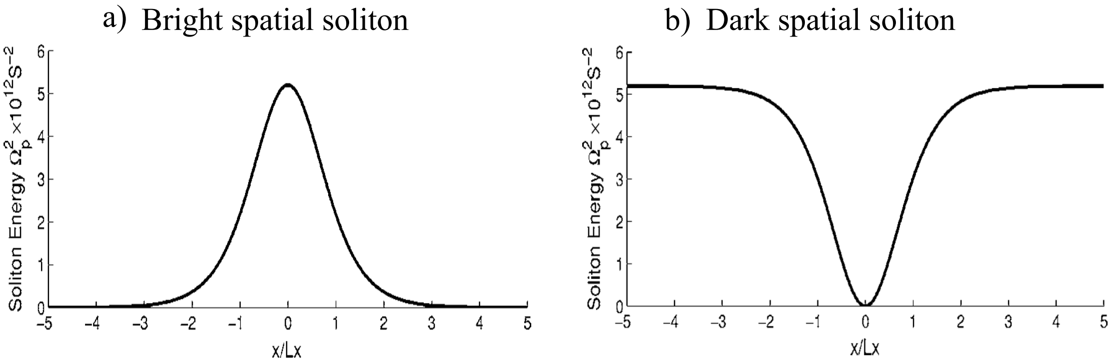

Figure 1.8: Bright and dark spatial soliton intensity profiles. Figure taken from Ref. [66].

To the contrary, dark solitons present a dark spot of finite width across the transverse profile surrounded by a bright background. This dark region is due to a π phase shift located where the field value is zero. This second class of solitons requires a self-defocusing media to guide self-trapped dark beams [67].

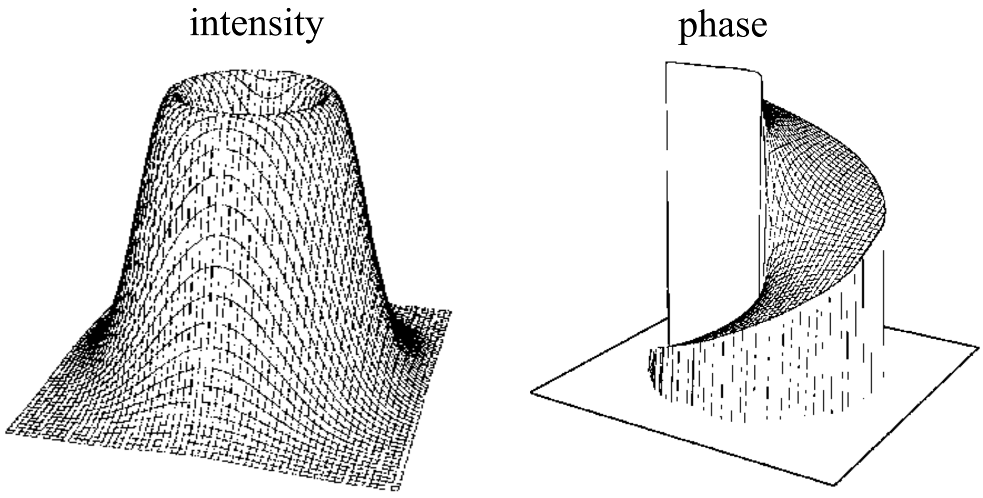

Figure 1.9: Intensity and phase distribution for an optical vortex soliton. Figure taken from Ref. [68].

A third category of solitons known as optical vortex solitons (Fig. 1.9) consists of a circularly symmetric dark hole surrounded by a bright uniform background. This particular variety of solitons possess a helicoided angular phase shift of $\pm 2\pi$, thus optical vortex solitons propagate without changing its transversal shape but with a phase rotation around the center of symmetry [69]. Therefore, vortex solitons can be considered as (2+1)-D dark solitons and they can be observed in a media with defocusing nonlinearity. These bright, dark and vortex spatial solitons could find application in guided wave optics especially in all-optical logic and switching devices [67].

C) PHOTOREFRACTIVE AND QUADRATIC SOLITONS

The next important classification of spatial soliton relies on the type of non-linearities by which they are supported. Apart from the Kerr solitons, the two major classes of solitons discovered in terms of nonlinear mechanisms are photorefractive solitons and quadratic solitons.

The former type of spatial soltions were discoverd in the early nineties [70]. The photorefractive effect is the main mechanism behind the formation of these solitons. The photorefractive effect starts with the absorption of light and subsequent charge generation. Then these charges move and establish a local space-charge fields. Finally a linear electro-optic effect is requested to change the index of refraction proportional to the local fields [57]. It can be observed in noncentrosymmetric dielectric (LiNbO$_3$ and KNbO$_3$) and semiconductors (GaAs, InP) with second-order non-linearities. A peculiarity of photorefractive solitons is that very low power (microwatt-level) is sufficient to induce them. Moreover, the induced waveguide can be later used to guide other beams at wavelengths that are photorefractively less sensitive. This makes them attractive for waveguiding and steering applications [56]. In addition, photorefractive soliton induced waveguides can be used for device applications such as directional couplers and high-efficiency frequency converters [71, 72].

The quadratic solitons were predicted in the 1970s [73] and were demonstrated experimentally in 1995 [74]. In this case, beam self-trapping mechanism arises in the material due to second harmonic generation, which is based on χ^2 effect in noncentrosymmetric materials such as KDP, LiNbO3 and BBO [75]. When light at a certain frequency ω (fundamental fields) propagates in such materials, a polarization field excites a field that propagates with twice the frequency (second harmonic) of the input beam. Hence, both frequencies are present at the output of the non-linear crystal. The phase velocities of these two beams are different due to dispersion. Due to this phase mismatch the optical power is converted from ω to 2ω and then reconverted back from 2ω to ω via processes called up- and down-conversion. This coupling induces a large phase deformation and thus modifies the propagation of both beams. A balance between diffraction and nonlinear phase shift is required for the soliton formation [76].

There are other families of nonlinearities via which spatial soliton can generate. For example, resonant nonlinear effects in atomic vapors, nonlinear upconverted photobleaching in dye-doped polymers, orientational and thermal nonlinear effects in liquid crystals and pyroelectric effects etc [77, 56].

SUMMARY

So far we have discussed the basics of NLO and the formation of different kinds of optical spatial solitons. Besides these Kerr induced effects, intense light matter interactions contributes to several phenomena and has made a great impact on today's daily life. For instance, the relevance of NLO can be found in optical communication, sensors, commercial lasers, medicine, military, scientific instrumentation, high-resolution spectroscopy and many more [33]. However, most of these applications are limited by the requirement of high energy, highly nonlinear material and the device size constraints related to the wavelength of light. One possible solution to overcome the challenges in the field of NLO is to use plasmonic effects. The role of plasmonics for enhancing optical nonlinearity is detailed in the following sections.

PART II

1.2/ INTRODUCTION TO PLASMONICS

A second domain directly linked to the subject of this thesis is plasmonics. This field for which first results were reported in the early 1900 deals with the interactions of electromagnetic wave with conduction electrons in metal [7]. The basis of plasmonics is about the excitation of Surface Plasmons (SPs) that are collective charge oscillations on a metal surface. SPs can take the form of Surface Plasmon Polaritons (SPPs) as well as Localized Surface Plasmons (LSPs). The combined excitation of light and surface plasmons at the interface of a metal-dielectric is called SPPs and the excitations of SPs in bounded geometries such as metallic nano particles are called LSPs.

The studies of plasmons based structures and devices have received a lot of attention in the past few years due to its peculiar properties and applications in optics such as surface-enhanced Raman spectroscopy, magneto-optic data storage, solar cells and to construct sensors for detecting biologically interesting molecules [78]. Many of the advances in these areas result from the unique properties of SPPs such as the ability to confine light to nanoscale dimensions that are far beyond the diffraction limit [5]. The properties of SPs, especially their interaction with light can be modified by altering the structure of a metal surface. This leads to the miniaturization of photonic circuits with length scales much smaller than those currently achieved [78]. Furthermore, concentration of light in sub wavelength structures can enhance the electric field and boost non-linear phenomena which is one ambition of the present work.

In this thesis we will exploit the strength of plasmonics for enhancing the Kerr optical nonlinearity. More specifically, we will study the coupling of propagating SPs and spatial solitons. To understand the concept of hybrid plasmon-soliton waves it is thus important to understand the properties of SPPs. Here we provide an overview of the properties of SPPs. We begin by a historical review of the field of SPs followed by introducing the underlying physics. Then excitation schemes along with applications and challenges of plasmonics are presented.

1.2.1/ HISTORICAL DEVELOPMENT OF SURFACE PLASMONS

The first observation of propagating SPs dates back from 1902, when Robert. W. Wood illuminated a metallic diffraction grating with polychromatic light and found a pattern of unusual dark and bright bands in the reflected light, which he refered as anomalies [79]. The theoretical treatment of these anomalies was later suggested by Lord Rayleigh in 1907 [80].

Several experimental and theoretical studies were carried out on electron energy losses in glasses and on thin foils in the fifties [81, 82, 83, 84]. In 1956, David Pines theoretically described that the energy losses were due to the collective oscillations of free electrons in the metal and called these oscillations as ’plasmons’ [82]. The same year Fano associated Wood’s anomalies with the excitation of electromagnetic surface waves on the diffraction grating [85]. Subsequently, Rufus Ritchie proposed the concept of SPs in the context of electron energy loss in thin films [83]. The experimental observation of the excitation of surface collective charges were demonstrated by Powell and Swan [84] and the term ”surface plasmons” was given by Stern and Ferrell [86].

Major progress in the study of SPs was made by Otto and Kretschman in the late sixties [87]. They proposed the optical excitation of SPs on metal films by attenuated total reflection. Thereafter, Stephen Cunningham *et al.* introduced the term SPP for the coupling between oscillating electrons of surface plasmons and electromagnetic field in 1974 [6].

The next section presents the underlying physics of SPPs, involving excitation of SPPs, dispersion relations, propagation behaviour and the length scales of SPPs.

1.2.2/ CHARACTERISTICS OF SURFACE PLASMON POLARITONS

SPP is an electromagnetic surface wave that travels along the interface between a metal and a dielectric material. The surface electromagnetic wave is linked with surface charges

[88]. In order to describe the properties of SPPs, it is helpful to start from the excitation of surface charges.

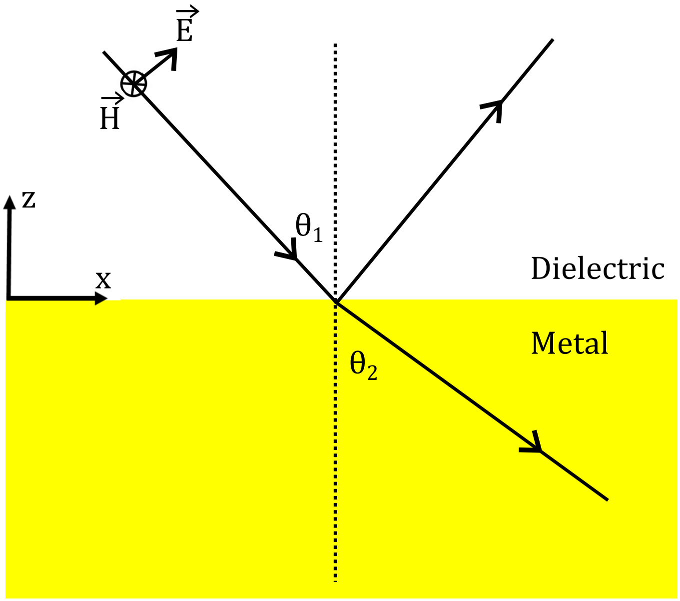

Figure 1.10: Illustration of a TM polarized light incident upon a planar interface between a metal and a dielectric at an angle of incidence θ_1. $\vec{E}$ and $\vec{H}$ are the electric and magnetic field components of the incident wave respectively.

Consider a TM polarized light (P-polarization, electric field parallel to the plane of incidence and magnetic field perpendicular to the plane of incidence) that reaches a smooth planar dielectric-metal interface at an angle θ_1 (Fig. 1.10). The momentum of the incident wave in the dielectric medium is $\hbar k_d$, where $\hbar$ is the Dirac constant and k_d is the wave vector in the dielectric, given by $k_d = 2\pi n_d/\lambda$, with n_d the dielectric refractive index. When the wave hits the interface, the reflected wave propagates an angle equal to the incident angle, thus the photon momentum is conserved. The wave transmitted in the metal propagates in the direction given by θ_2 (See Fig. 1.10). The transmitted photon momentum is $\hbar k_m$, where $k_m = 2\pi n_m/\lambda$, with n_m the refractive index of the metal, and the momentum component along the x direction has to be conserved, i.e., $k_{dx} = k_{mx}$, (it is also because of the continuity equation: the field components (electric and magnetic) parallel to the interface have to be continuous), where $k_{dx} = k_d \sin\theta_1$ and $k_{mx} = k_m \sin\theta_2$, and we obtain:

$$n_d \sin\theta_1 = n_m \sin\theta_2 \tag{1.28}$$

This is called Snell's law. In general the refractive index of the dielectric n_d is larger than that of the metal n_m, thus $\theta_2 > \theta_1$ with the maximum value for θ_2 being 90°. The largest value for θ_1 to have a transmitted beam is thus equal to the critical angle θ_c, Which is given by:

$$\sin\theta_c = \frac{n_m}{n_d} \tag{1.29}$$

A wave with incident angle beyond θ_c is totally reflected. For a TM polarized wave, the z-component of the oscillating electric field generates surface charges at the interface between the metal and the dielectric and these surface charges undergo collective oscillations.

To summarize, as the incident angle increases toward the critical angle, the transmitted beam diminishes in intensity while the reflected beam grows stronger. At all angles greater than critical angle, total reflection is achieved, in which all of the light is reflected back into the dielectric medium. Although the light no longer propagates into the metal, there is a small amount of penetration of the reflected light across the interface, which then propagates parallel to the surface, creating an electromagnetic field in the metal immediately at the interface. This field is evanescent because its amplitude decreases exponentially with increasing distance from the interface. This evanescent field is at the origin of the charges that undergo collective oscillations and give rise to the SPs. Note that, the s-polarized light (TE mode- electric field perpendicular to the plane of incidence) will not create SPs at the metal dielectric interface since it has no field component perpendicular to the interface, only TM waves can excite plasmons.

We have seen that SPP is an electromagnetic excitation existing at the interface between a conductor and a dielectric material and evanescently confined in the direction perpendicular to the interface [5]. To introduce the main parameters characterizing SPP, let us consider a metal-dielectric interface with two evanescent waves decaying exponentially into both neighbouring media as shown in Fig. 1.11. The plane $z = 0$ separates the metal from the dielectric medium. Since the SPP supported at the planar interface is TM in nature it possesses the non zero field components $E_x, E_z, \text{and } H_y$. The surface charge distributions and electric field components of the SPP propagating in the x direction are also schematically shown in Fig. 1.11.

The tangential components of E and H are continous at $y = 0$ according to the continuity of the electromagnetic fields, i.e., the field components E_x and H_y are continuous at the interface. The SPP electric field for $z > 0$ space is filled by a lossless dielectric material having a positive permittivity, ε_d and the space $z < 0$ is filled with a metal having a negative permittivity, ε_m. According to Ref. [89], the electric field components are given by :

$$E(z > 0) = (E_x^0, 0, E_z^d).e^{i(k_{spp}x-\omega t)} \exp(-z\sqrt{k_{\text{spp}}^2 - \epsilon_d k_0^2}), \tag{1.30}$$

$$E(z < 0) = (E_x^0, 0, E_z^m).e^{i(k_{spp}x-\omega t)} \exp(z\sqrt{k_{\text{spp}}^2 - \epsilon_m k_0^2}), \tag{1.31}$$

where E_x^0 is the amplitude of the tangential electric field component while $E_z^{d(m)}$ is the perpendicular component of the electric field in the dielectric (metal). k_{spp} is the propagation constant of the SPP mode propagating in the x direction. k_0 is the light wave vector in

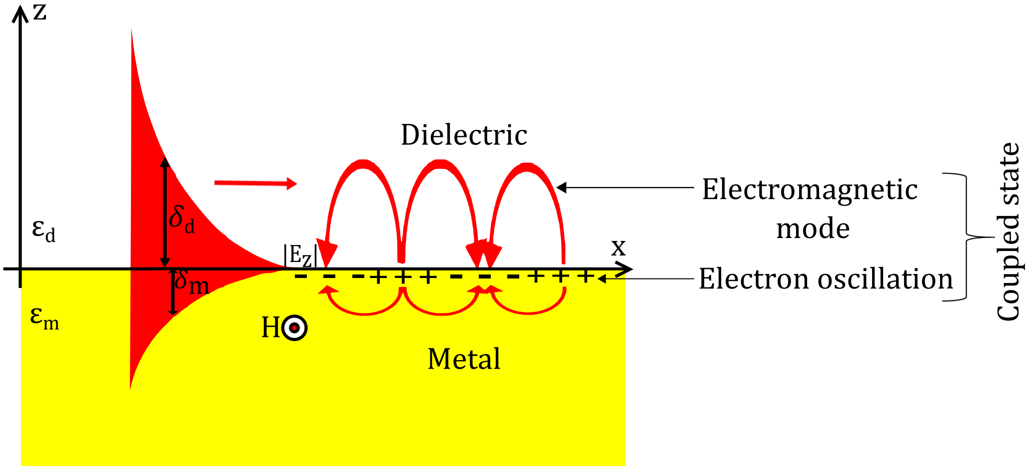

Figure 1.11: Illustration of the electromagnetic field components of a SPP supported by metal and dielectric interface. The mode is TM with components of the electric field normal to the interface (z-axis) and along the x-axis. The electric field distribution is maximum near the surface and decays exponentially in the direction normal to the interface (z).

free space denoted as $k_0 = 2\pi/\lambda_0$, λ_0 is the wavelength in free space and ω is the angular frequency. Since the field components should satisfy Coulomb's law $\nabla.E = 0$, the field components perpendicular to the interface can be related to the tangential one:

$$E_z^d = \frac{ik_{spp}}{\sqrt{k_{\text{spp}}^2 - \epsilon_d k_0^2)}} E_x^0 \text{ and} \tag{1.32}$$

$$E_z^m = -\frac{ik_{spp}}{\sqrt{k_{\text{spp}}^2 - \epsilon_m k_0^2)}} E_x^0 \tag{1.33}$$

Many of the SPPs characteristics can be understood by examining their dispersion relation i.e., the relation between the angular frequency (ω) and the wave vector (k_{spp}) of SPP modes. The dispersion relationship for SPP can be found in a number of ways. Using the continuity boundary condition for the electric field displacement components along z : $\epsilon_d E_z^d = \epsilon_m E_z^m$. From equations (1.32) and (1.33), we thus deduce:

$$k_{spp} = k_0 \sqrt{\frac{\varepsilon_m \varepsilon_d}{\varepsilon_m + \varepsilon_d}} \tag{1.34}$$

For the SPP to exist, it requires that the square root expressions in equations 1.30, 1.31 and 1.34 to have a positive real part. Since we assumed earlier that $\epsilon_d > 0$ and $\epsilon_m < 0$ we thus have

$$\varepsilon_d \varepsilon_m < 0 \tag{1.35}$$

As a consequence we also need:

$$\varepsilon_d + \varepsilon_m < 0 \tag{1.36}$$

The relations Eq. (1.35) and Eq. (1.36) determine the frequency interval within which SPPs are allowed. For most metals and dielectrics, this condition is satisfied in the long wavelength part of the visible and in the infrared. The permittivity ε_m is expressed by the Drude model [5]:

$$\varepsilon_m = 1 - \frac{\omega_p^2}{\omega^2} \tag{1.37}$$

Here ω_p is the plasma frequency of the metal. In general, light of frequency below the plasma frequency is reflected by a material because electrons in the material can screen the electric field of the light whereas the light of frequency above the plasma frequency is transmitted because the electrons cannot respond fast enough to screen it. For most metals the plasma frequency is in the ultraviolet wavelength region.

By considering the Eq. (1.37) for ε_m in Eq. (1.34), we can deduce the dispersion relation of SPP mode supported by a lossless Drude metal-dielectric interface,

$$K_{spp} = k_0 \sqrt{\frac{\varepsilon_d (1 - \frac{\omega_p^2}{\omega^2})}{\varepsilon_d + 1 - \frac{\omega_p^2}{\omega^2}}} = \beta \tag{1.38}$$

Fig. 1.12 shows the dispersion relations of the SPP wave described by Eq. (1.38). The dispersion relationship between frequency and wave vector of the photon is given by $k_0 = \omega/c$, c being the speed of light. Consider a medium having a relative permittivity ϵ_d and thus refractive index $n_d = \sqrt{\epsilon_d}$. In this case, the dispersion relation for the photon is given by $k = n_d k_0 = \sqrt{\epsilon_d}\frac{\omega}{c}$, it is thus represented by a straight line. The black dashed line represents the photon propagation in the dielectric and the blue solid line is the SPP dispersion curve.

We can see that the propagation constant of the SPP is larger than that of the light in the dielectric. This leads to two important facts: 1) special momentum matching schemes are required for the coupling of SPPs modes (since SPP modes having greater momentum than light of same frequency ($k_{spp} > \sqrt{\epsilon_d}\frac{\omega}{c}$), one cannot use incident light to couple these modes, a momentum enhancing scheme is needed), and 2) it results into better confinement of light than in dielectrics. To understand this point, consider the following equation:

$$|k_{d(m)}|^2 = \beta^2 - k_0^2 \varepsilon_{d(m)}, \quad \delta_{d(m)} = |k_{d(m)}|^{-1} \tag{1.39}$$

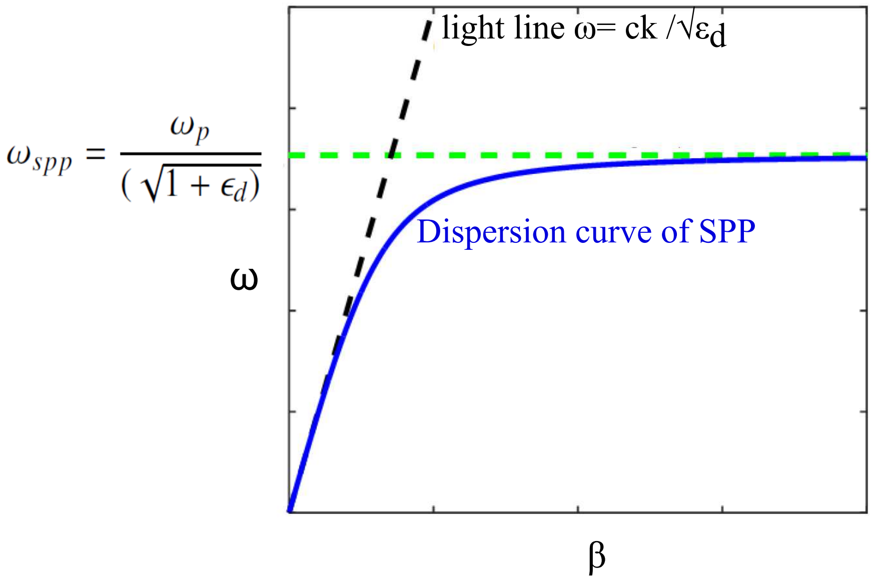

Figure 1.12: Dispersion curve of surface plasmon polariton at a metal dielectric interface without considering the metal loss.

Here, $k_{d(m)}$ are the wave vector components perpendicular to the interface of the dielectric (metal) medium. $\delta_{d(m)}$ are the evanescent decay lengths of the fields perpendicular to the interface. Since ε_m is negative, the penetration depth of light into the metal is always smaller than the one into the dielectric. As depicts in Fig. 1.12, for a small frequency (ω), β is very close to $k_0\sqrt{\epsilon_d}$ and the dispersion curve follows the light line very closely. In this case k_d is very small and inversely δ_d is large. Consequently, the SPP wave extends deeper into the dielectric. As ω increases, the difference between β and $k_0\sqrt{\epsilon_d}$ also increases which means that k_d becomes larger and δ_d becomes smaller. This results a better confinement of light in the dielectric side.

Note that, when ω approaches the surface plasmon resonance frequency (ω_{spp}), β approaches infinity. It corresponds to $\varepsilon_d + \varepsilon_m = 0$, the plasmon frequency is thus given by,

$$\omega_{spp} = \frac{\omega_p}{(\sqrt{1+\varepsilon_d})} \tag{1.40}$$

This condition is known as surface plasmon resonance (SPR). Near the SPR frequency, the plasmonic wave greatly slows down and the extent of field on either side of the interface becomes vanishingly small.

Another important characteristic parameter of SPP is the propagation length δ_{SPP} which is defined as the distance over which the intensity decreases to $1/e$ of its starting value.

It is given by,

$$\delta_{SPP} = \frac{1}{2\beta i} = \frac{c}{\omega}\left(\frac{\epsilon_{mr}+\epsilon_d}{\epsilon_{mr}\epsilon_d}\right)^{3/2}\frac{\epsilon_{mr}^2}{\epsilon_{mi}} \tag{1.41}$$

where ϵ_{mr} and ϵ_{mi} are the real and imaginary parts of the dielectric function of the metal respectively. It shows that the propagation length is mainly dependent on the dielectric constant of the metal and the incident wavelength.

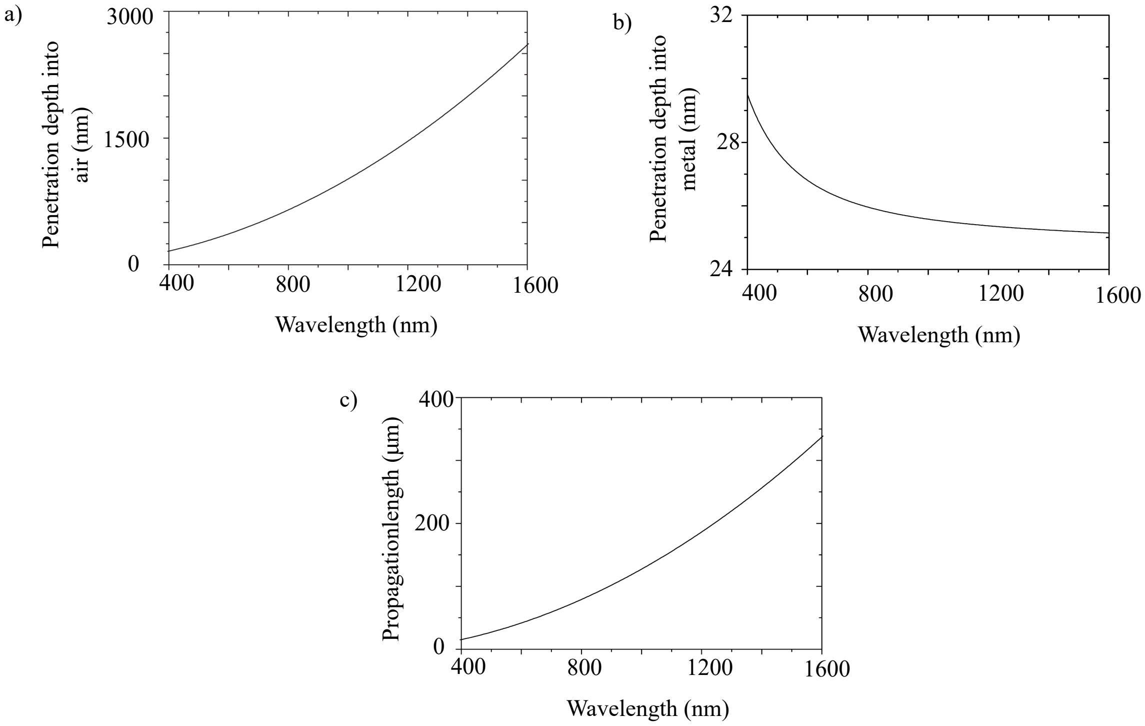

Figure 1.13: Penetration depth into the (a) dielectric, (b) metal and (c) propagation distance of the SPP wave as a function of wavelength. Figure taken from Ref. [90].

To provide a better understanding, the penetration depth and propagation distance as a function of wavelength for silver/air interface is shown in Fig. 1.13. We can see that the penetration depth of SP wave into the dielectric (Fig. 1.13(a)) is on the order of few micrometer and it increases with wavelength. On the other hand, the penetration depth of SP into the metal decreases with the wavelength (Fig. 1.13(b)) and is a few tens of nanometer. The propagation distance (Fig. 1.13(c)), is a few hundreds of microns for longer wavelengths and it can be much shorter for short wavelengths due to a strong attenuation in the metal. Moreover, as wavelength is increased, the SP is less confined and hence the propagation distance increases.

1.2.3/ EXCITATION OF SURFACE PLASMON POLARITONS

In the previous section we have discussed the characteristics of SPPs. Here we present some general techniques to excite plasmonic modes with electromagnetic waves. As shown in Fig. 1.12, the wave vector of SPP is larger than the light wave vector in the dielectric medium. Thus, wave vector matching has to be fulfilled when excitation of plasmon is induced by light illumination. The excitation mechanisms are highly dependent on the geometry of the plasmonic structures as well as the polarization state of the incident light. The commonly used configurations to resolve this wavenumber mismatching are prism couplers [91, 92], grating couplers [91, 92] , and fibre/waveguide couplers [93, 94, 95, 96].

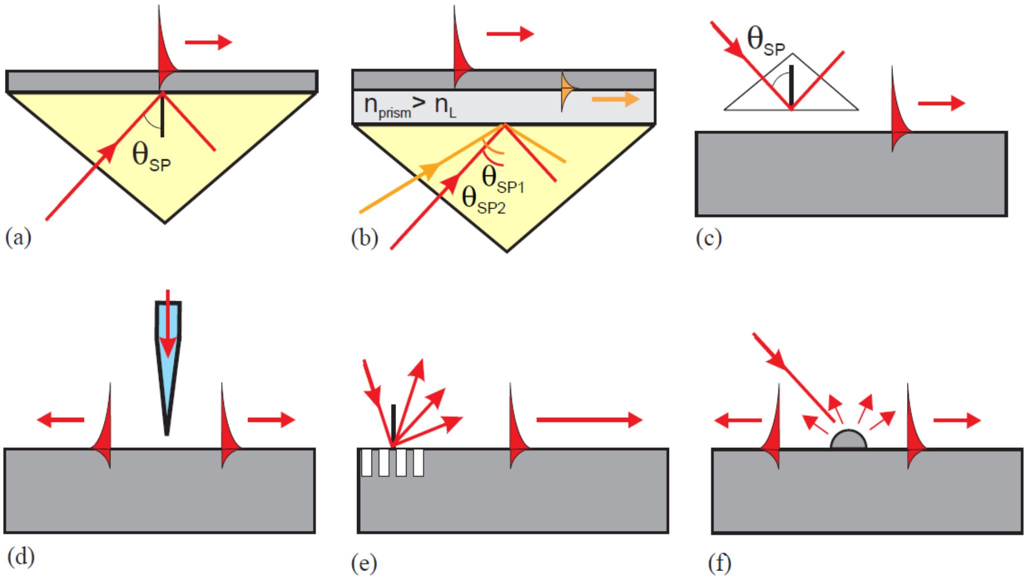

Figure 1.14: SPP excitation configurations: (a) Kretschmann geometry, (b) two-layer Kretschmann geometry, (c) Otto geometry, (d) excitation with a SNOM probe, (e) diffraction on a grating (f) diffraction on surface features, (g) waveguide coupler, and (h) fiber-optic coupler. Figures (a-f) taken from Ref. [92].

The prism based system can be applied in different configurations. In the Kretschman configuration (Fig. 1.14(a)), a metal film is deposited directly on top of a prism base, and it is illuminated through the dielectric prism at an angle of incidence greater than the critical angle for total internal reflection [87]. When the light couples to the SPPs, a sharp minimum can be observe in the reflectivity since the light energy is transferred to the plasmons. With the increase of the metal film thickness, the efficiency of SPP excitation decreases as the tunnelling distance increases. The SPP at the interface between the prism and the metal cannot be excited in this geometry since the wave vector of the SPP at this interface is greater than the photon wave vector in the prism for all angles of incidence. This is however possible by the addition of a dielectric layer with a lower refractive index than the one of the prism between the metal film and the prism (Fig. 1.14(b)). In this geometry, the photon tunnelling through this additional dielectric can excite SPPs at the inner interface when choosing the proper angle of illumination.

For bulk metal, the Otto arrangement is used (Fig. 1.14(c)). Here, the light tunnelling occurs through the air gap between the prism and the surface [97]. Otto configuration is useful in the study of SPR in solid phase media. However, since the air gap between the metal and prism surface reduces the SPR efficiency, it is less useful for applications with fluids and solutions. The major drawback with the prism coupling technique is that it necessitates a prism where the refractive index is higher than the effective index of the SPP. So plasmonic mode with a high effective index cannot be excited with this scheme.

Near field optical microscopy offers the possibility to excite SPPs locally at a given place on a surface [98]. In this geometry (Fig. 1.14(d)), a small probe tip of aperture size smaller than the excitation wavelength of light illuminates the surface of a metal film in the near field. This configuration is treated as either a diffraction or tunnelling mechanism for SPP excitation. It allows high optical resolution through the local excitation of SPPs at the position of the scanning near field optical microscope tip. But at the same time the collection efficiency is limited by the aperture size and by the distance between the sample and the tip.

Another way to provide the conservation of wave vector is by a periodic pattern of shallow grooves or holes, i.e., grating couplers (Fig. 1.14(e) and (f)). The grating coupling system is based on the physics of diffraction grating. It can be realised by etching a smooth metal film (Fig. 1.14(e)) or by corrugations at the surface Fig. 1.14(f). When such a metal-dielectric interface is periodically distorted, incident wave will be diffracted in several beams with a variety of angles [99]. As a result, the component of the diffracted light whose wave vectors coincides with the SPs wave vector will be coupled. This excitation configuration provides efficient coupling to the plasmon mode for both air-metal and substrate-metal interfaces, when the film thickness and the grating corrugation depth and period are suitable.

The light can also be coupled to SPPs using optical waveguides or fibres. The light wave is guided by either a single or multilayer (slab or channel) waveguide to a region with a thin metal layer. In that region, the light wave evanescently penetrates through the metal. Under the phase matching condition of the guided mode and the SP mode, the incident photon excites the SPP at the outer interface of the metal layer. The use of optical waveguides offers some attractive features, including a simple control of the path for sensors, small sizes, light transmission over long distances and ruggedness [96]. The following section will present different waveguiding geometries of plasmon propagation in more details.

1.2.4/ PLASMONIC WAVEGUIDES

A wide variety of plasmonic waveguides have been investigated for the purpose of on-chip communication [100] and the fabrication of plasmonic devices and components including Mach-Zehnder interferometers, lasers, modulators, AND NOR gates, triple gates, control switches, routers, photon-electric converters etc [101]. The main reason of the growing interest in plasmonic waveguides is due to the subwavelength confinement while retaining the broad bandwidth transmission capacity from photonics [89]. An overview of the waveguide architectures are shown in Fig. 1.15.

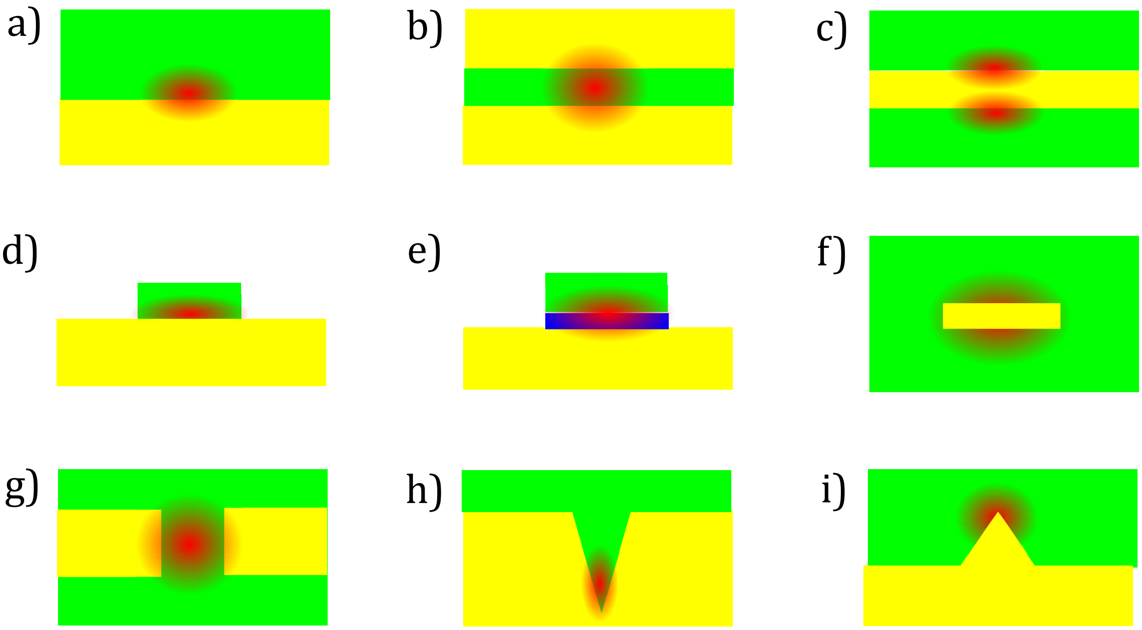

Figure 1.15: Plasmonic waveguides: (a-c) one dimensional plasmonic waveguides: (a) metal-dielectric interface, (b) dielectric film is sandwitched between two metal, (c) metal is sandwiched between between two dielectric. (d-i) Two dimensional plasmonic waveguides: (d) dielectric loaded, (e) low index hybrid, (f) metal strip, (g) gap, (h) channel, and (i) wedge waveguides. Metal layer is in yellow and dielectric layer is in green.

The simplest geometry to generate strong localization of electric field is a single metal-dielectric interface (Fig. 1.15(a). Here, SPPs at the interface of metal-dielectric can provide confinement only in the direction perpendicular to the interface.

Multiple interface systems such as two metal-dielectric interfaces can supports SPP modes. Here, SPPs are supported either by a thin dielectric layer bounded by metals (Fig. 1.15(b)) or a thin metal surrounded by a dielectric (Fig. 1.15(c)), often called metal-insulator-metal (MIM) or insulator-metal-insulator (IMI), respectively [102]. Excitation of two independent SPP waves occurs at two interfaces involving the dielectric and the metal when a thick metal film is sandwiched between a dielectric. But, the evanescent fields of the two uncoupled SPP waves into the metal cannot overlap with each other [103]. In contrast, for a very thin metal films of tens of nano meter thickness bounded by a dielectric can results two SPP waves into the metal and can form two coupled modes. One is called symmetric mode and the other is called antisymmetric mode. The field loss is smaller for symmetric mode because the electric field penetrates more deeply (several micrometers) into the dielectric via two identical evanescent tails. Also, the attenuation loss is much lower than that of the SPP at the single interface. The symmetric mode is therefore called the long-range SPP (LR-SPP) [104, 105, 102]. For the antisymmetric SPP mode, the field losses are very large due to an electric field mainly concentrated in the metal, which results in a strong loss. Therefore, antisymmetric mode is called the short-range SPP (SR-SPP) [104]. These two configurations have received a lot of attention due to the ease of fabrication.

Two dimensional (2-D) confinement is required for real applications. The most common 2-D geometries are shown in (Fig. 1.15(d-i)). In the case of dielectric loaded waveguide (Fig. 1.15(d)), the SPP is confined within the high-refractive index region and the propagation loss of SPP at the interface of metal-dielectric is larger when the dielectric contacting the metal has higher index. For low-index hybrid geometry (Fig. 1.15(e)), SPP exhibits strong localization to the thin (nanometer wide) layer of low index gap and attenuation is bounded between the low index and high index medium. The metal strip (Fig. 1.15(f)) configuration is useful to produce lateral confinement by limitting the width of the metal film. Though the attenuation of LRSPP in metal srip is ten times lower than the wide metal film, but the confinement is poor [106].

Better mode confinement is possible with gap waveguides (Fig. 1.15(g)). The gap mode supported by MIM structure can provide strong SR-SPP confinement and attenuation is comparable to that of the metal clads. The channel waveguide (Fig. 1.15(h)) has a V-shaped cut into a metal surface and it is useful for photonic integrated circuits functionality [107]. Difficulties to fabricate an extremely sharp groove or wedge angles to provide strong confinement has limited their applications. The inverse structure to V-groove waveguide is a metallic wedge (Fig. 1.15(i)) and faces the same fabrication challenges. Basically, all these waveguide schemes have their own advantages and disadvantages, the choice of the scheme is depends on the particular applications.

1.2.5/ APPLICATIONS AND CHALLENGES OF PLASMONICS

The previous sections described the basic concepts of plasmonics. In order to deeply appreciate the strength and success of plasmonics, it is important to understand the potential applications and challenges of plasmonics in sub wavelength optics.

One of the impressive application of plasmonics is in sensors. Plasmonic sensors have been used in many important areas including medicine, environmental monitoring, biotechnology, drug and food monitoring for detection and analysis of chemical and biochemical substances [96]. The sensing based on surface-enhanced Raman spectroscopy (SERS) can amplifies the electromagnetic field up to 10^{10} to 10^{11} times and identify the presence of specific target molecules based on their unique vibrational signatures [108]. In the typical SERS experiment, the incident laser light is focused onto the SERS hot spots on the metal nanostructure and the emitted light being detected from the same spot. This approach is not feasible with living systems because the high power incident light can cause destruction or induced chemical modification of the analyte.

Another spectacular applications of plasmon is in subwavelength imaging and superlens or perfect lens [109]. The wavelength of plasmon is much smaller than in the dielectric medium so they can be used to view objects much smaller than the wavelength of light. Opposite of this is the superlens which uses plasmons to view objects much larger than normally possible due to the diffraction limit. This is possible by plasmonic metamaterials.

Plasmon assisted solar cells (converts light into electricity) are found to be very useful in space exploration vehicle, rural electrification, for providing power to light houses, refrigerate medications etc. Unlike the conventional solar cells with a thick photovoltaic absorbers, plasmonic solar cells absorbers are very thin, typically less than 2 μm thick, and can use cheaper substrates than silicon such as glass, plastic or glass. However, thin film solar cells cannot absorb as much light as thick conventional solar cells made with same absorption coefficient [88].

Other promises of plasmonics including superfast computer chips [8], new possibilities to treat cancer [110], ultrasensitive molecular detectors [111, 112], invisibility with negative refractive index materials [113], quantum optics [114], optical data processing [107] and data storage [115]. All these are possible through the strengths of plasmonics such as 1) extreme light concentration and light manipulation below the free space diffraction limit; 2) straightforward tunability of the optically-resonant response of metallic nano-structures by engineering their size, shape or dielectric environment; 3) simple building blocks offer a tremendous design flexibility to create a large number of optical functions; 4) efficient light to heat conversion with high spatial and temporal control; 5) multi-functionality of nano-metallic elements in a single physical space [7].

Although plasmonics is a promising candidate for many applications, there are a number issues which needs to be solved. The primary restriction is related to the size of metallic nano structure. A minimum size is required for efficient collective oscillations of plasmons. The only way to overcome the physical restriction is to go beyond the diffraction limit of light.

Another issue is spectroscopy with ultra violet and deep-ultraviolet frequencies. As seen in dispersion curve (Fig. 1.12), plasmonics effects are significant only in the visible to near infra-red region. When we go beyond the plasmon resonance frequency, metals are not plasmonic, but dielectric. So we have to consider either a natural or artificial materials that can work as plasmonic materials in this frequency region.

The major limitation of SPs is its high propagation losses. Different approaches have been proposed to solve this challenge. One way of reducing the SPP attenuation is to use a thin metal film or operating the structure in the LR-SPP mode. In the case of LR-SPP mode, the power is concentrated mainly in the dielectric and hence the propagation loss is reduced. It has also been shown that the LR-SPP attenuation is at least a factor of 2 to 3 lower than that of the single interface SPP [116]. However, the comparable mode size of LR-SPP and dielectric waveguide modes makes them less suitable for nanophotonic applications. An optical gain medium can be used to compensate for the absorption losses in the metal. When a SPs suffer propagation loss, the gain medium could provide large enough amplification and hence reduce the losses. But, the pumping schemes with plasmonic waveguide is difficult in practice.

One possible way of compensating for SPP loss is to introduce dielectric materials close to a metal. This way of improving the plasmonic waveguide design can provide a compromise between loss and confinement. The second main goal of this thesis is following this approach and looking for the practical realization of strong field confinement together with low propagation losses.

1.3/ GOAL OF THE THESIS WORK: PLASMON-SOLITON COUPLING

We propose to demonstrate that beam focusing assisted with plasmon is possible. It paves the way to hybrid plasmon-soliton waves. This concept was envisioned for more than 35 years ago but no experimental demonstration has yet been revealed. The main goal of this thesis is to combine both solitons and plasmons to form self-trapped beam at low power.

The study of plasmonic effects at nonlinear regime is still an unexplored area. Only few nonlinear processes have been described and studied in plasmonic systems such as second harmonic generation [117, 118], optical limiting and self-phase modulation with nano particles [119]. In this thesis we will study the underlying mechanism of intensity enhancement brought by the plasmon through design, fabrication and characterization of a specific structure. The exploitation of the enhanced nonlinear effects and the hybrid wave propagation will lead to the development of integrated and standalone photonic devices. The following chapters will describe our work on the experimental demonstration of plasmon-soliton coupling in the proposed nonlinear plasmonic structure.

2

CHALCOGENIDE GLASSES, MATERIAL WITH LARGE OPTICAL NONLINEARITIES

Identifying optical materials for ultrafast all-optical signal processing and more generally for nonlinear photonic devices fabrication [120] has attracted researcher's attention over the past decades. Key materials such as silicon [121] or III-V compounds [122, 123] have been investigated. Although excellent results have been obtained for given spectral range, the quest for better material with stronger Kerr coefficient, lower two-photon absorption (TPA), negligible free carrier absorption and low-cost processing techniques are still relevant. Chalcogenide glasses (ChGs) that have large Kerr nonlinearity, ultrafast response time, and optical transmittance in the infrared are among the materials of interest.

In this chapter, we will discuss the properties of the ChGs that make them suitable for nonlinear optical applications and especially for plasmon-soliton coupling. The first section begins with an overview of the main features and the optical properties of the ChGs. The following section presents the Ge-Sb-Se based chalcogenides as well as their synthesis and fabrication carried out at the institute of chemical science in Rennes, France in collaboration with the group of Dr. Virginie Nazabal. We then present the characteristics of the fabricated films such as chemical composition, index of refraction and optical band gap. Subsequently, the measurements of linear absorption losses of the fabricated waveguides are described. This chapter will conclude with the selection of three nominal compositions for the nonlinear characterization at the telecommunication wavelengths.

2.1/ CHALCOGENIDE GLASSES: PROPERTIES AND APPLICATIONS

The term 'chalcogen' means 'ore former,' derived from the Greek words chalcos that means 'ore' and gen that means 'formation' [124]. The elements of group sixteen of the periodic table such as sulfur, selenium and tellurium (but not oxygen) are known as chalcogens. These glasses are formed by the addition of other elements for example arsenic, gallium, antimony, silicon etc. The glass structure consists of covalently bonded molecules, in contrast with the ionic bonding of other glasses, and these are bound together via a combination of covalent and Van der Waals-like attractions [125, 126]. One can classify chalcogenide materials by the type of atoms to which they bond to form amorphous systems. The most known amorphous chalcogenide systems under these classifications are pnictogen-chalcogen (e.g., (V-VI) As_2S_3, P_2Se), tetragen-chalcogen (e.g., (IV-VI) $SiSe_2$, In_xSe_{1-x}), metal chalocgenide (e.g., MoS_3, WS_3) and halogen-chalcogenide (e.g., As-Se-I, Te-Cl) [127, 128]. Chalcogenides can also be doped with rare earth elements (e.g., Er, Nd, Pr, etc.) to enhance the functionalities. Furthermore, they exist naturally as minerals for example FeS_2 and $AuTe_2$ [127]. Basically, ChGs can be formed with a wide variety of composition and it can be adjusted to tune the optical properties such as refractive index, band gap and nonlinearity.

ChGs are advantageous over many materials (monocrystalline Ge, polycrystalline ZnSe) which is currently used for mid-infrared applications [129]. They can be molded by simple heating above their glass transition temperature (T_g). The strong mechanical properties (hardness, toughness, etc.), a relatively easy synthesis and lower production costs of chalcogenides than mono or polycrystals (Ge, ZnS) make them suitable for infrared (IR) optical applications such as detection of chemical and biological species, production of infrared fibers, agricultural and environmental analysis, or quality control in food industry, etc. [130, 131].

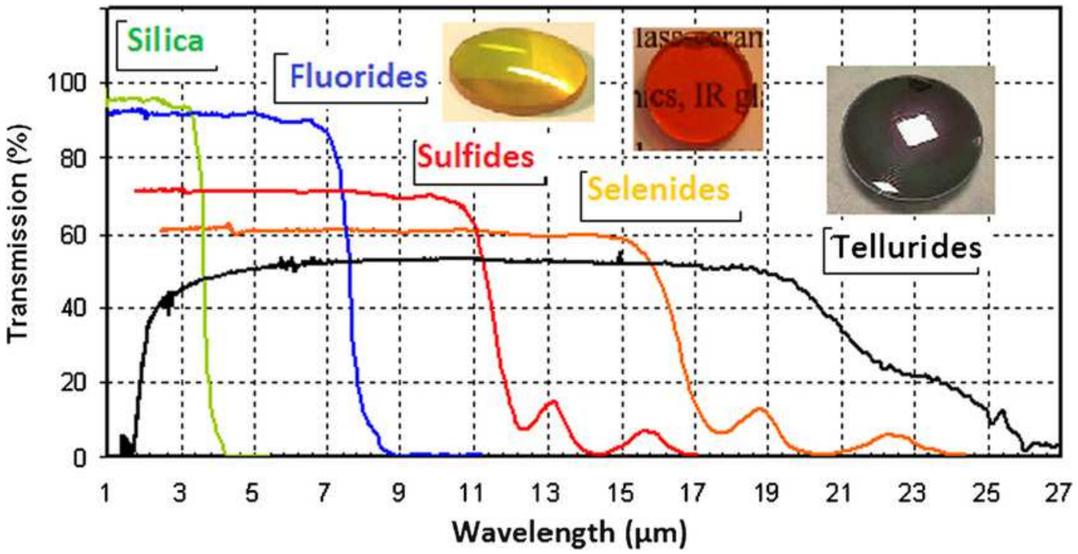

Figure 2.1: Transparency window of different glass families. The insets are examples of sulfide As_2S_3 (yellow), selenium As_2Se_3 (red) and tellurium $Te_{20}As_{30}Se_{50}$ (black) glasses. Figure taken from [129].

One of the main interest of ChGs lies in their wide transmission window that can extend from the visible to the mid-infrared depending on chemical composition [129, 126]. For example, wavelengths up to 10 μm for sulfides, 12-13 μm for selenides, and 18-20 μm for tellurides can be transmitted as seen in Fig. 2.1 [132, 133]. As also shown in Fig. 2.1, these glasses are partially transparent in the visible range for glasses based on sulfur and opaque for selenium or tellurium based glasses. The introduction of heavier elements in the glass composition can further broaden the spectral window to longer wavelengths due to the modification of phonon vibrations. However, the extension of the transparency window to short wavelengths are very complicated because it is connected to the variation of the electronic band gap. The imagery using visible (Fig. 2.2(b)), near-IR (Fig. 2.2(c)) and thermal-IR radiations offer a large number of applications including the driving assistance of a vehicle to read the road signs properly (Fig. 2.2(a)). The thermal imaging permits one to see in the fog and to detect the presence of pedestrians even in the dark [129] and in military areas for de-camouflaging hot targets [129]. Further, ChGs are promising sensors materials for the infrared spectral range [134].

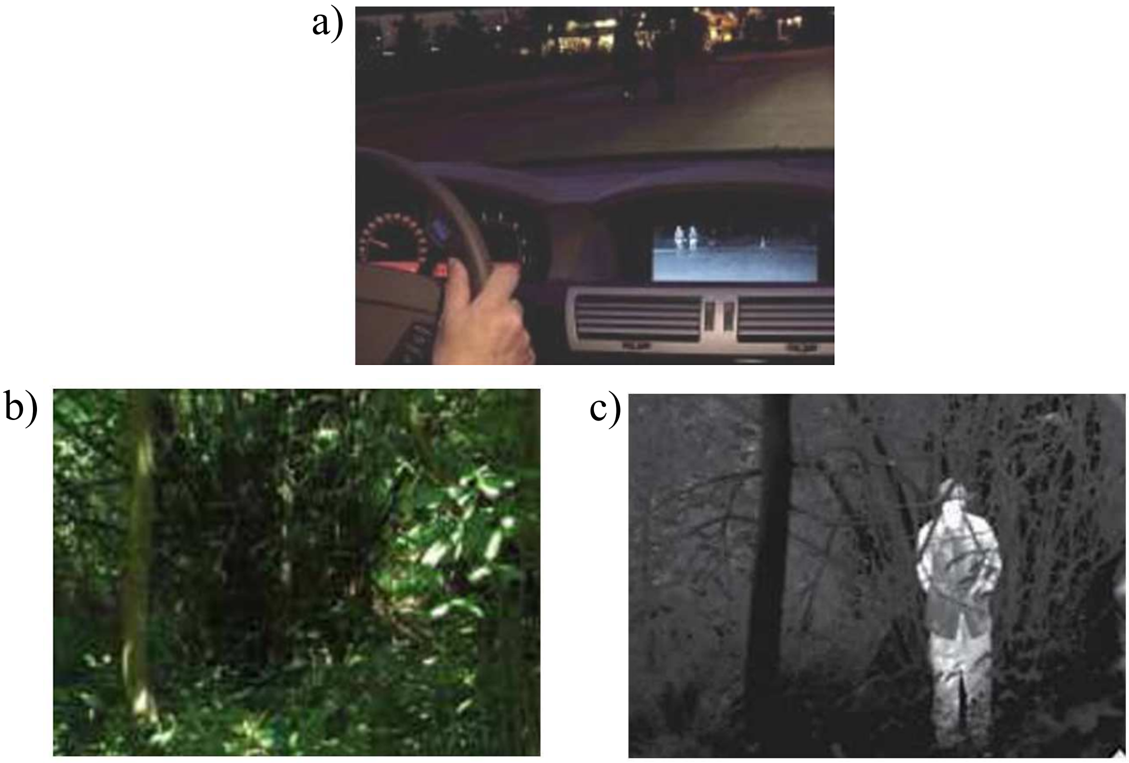

Figure 2.2: (a) Night driving assistance, (b) visible image, (c) same image in the infrared. Figures taken from [129].

Another important and most widely studied properties of ChGs is their photosensitivity [135, 136, 137]. This is associated with the local changes in the chemical bonds and in the valency of neighbouring atoms induced by the irradiation of light at a wavelength close to the band gap. Commonly observed photoinduced phenomena involve changes in the optical properties of the system such as band gap energy (photo-darkening or photo-bleaching [138]) and corresponding to the refractive index [139]. Others include photo-decomposition, photo-crystallization, photo-polymerization, photo-dissolution and photo-vaporization [128, 140].

As its name implies, photo-decomposition is the light-induced dissociation of a compound into its constituents and occurs when illumination of photon energy greater than E_g of the material. Phenomena called photo-crystallization and re-amorphization have been well studied in As-Te-Ge compositions and requires pulsed laser system to raise the temperature of the film to the melting point of the crystals. Similarly, photo-electronic and chemical changes are possible during photo-polymerization of chalcogenide films. The usual configuration to observe the photo-dissolution effects consists of deposition of a thin metallic layer on or below the chalocogenide film. Further, this effect is possible with a photon of energy above or below E_g of the material or illumination from either the chalcogenide or metallic (e.g., silver, copper) side. While, photo-vaporization is strictly a photo-oxidation reaction followed by thermal evaporation of the volatile oxidation products.

All mentioned photoinduced effects can be observed in bulk glasses and particularly in films, because film can condense into amorphous state with a large number of defective bonds, creating a different topology from that of bulk glasses [141]. Both reversible and irreversible photoinduced effects are observed in both poorly annealed vapour-deposited films or in well-annealed glasses [142]. In additon, photoinduced effects can be of interest for applications such as optical imaging, hologram recording, photolithography, light trimming bandpass filters etc. [143, 136].

Specific chalcogenide alloys posses low acoustic loss and high acousto-optics figure of merit. Further, recent work on chalcogenides was for acousto-optic applications [144]. Ternary ChGs of $Ge_{33}As_{12}Se_{55}$ (AMTIR-1) can be used for bulk acousto-optic cells operating in the near IR [145].

The main reason for choosing chalcogenides as our key material is due to its high refractive indices and its flexibility to fabricate waveguides [146]. ChGs exhibit high third-order nonlinearities between two to three orders of magnitude greater than silica in the near infrared region and high values of linear refractive index (2.2 to 2.6 for sulfides [147], 2.4 to 3.0 for selenides [148], and 2.6 to 3.5 for tellurides [149]). Further, the large index difference between chalcogen and air can provide a complete band-gap for photonic crystals [126]. The high refractive indices are advantageous for strong field confinement which allows waveguides with low bend loss at small radii (leading to compact circuit designs) and enhanced optical intensities (for efficient nonlinear interactions) [129]. These unique features make them great for developing next generation integrated photonic chip platforms for ultrafast all-optical processing including regeneration [126], optical performance monitoring [150], optical sampling [151], wavelength conversion [152], logic gates [153].

The moderate level of two-photon absorption at telecommunication wavelength [154, 155] and negligible free-carrier absorption [156] in contrast to semiconductors make them also well suitable for applications in nonlinear optics.

ChGs have received an increased interest due to all these properties. However, key challenges to their use include toxicity, lack of chemical and mechanical durability, thermal expansion incompatibilities with certain substances and stability issues during the processing have to be resolved [145]. Hence, the choice of a proper chalcogenide composition is very important.

While few chalcogenide compositions and systems such as As_2S_3 [157], As_2Se_3 [158], Ge–As–S(Se) [159], and Ge–Sb–S [160, 161] have been intensely explored for nonlinear optical properties purposes, new chalcogenide glasses are still synthesized, with the hope that a high-bit-rate optical processing system operating at low peak power can be reached. For our studies ChGs of composition Ge-Sb-Se is selected. The reason behind the selection of this particular ternary composition is presented in the following section.

2.1.1/ CHOICE OF GE-SB-SE SYSTEM

The composition of Ge-Sb-Se have many advantages including wide range of optical transparency. The quantity of Ge atom into Se matrix allows modification in the chemical composition and the energy band structure. Most importantly, it can extend the transparency window up to 1600 nm [162, 128]. To further strengthen the material, a third element such as Sb can be introduced into the Ge-Se system. Sb increases the (non)linear refractive index of the corresponding chalcogenides due to an enlargement of (hyper)polarizability [163]. The corresponding ChGs will also have a lower band gap energy related to this addition. Moreover, Sb is an element that reduces photosensitivity of the glass and this property could be tailored by changing the proportion of Sb [148].

This Ge-Sb-Se glass can be synthesized at very low temperature which is advantageous for the integration with silicon technology. In addition, Ge-Sb-Se composition can provide better thermal, mechanical and chemical properties including higher melting and glass transition temperature and lower thermal expansion coefficient such as $\sim 16 \times 10^{-6}/°C$ compare to $21.4{\times}10^{-6}/°C$ for As_2S_3 [126, 164]. Compared with arsenic-contained glasses such as As_2S_3, As_2Se_3, and Ge-As-Se [165], selenium based ChGs especially Ge-Sb-Se glasses are less toxic which makes them environmentally acceptable. Moreover, the tailoring of the glass chemical composition in Ge-Sb-Se system could provide large Kerr nonlinearity, low Two Photon Absorption (TPA) and optimized figure of merit.

In addition, selenide system has a large glass forming area, giving the possibility to choose the composition of glasses in accordance with the desired properties and ap-

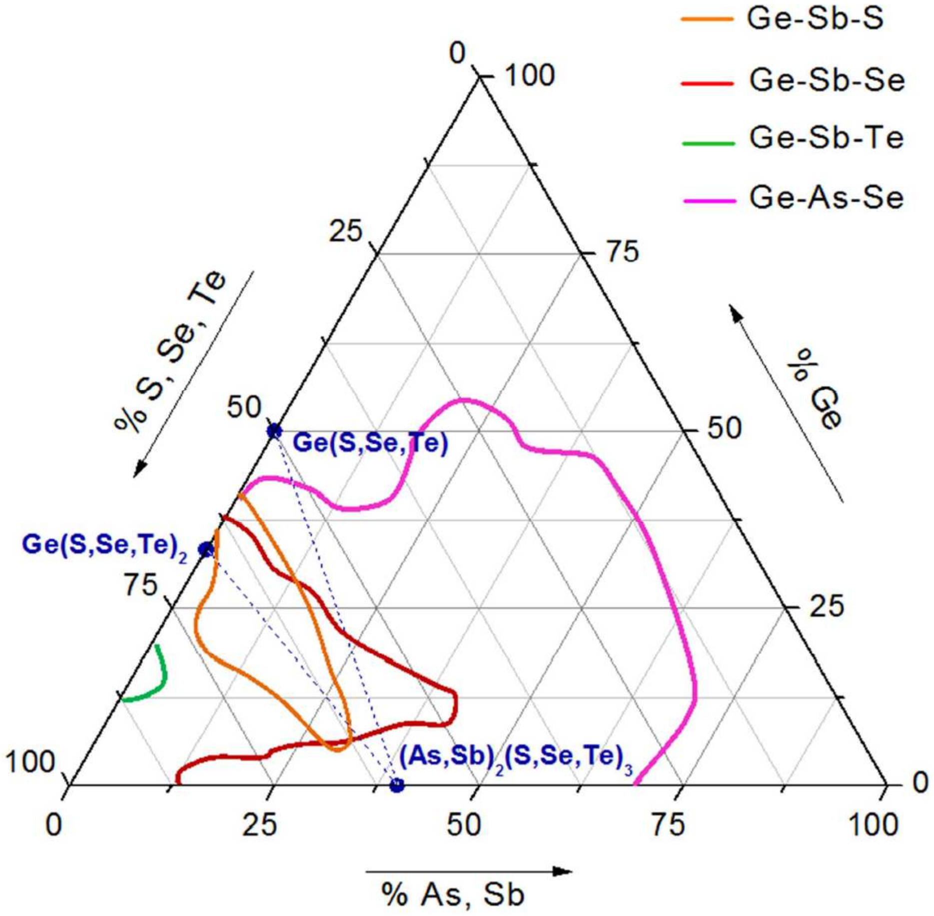

Figure 2.3: Glass forming areas of Ge systems (As, Sb)-(S, Se, Te). Figure taken from [166].

plications. For a comparison, glass forming areas of different systems such as Ge-Sb-S, Ge-As-Se and Ge-Sb-Te are shown in Fig. 2.3. In the case of Ge-Sb-S system, glassy field is greater than that of selenides, but the glassy field offers by sulfides are less interesting for our study. Indeed studies have shown that the selenides can have a high nonlinear refractive indices of $\sim 1.2 \times 10^{-17} m^2/W$ which is ~3-4 times higher than that of sulfides [155]. Since we are interested in the third order optical nonlinearity and related applications of ChGs, selenide system is a good choice.

Research into Ge-Sb-Se thin films and waveguides have attracted much attention due to their great potential for use as integrated biological and chemical sensors, optoelectronic and thermal electric device fabrication [146, 167]. Recently, the linear and nonlinear optical properties of Ge–Sb–Se glasses have been studied at near and mid infrared wavelengths [148, 163, 168, 169, 170]. Krogstad *et al.* reported nonlinear properties of bulk and single mode strip waveguides made of $Ge_{28}Sb_{12}Se_{60}$ glass at a wavelength of 1030 nm [171]. Nevertheless, the Kerr nonlinear response of Ge–Sb–Se amorphous materials, when fabricated in thin film forms, needs further studies. Thus we will focus on linear and nonlinear characterization of selected chalcogenide waveguides from Ge-Sb-Se system.

2.1.2/ SYNTHESIS OF CHALCOGENIDE GLASS TARGET

Chalcogenide glass targets from pseudo-binary $(GeSe_2)_{(100-x)}(Sb_2Se_3)_x$ (where x=10, 30 and 50) system were synthesized in the laboratory of the Institute of Chemical Sciences in Rennes, France by the conventional melting and quenching method. High purity elements of Ge, Sb, Se are selected for the glass preparation. Since they are very sensitive to contamination by the oxygen, the synthesis is performed in a silica tube under vacuum. The experimental setup used for the systhesis of glasses is shown in Fig. 2.4.

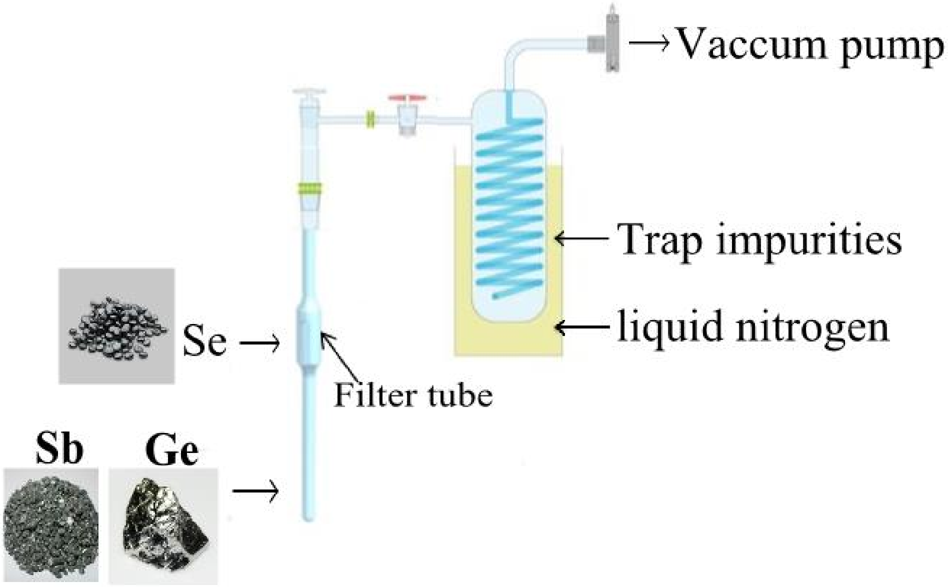

Figure 2.4: Schematic of the experimental set up used for the synthesis of Ge-Sb-Se glasses. Figure taken from Ref. [166].

It is composed of a turbo molecular vacuum pump and trap impurities cooled with liquid nitrogen. The use of the vacuum trap cooled with nitrogen make it possible both to protect the pump and to avoid steam release of the various elements present in the atmosphere. Then purified selenium is introduced into the filter tube and germanium and antimony are added directly into the tube. After that, the assembly is sealed under vacuum (10^{-4} mbar) over the filter. This sealed assembly is then placed in a furnace called distillation furnace. This has two distinct zones named as a hot zone (750°) and a cold zone. Selenium which is located in the hot zone of the oven, evaporates and condenses in the cold zone with the other two elements. This step can eliminates the non-volatile species present in the selenium such as carbon and residues of silica. All constituent elements of ChGs are combined in the reaction tube which is then sealed below the filter.

As a next step, the reaction tube is inserted in a tilting furnace. The mixture is melted at 850°C and maintained at this temperature for 9 hours to allow complete reaction between the elements and good homogenization in the liquids allowing the formation of Ge-Se-Sb. After this phase of melting, the furnace temperature was lowered to (750°C) for two hours to reduce the vapor pressure above the melt, thereby facilitating quenching. In order to avoid the crystallization during the quenching step, the glass is cooled with water. The glass is then annealed for several hours at a temperature close to its glass transition temperature ($T_g - 20°C$). This step reduces the mechanical stresses due to rapid cooling of the quenching. Finally, the glass is slowly cooled down to room temperature and then cut and polished to form glass samples. An example of the glass rod obtained by this method is shown in Fig. 2.5.

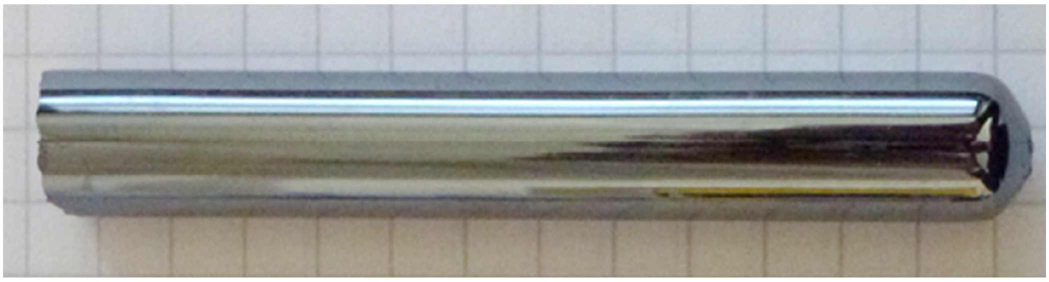

Figure 2.5: Photograph of the glass rod of $(GeSe_2)_{90}(Sb_2Se_3)_{10}(2S1G - Se - 3)$ (diameter 12 mm and length 6.5 cm). Photo taken from Ref. [166].

2.1.3/ PLANAR WAVEGUIDE FABRICATION

The next step consists in the fabrication of slab chalcogenide waveguides since Kerr spatial solitons are only stable in this configuration. One advantage of using slab/planar waveguides based on chalcogenides is the low-cost production techniques. Further, the light guidance and propagating nature in a confined space is advantageous for coupling the plasmon-soliton waves. This section presents the fabrication of planar waveguides from Ge-Sb-Se system.

Commonly used techniques for the fabrication of chalcogenide thin films are chemical vapour deposition [172], thermal evaporation [173], pulsed laser deposition or radio-frequency sputtering [174]. Since the film characteristics such as stoichiometric conformity, morphology, topography, structure or optical properties can be affected by the deposition method, it is important to choose the right deposition technique. Here, we will concentrate on the Radio-frequency (RF) magnetron sputtering because of its relative simplicity, easy control of the process, good adherence, high composition control, good homogeneity and possibility to fabricate multi-layered structures or films of unusual compositions [126, 162].

2.1.3.1/ Principle of RF magnetron sputtering

Before going to the details of RF magnetron sputtering, it is better to start from the basic idea of sputtering process. Sputtering is a physical vapour deposition process used for depositing thin films onto a substrate (e.g. silicon), by ejecting atoms from target (or source) materials and condensing the ejected atoms onto a substrate in a high vacuum environment. Schematic view of the basic sputtering process is shown in Fig. 2.6. This process begins when a target is bombarded with energetic ions, typically inert gas ions such as Argon (Ar^+). The forceful collision of these ions onto the target ejects target atoms into the space. These ejected particles then travel some distance until they reach the substrate and starts to deposited as thin film onto the surface of the substrate.

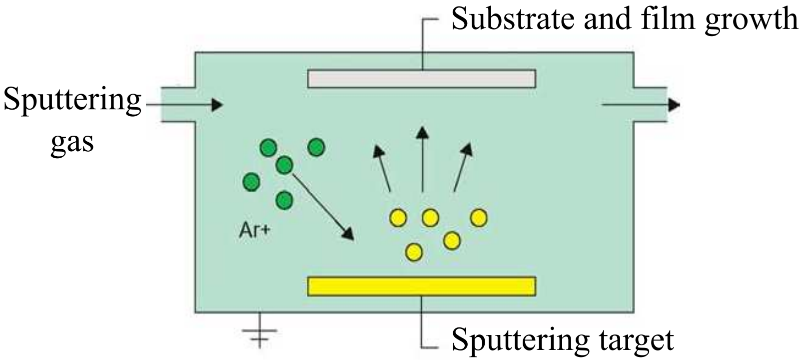

Figure 2.6: Overview of the basic sputtering process. Figure taken from wikipedia.

There are a number of ways to enhance the sputtering. One way is to use a magnetron sputtering system. The main difference between magnetron and simple sputtering described above is the addition of a magnetic field originating from permanent magnets placed below the target (Fig. 2.7). This magnetic field causes travelling electrons to spiral along the magnetic flux lines near the target instead of being attracted towards the substrate. Since plasma (ionized gas consisting of approximately equal numbers of positively charged ions and negatively charged electrons) is confined to an area near the target, thin films can be formed without damages. Moreover, magnets can increase the number of electrons that take part in ionization and thereby increase the probability of electrons striking the Argon atoms, increase the length of the electron path, and hence increase the ionization efficiency significantly [175].

Magnetron sputtering is possible in RF or DC modes. For a conducting target, a DC power supply is mainly used. Note that, this DC voltage is placed between the target and substrate which ionizes Argon atoms and creates plasma. In the case of insulating or

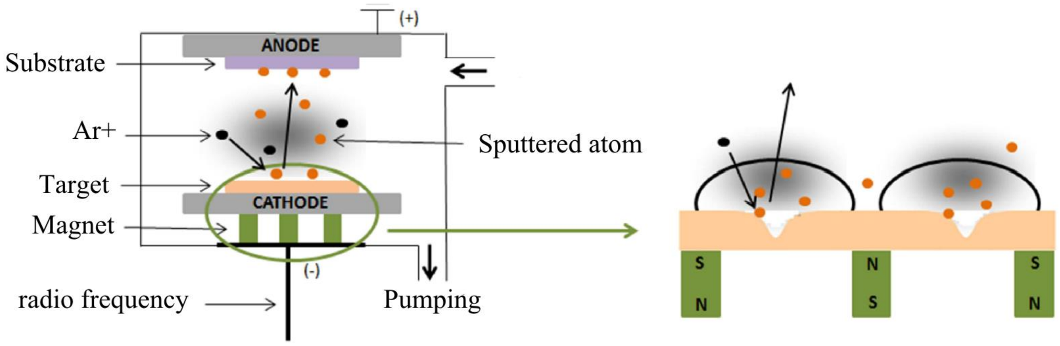

Figure 2.7: Schematic diagram of the RF magnetron sputtering device. Figure taken from Ref. [166].

semiconducting targets, positive charge will build up on the material and it will stop the sputtering hence an RF power supply is required. Further, RF sputtering can be applied on both conducting and non conducting materials.

2.1.3.2/ THIN FILM DEPOSITION

Fabrication of the films were realised by the group of Dr. Virginie Nazabal of the Institute of Chemical Sciences Rennes, France and also by Dr. Peter Nemec from Pardubice in Czech Republic. The insulating nature of our materials requires to work in RF mode. ChGs prepared by the conventional melting and quenching discussed above were used as a sputtering targets for thin films deposition. As shown in Fig. 2.8, targets with a diameter of 50 mm and thickness of 3.5 mm were obtained by slicing the glass rods followed by polishing with abrasive discs. The SiO_2/Si substrate used for the deposition of thin films were chemically cleaned at room temperature with a detergent solution (surfactant) in an ultrasonic bath. It is worth noting that, several parameters such as the distance between the target and the substrate, the substrate temperature, the nature and pressure of the gas (Argon), and the applied RF power can influence the quality of the fabricated film. In our case, we identified three factors as being the most influential factors such as the argon pressure (mbar), the applied RF power (W), and the deposition time (min).

The high quality thin films were deposited on oxidized silicon substrate under the following conditions. The working pressure and the Ar gas flow ranged from 5×10^{-3} to 5×10^{-2} mbar and 25-100 sccm (Standard Cubic Centimeters per Minute) respectively is used. The sputtering power was maintained at a low RF power (10-25 W) considering the insulator nature of the targets and the requirement of fabrication of amorphous layers. Deposition rate varied from ~10 to ~70 nm/min depending on the target chemical composition and the distance between the substrate and target since the optical waveg-

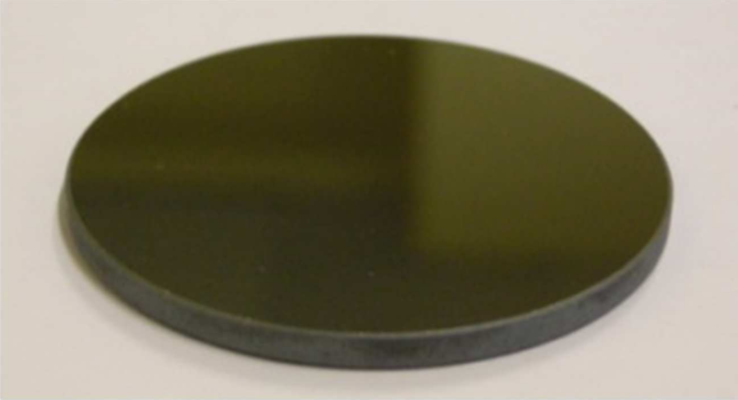

Figure 2.8: Chalcogenide glass target from Ge-Sb-Se system. Photo taken from Ref. [166].

uiding requires selenide layers of few microns thickness. Finally, the three dielectric layers (SiO_2/chalcogenide/air) with different refractive index allows the formation of slab waveguides.

2.2/ CHARACTERIZATION OF PLANAR WAVEGUIDES

The following characterizations were carried out at the Institute of Chemical Sciences in Rennes, France in Dr. Virginie Nazabal's group.

The chemical composition of the fabricated Ge-Sb-Se structures were analysed by scanning electron microscope (SEM) with an energy-dispersive X-ray analyser (JSM 6400-Oxford Link INCA, Buckinghamshire, UK). The realized compositions $Ge_{12.6}Sb_{24.5}Se_{62.9}$, $Ge_{19.5}Sb_{17.8}Se_{62.7}$ and $Ge_{28.8}Sb_{5.8}Se_{65.4}$ are in agreement with the theoretical target composition of $Ge_{12.5}Sb_{25}Se_{62.5}$, $Ge_{19.4}Sb_{16.7}Se_{63.9}$ and $Ge_{28.1}Sb_{6.3}Se_{65.6}$ with a measurement uncertainty of about ±0.5 %. For simplicity, sputtered films are named in a general way by considering the theoretical compositions of the targets; i.e., $Ge_{12.5}Sb_{25}Se_{62.5}$, $Ge_{19.4}Sb_{16.7}Se_{63.9}$ and $Ge_{28.1}Sb_{6.3}Se_{65.6}$ or with a simplified name, Se6, Se4 and Se2 respectively. The chemical compositions of the sputtered films are presented in Table. 2.1.

The chalcogenide guiding layer thicknesses were determined by ellipsometry and SEM techniques (See Table. 2.1). Further, micro-Raman spectroscopy was used to determine the structure and physicochemical properties of the RF sputtered selenide films. Prepared thin films are found to be of good quality in terms of morphology, topology and surface roughness. More details of the films quality analysis deterimend by the non-optical methods of SEM, atomic force microscopy, and energy dispersive spectroscopy can be found in Ref. [166].

Table 2.1: Material parameters for the chalcogenide thin films

Sample	Theoretical composition	Real composition	Guiding layer thickness (μm)
x=50/Se6	$Ge_{12.5}$ Sb_{25} $Se_{62.5}$	$Ge_{12.6}Sb_{24.5}Se_{62.9}$	3.0
x=30/Se4	$Ge_{19.4}Sb_{16.7}Se_{63.9}$	$Ge_{19.5}Sb_{17.8}Se_{62.7}$	3.0
x=10/Se2	$Ge_{28.1}$ $Sb_{6.3}Se_{65.6}$	$Ge_{28.8}Sb_{5.8}$ $Se_{65.4}$	3.2

2.2.0.1/ REFRACTIVE INDEX AND OPTICAL BAND GAP OF THE CHALCOGENIDE LAYER

The refractive index of the films in the near infrared range were measured by the prism coupling technique using a Metricon 2010 equipment. As shown in Fig. 2.9, the film to be analyzed is brought into contact with the prism base by means of a pneumatically-operated coupling head, creating a small air gap between the film and the prism. A laser beam strikes the base of the prism where refractive index is higher than the film and is reflected at the base of the prism onto a detector. At certain values of the incident angle (θ_i), photons can tunnel across the air gap into the film and enter into a optical propagation mode, causing a sharp drop in the transmitted intensity to the detector. To determine film index, measurements were made with silicon prism at the wavelengths of λ =1550 nm and λ =1311 nm. This technique allows a measurement of the films index with an uncertainty of $\pm 10^{-3}$. The obtained values are listed in Table. 2.2. As expected, the refractive index values rises by increasing the proportion of antimony from 2.47 (for se2) to 2.9 (Se6) at 1550 nm. The high refractive index of the chalcogenide films and the presence of lower refractive index SiO_2 layer form a step index waveguides with high index contrast.

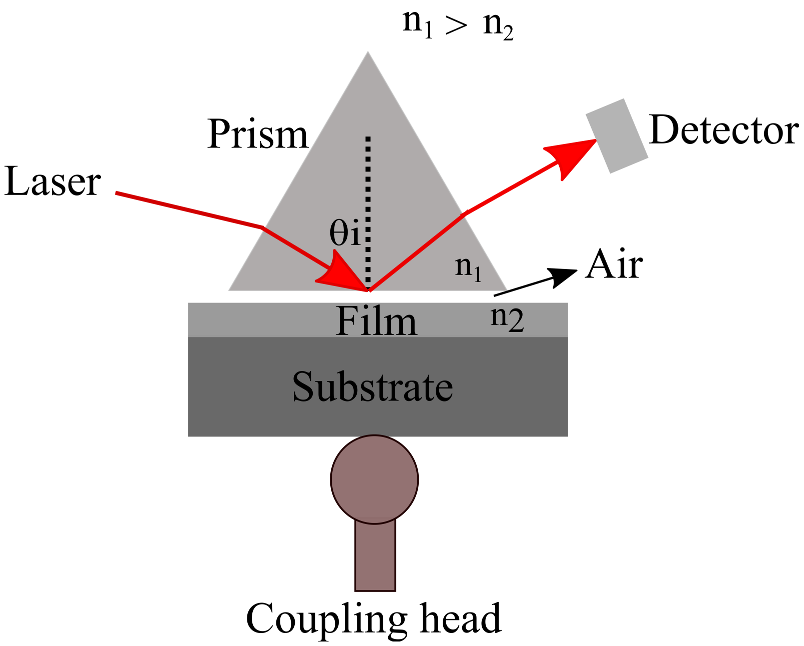

Figure 2.9: Principle of the prism coupling technique.

In addition to the above analysis, the dispersion of the refractive index of the films as a function of wavelength in the near infrared spectrum were extracted from the variable angle spectroscopic ellipsometer (VASE) technique (VASE, J.A. Woollam Co., Inc.). In ellipsometry, the change of polarization state of linearly polarized light is measured upon reflection at the surface of the sample (Fig. 2.10). The polarization states after reflection depend on properties of the investigated surface and, in case of multilayer thin film system, on the properties of each layer. Compared to standard ellipsometry, VASE measures the sample's coefficients in s-and p-polarized light (where s-is electric field perpendicular to and p-is in to the plane of incidence) as a function of wavelength and angle of incidence [176]. Two experimental parameters, ψ and Δ, called changes in amplitude and phase, are usually measured. Further, the following parameters can be deduced such as thin film thickness and refractive index.

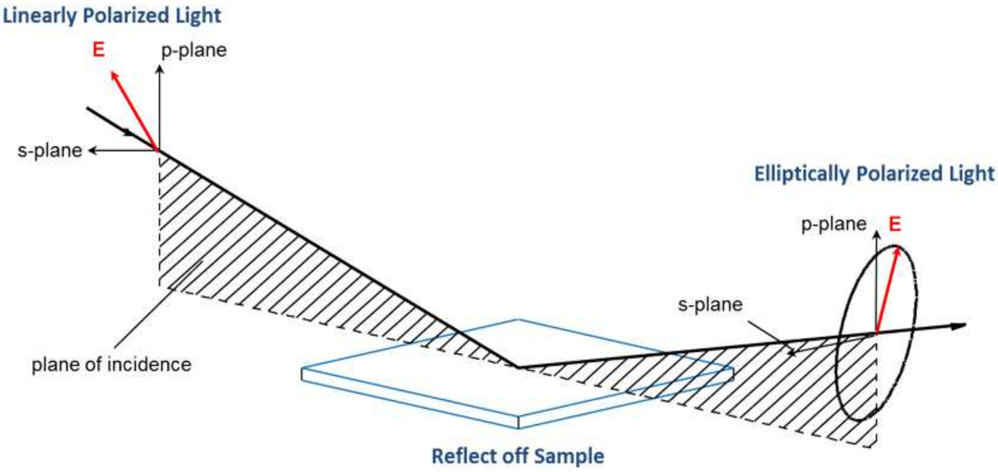

Figure 2.10: Typical ellipsometry configuration. Figure taken from Ref. [177].

Measurements were performed for the spectral range of 300-2300 nm (UV-Vis-NIR) with wavelength steps of 10 nm and angle of incidence of 65°, 70° and 75°. The resolution of UV-Vis-NIR ellipsometer of 20, 10 or 5 nm was selected. The optical response of the thin films were fitted using the Cody-Lorentz (CL) model [178] which is appropriate to describe the optical functions of thin films. Thickness of thin film and its uniformity were selected as fitting parameters. Experimental data of VASE were analysed using a three layer model: i) a glassy substrate, ii) chalcogenide thin film and iii) a rough surface layer. Note that, the measurement uncertainty was $\pm 10^{-2}$ which is greater than that of refractometry. However, this technique has the advantage of providing the dispersion of the refractive index of the material over a wide range of wavelengths. The refractive index obtained by ellipsometry at 1311 nm and 1550 nm are also listed in the Table. 2.2.

Optical band gap values of the fabricated waveguides were also extracted from VASE data again employing Cody–Lorentz model [178]. As listed in Table. 2.2, the band gap

Table 2.2: Refractive indices and band gap of chalcogenide thin films

Sample	Prism coupling		VASE		Eg
	n(1311 nm)	n(1550 nm)	n(1311 nm)	n(1550 nm)	(eV)
x=50/Se6	2.93	2.90	2.92	2.89	1.70
x=30/Se4	2.68	2.67	2.69	2.67	1.86
x=10/Se2	2.48	2.47	2.48	2.47	2.11

values of the Ge-Sb-Se system decreases with the addition of Sb content. The decrease in optical band gap is due to the formation of Sb/Se bonds having lower bond energy than Ge/Se bonds. In addition, the variation of the glass network structure and the variation of defects affected by deposition parameters could lead to the variations in the band gap energy (E_g) [179]. It is worth noting that E_g has a great correlation with third-order nonlinear properties. Thus, a stronger Kerr nonlinearity can be expected for Se6.

2.2.1/ MEASUREMENTS OF WAVEGUIDE LOSSES

The determination of optical losses in waveguides is of great interest for the fabrication and optimization of the parameters of the integrated optical devices. Three main mechanisms are considered to cause losses in waveguides; absorption, scattering and radiation. In order to make waveguides into a functional optical devices its losses should be reduce as low as possible.

The basic method to determine losses consist in injecting a known optical power into one end of the waveguide and measure the emerging power from the other end. However, there are many problems and imprecisions inherent in using such basic approach. A number of techniques have been developed to circumvent the basic issues and to accurately measure the optical losses. Commonly used techniques are prism coupling, Fabry-Perot loss measurement, transmission methods, thermo-optical methods such as photo-acoustic and thermal lens techniques and cutback method [180]. Among these techniques, we chose cutback method to determine the linear losses in the fabricated planar waveguides.

2.2.1.1/ LINEAR LOSS MEASUREMENTS BY CUTBACK METHOD

Cutback method is a simple method for direct measurement of transmission losses by comparing the transmittances of waveguides having different lengths [181]. The method is performed by injecting light of the desired wavelength inside a polished or cleaved input face of a waveguide and measuring the total power transmitted. A series of transmitted power measurements are recorded starting with a relatively long sample and then repetitively shortening the sample by cleaving. We used a simple hand tool called diamond-tip scribe for cleaving the samples. Note that we also used a dicing saw to shorten the waveguides but light coupling to the waveguide was poor due to the low-quality facets. Schematic drawing of the cleaved waveguide is shown Fig. 2.11. Moreover, cutback method requires two waveguides of equal quality and different length since the measurements are repeated for several times. As a matter of fact, proper care has to be taken before each measurement to have optimum end constant coupling efficiency.

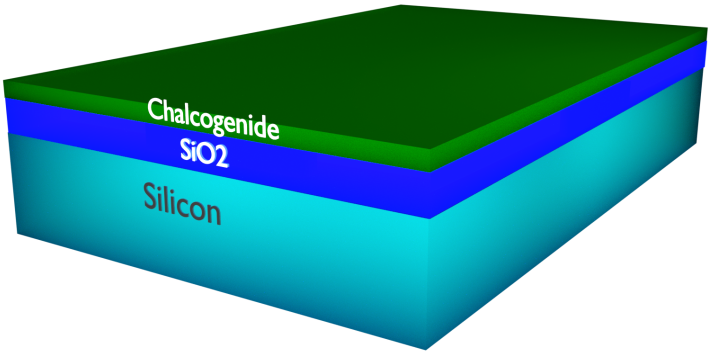

Figure 2.11: 3D artistic view of the planar chalcogenide waveguide.

In our case the measurements are performed by cleaving the waveguides into two different lengths, starting from the long propagation length z_2=1 cm to a small length z_1=0.5 cm. We make sure that the same power is coupled in both waveguides by optimizing the coupling efficiency. The following equation is then used to calculate the linear losses,

$$\alpha_1 = \frac{\ln(P_1/P_2)}{z_2 - z_1}, \text{ for } z_2 > z_1, \tag{2.1}$$

where P_1, P_2 are the transmitted power for the short and long sample [182]. The linear absorption coefficient of waveguides extracted from cut back method is included in Table. 2.3.

Linear losses of 0.19 cm^{-1} for Se2, 0.24 cm^{-1} for Se4, and 0.26 cm^{-1} for Se6 are measured at 1550 nm. As expected, loss is decreasing as material bandgap energy increases. Since the photon energy is closer to the material bandgap at 1200 nm, larger propagation losses range from 0.63 cm^{-1} for Se2 to 0.76 cm^{-1} for Se6 are determined. Comparison with data found in the literature is not straightforward since ternary glasses of the very same composition have not been studied or different wavelengths have been considered. The propagation loss values measured in our three planar waveguides at

Table 2.3: Linear loss of the selenide waveguide

Sample	λ (nm)	Linear loss $\alpha_1(cm^{-1})$
x=50/Se6	1550	0.26
	1200	0.76
x=30/Se4	1550	0.24
	1200	0.71
x=10/Se2	1550	0.19
	1200	0.63

1200 nm are consistent with the waveguiding loss values measured at 1064 nm in the compositions of $Ge_{29.9}Sb_{15.6}Se_{54.5}$ prepared by RF sputtering presenting a deficit in selenium [183]. At 1550 nm, the values can be compared to one found in bulk glasses of similar composition [148]. Our waveguides present larger losses (Table. 2.3) than the values measured in bulk, which may be attributed to additional losses due to the waveguide imperfections.

2.2.2/ SUMMARY

Among the variety of nonlinear materials, ChGs are selected due to their large Kerr nonlinearity, low losses, low fabrication cost and numerous applications in the infrared region. We particularly opted for the Ge-Sb-Se composition for several reasons. Firstly, the surface oxidation and formation of crystals can be reduced by antimony. Secondly, the introduction of selenium instead of sulfur could extend the optical transparency of chalcogenides further in the infrared spectral range. The fabrication of amorphous thin films from $(GeSe_2)_{(100-x)}(Sb_2Se_3)_x$ system with x=10, 30 and 50 are carried out by RF sputtering technique. Three different types of composition are selected, $Ge_{12.5}Sb_{25}Se_{62.5}$, $Ge_{19.4}Sb_{16.7}Se_{63.9}$ and $Ge_{28.1}Sb_{6.3}Se_{65.6}$ and called Se6, Se4 and Se2 respectively due to their excellent mid-IR transparency, high stability against crystallization and refractive index contrast allowing optical waveguiding in mid-IR.

Optical properties of the fabricated waveguides are studied by employing VASE and prism coupling technique. The measured refractive index at 1550 nm is 2.93, 2.68, and 2.47 for respectively Se6, Se4, and Se2. The material band gap energy of 1.70 to 2.11 eV is deduced by VASE. Linear loss values of the fabricated waveguides are measured by cutback method at 1200 nm and 1550 nm. Lowest value of propagation loss is found in Se2. Among the three compositions, Se6 has the smallest E_g and the largest refractive index. Importantly, with the increase of Sb content, the band gap energy decreased and the index of refraction increased.

3

NONLINEAR OPTICAL CHARACTERIZATION OF GE-SB-SE PLANAR WAVEGUIDES

So far we have completed the fabrication and the linear optical characterization of the designed structures. In order to get a full understanding of the characteristics of selenide waveguides, we must study the nonlinear optical properties. Further, the ternary chalcogenide (Ge-Sb-Se) films that we chose to propagate solitons have not been intensively studied yet, most of the resarch works on ChGs are limited into the compositions of As_2S_3 [157], As_2Se_3 [158], Ge–As–S(Se) [159], and Ge–Sb–S [160, 161] and in bulk samples. The aim of this chapter is to investigate the third order nonlinear properties of the chalcogenide waveguides presented in the previous chapter. Towards this goal, an original and reliable experimental technique based on the analysis of beam self-action effect is also proposed.

Structure of the chapter is as follows. First we present the measurements of nonlinear propagation losses conducted in the three different selenide waveguides at 1550 nm and 1200 nm. Then we describe the technique developed to find the nonlinear coefficients. This section includes the description of the technique principle, presentation of the experimental set up as well as the experimental results and the numerical simulations. Formation of Kerr spatial soliton is also demonstrated. The following section concentrates on the experimental results of wavelength influence on self-focusing behaviour. The last section reports the photosensitivity of the chalcogenide waveguides under long illumination time.

3.1/ TPA LOSS MEASUREMENTS BY TRANSMISSION ANALYSIS

Nonlinear absorption losses such as TPA, three photon absorption can present in materials when it is subject to high intensities (typically at intensities approaching GW/cm^2). These effects are detrimental for some nonlinear optics applications particularly for all-optical switches because of the reduction in switching speed produced by the long-lived carriers and the limiting of optical power [184]. On the other hand, optical limiters or protectors in laser systems require materials with large TPA coefficients. Thus, measurements of nonlinear absorption coefficient is required. Importantly, to accurately determine the third order refractive index coefficient using the beam self-trapping technique that will be presented later we have to measure the TPA coefficients.

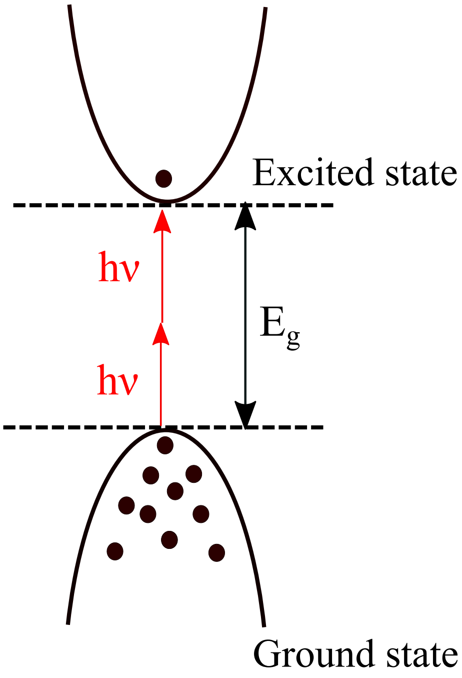

Figure 3.1: Illustration of the two photon absorption process.

The lowest order of a nonlinear absorption is TPA which involves a transition from the ground state of a system to a higher state by the absorption of two photons from an incident radiation field [185]. Illustration of the TPA process is presented in Fig. 3.1. TPA occurs when the incident photon energy $\hbar\omega$ is less than the direct band gap energy but greater than $E_g/2$ of the material. Since the photon energy at the excitation wavelength (e.g., 0.8 eV at 1550 nm and 1 eV at 1200 nm) is less than or close to half the band gap (Se6-0.85 eV, Se4-0.93, Se2-1.05) of the fabricated waveguides, they exhibit low or moderate TPA only. Hence, we can neglect the possibilities of higher order nonlinear absorption. Different techniques have been developed to determine the TPA coefficients of the materials. The simplest and most used is known as direct methods, in which the attenuation of the excited beam is monitored and indirect method, in which the secondary effects of TPA such as fluorescence, phosphorescence in the sample is measured [186]. In our case, we chose a direct method to analyse the contribution of TPA loss in the selenide waveguides at the wavelengths of 1550 nm and 1200 nm.

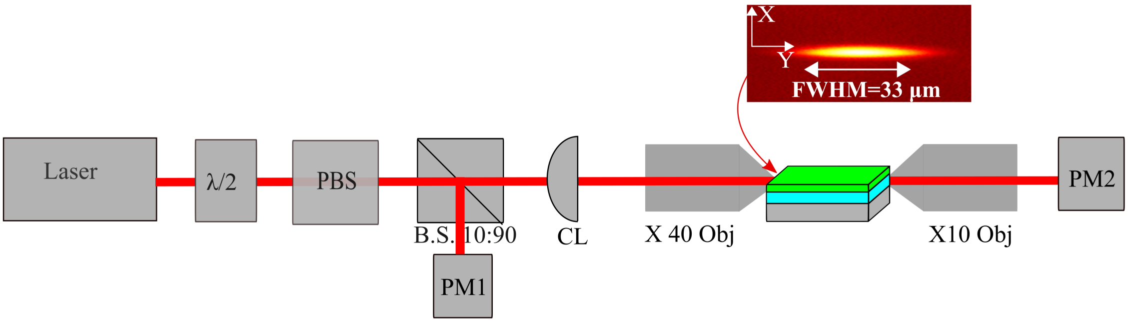

Figure 3.2: Schematic illustration of TPA measurement setup. $\lambda/2$, half-wave plate; PBS, polarizing beam splitter; CL, cylindrical lens; Obj, microscope objective; PM, power meters.

In order to evaluate the TPA coefficients of the planar waveguides at both wavelengths, transmission versus launched optical power is recorded. Schematic illustration of the experimental setup designed to measure the TPA coefficients is shown in Fig. 3.2. Experiments are performed with a 200 fs laser pulses from a tunable optical parametric oscillator (OPO) with a repetition rate of 80 MHz. The OPO is tuned to operate either at 1550 nm or 1200 nm. A small amount of incident power (10%) is split out by a beam splitter to monitor the input power to the sample using a power meter (PM1). The laser beam is reshaped to an elliptical spot by a cylindrical lens and focused by a ×40 microscope objective. The spot size at the entrance of the waveguide at a wavelength of 1.55 μm is 4×33 μm (FWHM) in the guided (X) and transverse dimension (Y), respectively and measured with an acquisition software connected to an IR camera. Note that the spot size is slightly smaller at 1200 nm (3.3 × 27 μm) in accordance with the wavelength dependence. The sample is mounted on an XYZ translation stage to get the maximum light coupling. The combination of a half-wave plate and a polarizer is used to vary the coupled power while the second power meter (PM2) allows measurement of the output power.

We have monitored the light power before and after the waveguide to deduce the transmission as a function of injected power using the setup mentioned above. The measurements are repeated several times at different positions in the sample to minimize experimental errors. Fresnel losses at the input of the waveguide are taken into account to deduce the incident intensity. Fig. 3.3 represents the typical transmission curves as a function of input intensity in the three selenide waveguides at 1550 nm (Fig. 3.3(a)) and 1200 nm Fig. 3.3(b). As can be seen in Fig. 3.3, TPA becomes dominant at high input intensity and limits the maximum transmitted power. We observed higher reduction of transmitted power in Se6 thin films at both the wavelengths. Whereas reduction in the

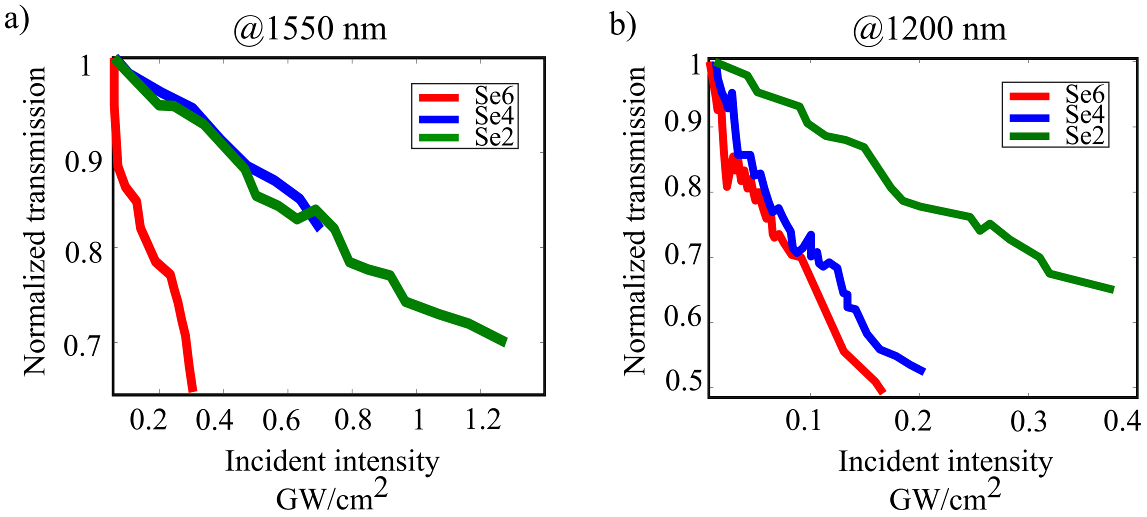

Figure 3.3: Normalized transmission as a function of intensity: for Se6 (red solid line), Se4 (blue solid line) and Se2 (green solid line) at 1550 nm (a) and 1200 nm (b).

transmitted power was lower for Se2 films.

The nonlinear absorption coefficient is then deduced by fitting the experimental data with the following equation which gives the normalized transmission as a function of input peak intensity I_0 [60]:

$$T_N = \frac{T}{T_{\text{max}}} = \frac{1}{\frac{1}{\alpha_1}[\alpha_1 + \alpha_2 I_0 (1 - \exp(-\alpha_1 l))]} \tag{3.1}$$

where T is the transmission, α_1 and α_2 are the linear and nonlinear absorption coefficients and l is the sample length. An examples of data fitting (using Eq. (3.1)) done in a 1 cm long Se6, Se4 and Se2 sample at 1550 nm and 1200 nm are shown in Fig. 3.4. The red circles represents the experimental data while the solid blue line is the fitting curve. The agreement between the experimental data and the fitted curve confirms that the power reduction effect is due to TPA. The fitting coefficient α_2 obtained for the different waveguides are given in Table. 3.3.

Table 3.1: TPA coefficients of the selenide waveguides

Sample	λ (nm)	α_2 $(cm.GW^{-1})$
x=50/Se6	1550	1.66 ± 0.18
	1200	5.5 ± 0.8
x=30/Se4	1550	0.37 ± 0.05
	1200	5.4 ± 0.6
x=10/Se2	1550	0.43 ± 0.06
	1200	2.7 ± 0.4

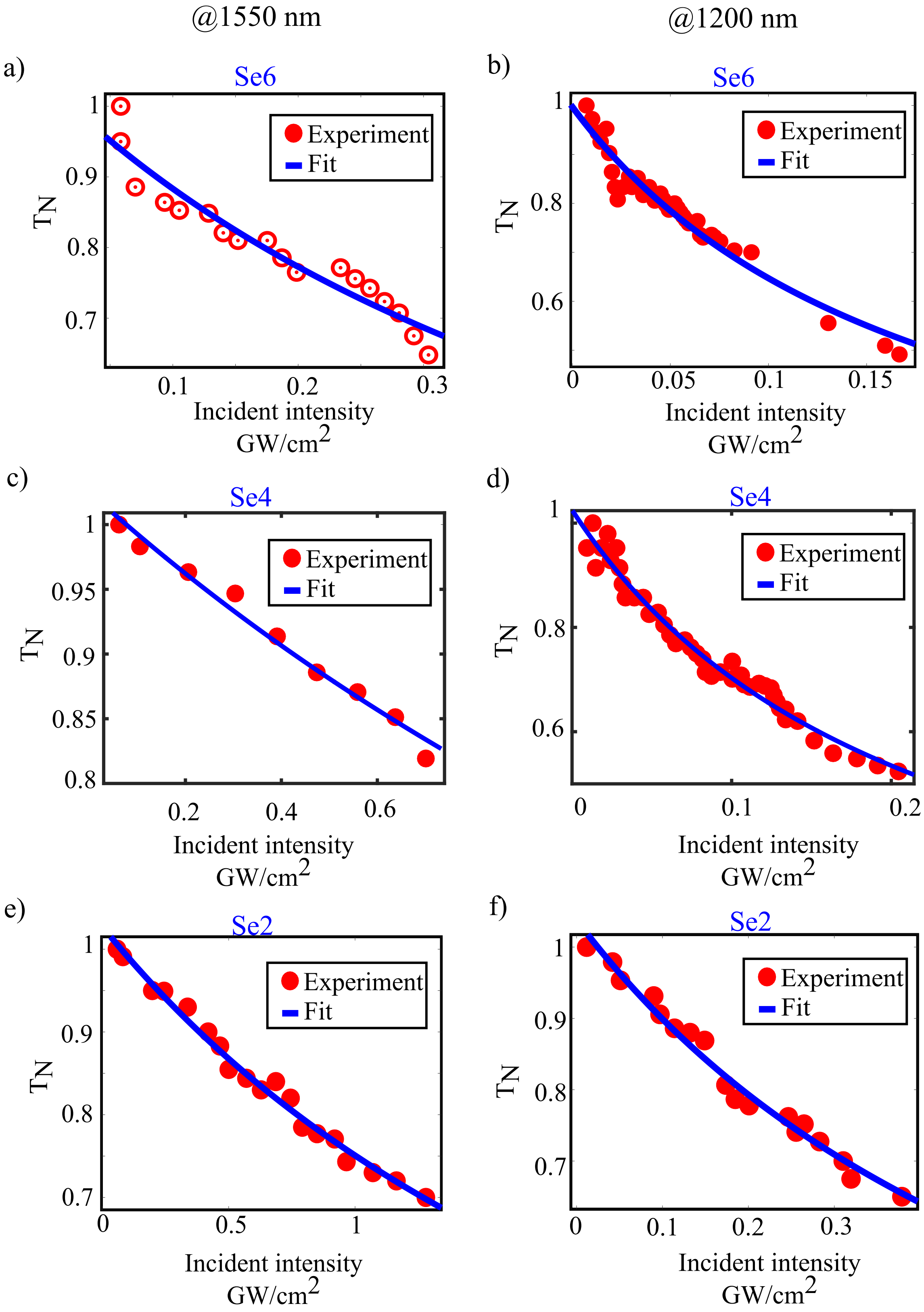

Figure 3.4: TPA curve fit done in a 1 cm long selenide films at 1550 nm and 1200 nm. (a, b) Se6, (c, d) Se4, and (e, f) Se2. Red circles: experimental data, Blue lines: data fitting.

From the results it is evident that TPA coefficients increases when the E_g of the selenide thin films becomes closer to the photon energy of the excitation wavelength. As expected the largest TPA coefficients are measured at 1200 nm. The values obtained at the wavelength of 1550 nm is low in the three compositions. However, measurement uncertainty of TPA is too large to conclude. It is however important to note that the values estimated for similar composition than Se4 and Se2 by Petit et al. [187] at 1064 nm are in good agreement with the values we found at 1200 nm. They have measured that α_2 varies from (1.6 ± 0.2) cm.GW^{-1} to (4.9 ± 0.6) cm.GW^{-1} depending upon the Ge-Sb-Se composition. TPA is weak at 1550 nm in Se2 and Se4 with values consistent with measurements performed in bulk samples of similar composition by transmission analysis [148] and by Wang *et al.* by open aperture Z-scan [169] given in Table. 3.3. The values obtained from the best fits range from 0.37 cm/GW (Se4 at 1550 nm) to 5.5 cm/GW (Se6 at 1200 nm) depending on the composition. These values are approximately 3 times smaller than the TPA value measured in selenide strip waveguides at 1030 nm with 7 ps pulses by an Yb-doped fiber laser [171].

3.2/ MEASUREMENTS OF ULTRAFAST OPTICAL NONLINEARITY

As stated in chapter 1, different mechanisms such as bound electronic motion, two-photon free-carrier generation, molecular Kerr reorientation, photo refractive effect, thermal effects etc. can contribute to a change in index dependent on intensity [188]. The nonlinearities that arise from these mechanisms possess different response times and can be associated to an equivalent n_2. As is seen in table. 3.2, electronic nonlinearities are fast and it is resulting from the instantaneous change in polarization density to the optical electric field. On the other hand thermal effect implies a long excitation and relaxation time. It can be induced optically and cause a change in refractive index due to an increase of the temperature due to material absorption. Importantly, to make a material useful for future photonic devices an ultrafast electronic response is desired.

Table 3.2: Characteristics of optical nonlinearities according to their physical process [1]

Mechanism	n_2 (cm^2/W)	Response time (sec)
Electronic polarization	10^{-16}	10^{-15}
Molecular orientation	10^{-14}	10^{-12}
Electrostriction	10^{-14}	10^{-9}
Saturated atomic absorption	10^{-10}	10^{-8}
Thermal effects	10^{-6}	10^{-3}
Photorefractive effect	large	(intensity-dependent)

The following sections present the experimental results of nonlinearity measurements conducted in the three different selenide waveguides at the wavelengths of 1550 nm and 1200 nm as well as details of the mechanism (thermal or electronic) that contribute to the change in refractive index of the material. Furthermore, we will introduce a new technique to measure the optical nonlinearity in very thin layers of planar waveguides. The real motivation to develop a new experimental technique is given in the following section.

3.2.1/ Techniques for the determination of n_2

The characterization of nonlinear optical properties have an important role in modern photonic functionalities including ultrafast all optical signal processing, short pulse generation and wavelength conversion. Different techniques have been employed to determine the third order nonlinear optical constants of bulk/film samples including self-phase modulation (SPM) [189], Mach-Zehnder technique (MZT) [190], degenerate four wave mixing (DFWM) [157], two-photon absorption spectroscopy [191], optical Kerr gate [192] and z-scan [193].

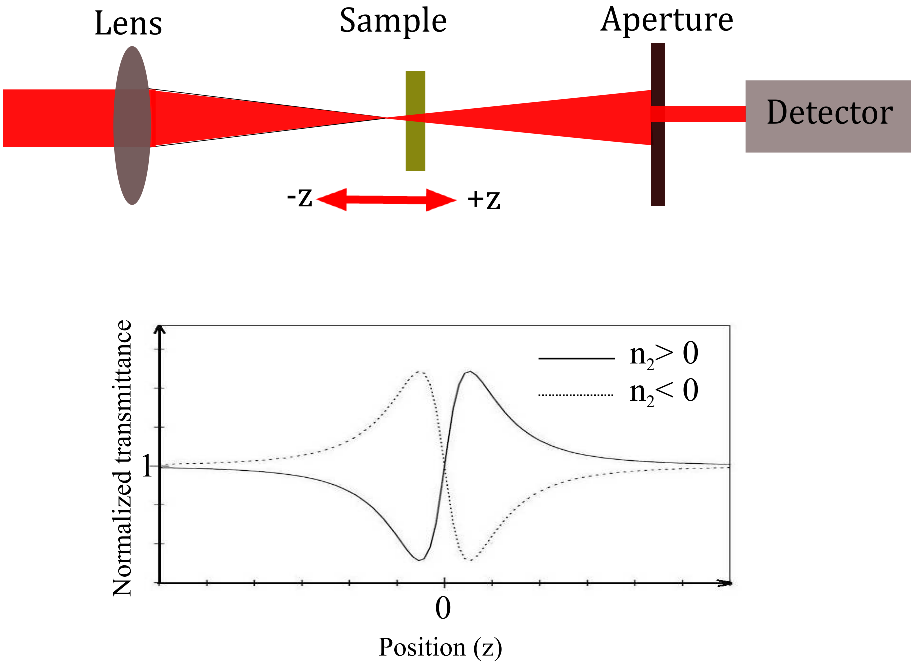

Figure 3.5: Schematic illustration of a z-scan technique (top) and the transmission versus position z-scan curve [194] (bottom).

The latter technique is the most widely used one and is appropriate to characterize both bulk material and thin films. The z-scan [193] is suitable to determine both the real and imaginary part of the nonlinear refractive index. This method is based on the analysis of the diffraction modification due to nonlinear effect of a beam focused in the sample under study while the sample is scanned along the z-direction as shown in Fig. 3.5 (top).

The transmitted light by a small aperture is then measured in the far field as a function of sample position z with respect to the focal plane of the focusing lens. If the material has a positive nonlinearity ($n_2 > 0$), the transmission versus position has a valley first and then peak (Fig. 3.5 (bottom). For a material with a negative nonlinearity ($n_2 < 0$) will produce an exactly reversed curve, first the peak and then the valley (Fig. 3.5 (bottom). One can determine the amplitude of n_2 from the transmission graph versus sample position. For accurate measurements, it requires samples with very good homogeneity. In addition, this technique cannot be used in very thin layers since the induced beam change becomes indiscernible. Moreover, the thin film under test is often deposited on a substrate that can perturb or prevent the measurement.

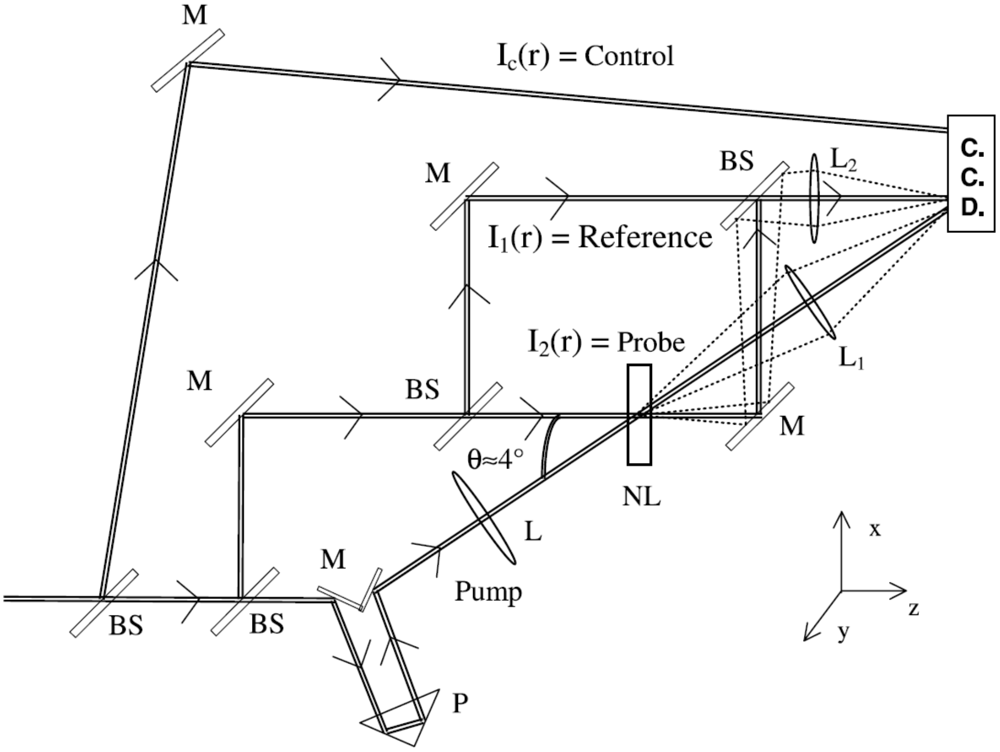

Figure 3.6: Schematic of Mach-Zehnder experimental setup: NL, nonlinear material; L, lenses; M, mirrors; BS, beam splitters. Figure taken from Ref. [190].

Unlike z-scan, a single laser shot is enough in MZT [190] technique to obtain a large number of measurements and to accurately estimate the nonlinear coefficients. Further, the risk of damage to samples is highly limited with single laser shot in the sample. The operating principle of MZT is explained by the experimental set up shown in Fig. 3.6. One beam of the Mach-Zehnder interferometer is used as a reference beam with intensity $I_{1(r)}$; a second beam is asses the area to be tested with an intensity $I_{2(r)}$. The nonlinear medium is then illuminated by a second pump beam focused with the aid of a lens. Then the interference pattern intensity due to the recombinations of the beams is recorded at the output of the sample using a CCD camera. When the nonlinear medium is excited by the pump beam, local fringe alteration is observed in the interference pattern due to the nonlinear dephasing and the amplitude change due to the nonlinear transmittance. The nonlinear dephasing allows the determination of n_2 and the TPA coefficient can be deduced from the amplitude of transmittance. Moreover, numerical treatment such as spatial Fourier transform on the acquired image permits both the characterization of poor optical quality sample and increase the precision of the measurements. But the great inconvenience of the MZT is the complexity of the optical setup. The poor optical quality of beam requires a day to day alignment of the optical setup which can be tedious.

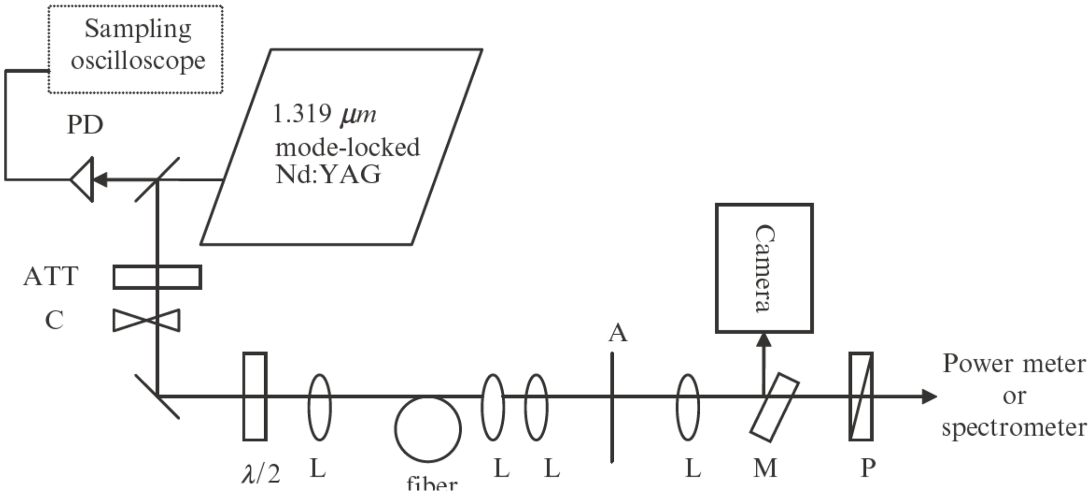

Figure 3.7: Schematic diagram of the experimental setup used for SPM technique. PD, pin-photodiode; ATT, attenuator; C, chopper; $\lambda/2$, half wave plate; L, lenses; A, aperture; M, glass plate; P, polarizer. Figure taken from Ref. [189].

Many techniques have also been developed to analyze nonlinearities in 2-D waveguides. For instance, the SPM technique [189], which is based on the analysis of the spectral broadening of a beam as a function of intensity and sample length, allows determination of nonlinear coefficients in 2-D waveguides or fibers. Schematic of the experimental setup for SPM is presented in Fig. 3.7. A pin-photodiode and a sampling oscilloscope is used to monitor the temporal-pulse profile. For instance a modelocked Nd:YAG laser can be used as the light source. The laser beam is injected into the waveguide/fiber with an objective lens. An intense pulse propagating through the nonlinear medium acquires a phase shift due to the nonlinear index of refraction. The self modulated pulses having a broadened spectrum of frequencies is then analysed at the output of the waveguide using an optical spectrometer. The n_2 coefficients can be deduced from the spectrum change. The main issues associated with SPM are an accurate measurement of peak intensity and an independent measurement of the effective area (Aeff) of the waveguide/fiber since the quantity actually measured by the SPM technique is $n_2/Aeff$.

Likewise, DFWM technique [157] is also well suited to analyse third order susceptibility tensor of 2-D waveguides. This is based on the temporal and spatial overlapping of three separate light pulses which allows an increased flexibility such as the possibility of measuring different tensor components of $\chi^{(3)}$, a straightforward study of temporal behavior, and less strict conditions on the beam profile and the surface roughness [195]. However, the complex experimental set up and the requirement of injection of synchronized pulses at different wavelengths limits the application.

Principally, none of these techniques is well suited to study nonlinear properties in very thin layers that form planar waveguides. So we propose a technique that is convenient to determine the Kerr effect in such structures. The method is based on the direct analysis of the influence of the non-linear effect on the spatial light distribution of a beam propagating in the slab waveguide. The proposed method has several merits. The experimental setup is simple and one laser shot could be sufficient to deduce the Kerr coefficient. The sensitivity is good especially when self-trapping leads to the formation of spatial soliton. The method can be used even in multimode waveguides and is relatively immune to perturbations due to the substrate. In addition, the proposed technique can be applied to characterize any materials that form a waveguide. The following section describes the principle of the proposed technique.

3.2.2/ PRINCIPLE OF BEAM SELF-TRAPPING TECHNIQUE

The characterization technique we propose is based on the analysis of beam self-action and more specifically on beam self-trapping to measure optical nonlinearities in planar waveguides. As described in chapter 1, section 1.1.3, beam self-trapping occurs when diffraction is counteracted by nonlinear index change induced by the beam itself [2]. Such an effect can even lead to the formation of a spatial soliton when the trapped beam propagates without changing its shape. The technique is used to characterize ultrafast nonlinear properties of three different selenide waveguides at 1550 and 1200 nm.

The proposed technique consists in focusing a pulsed laser at the input face of a slab waveguide while the beam profile is monitored with a camera at the output face. As shown in Fig. 3.8, if the launched beam is narrow, typically few 10's of micron wide, it clearly enlarges due to diffraction in the linear regime along few millimetres propagation distance. In the nonlinear regime, i.e., at higher power, diffraction is modified due to either self-focusing or self-defocusing.

To properly model the beam propagation, the effects of both linear and nonlinear absorption must be considered. The modified nonlinear Schrödinger equation (Eq. (1.24)) that includes absorption can be written as [122]:

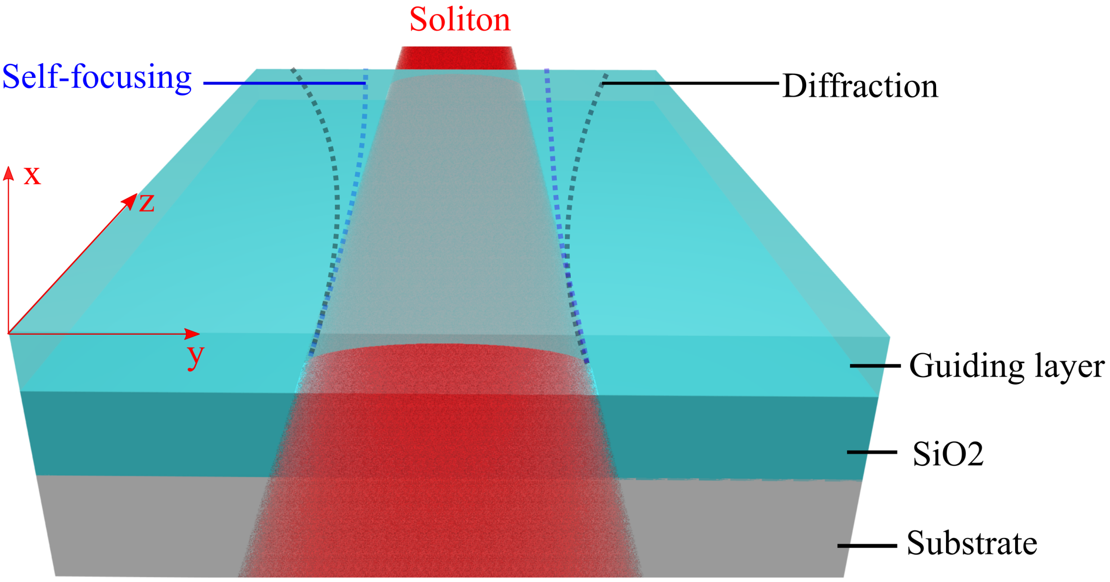

Figure 3.8: Beam propagation in the three layer planar waveguide.

$$\frac{\partial E(x,y,z)}{\partial z} - \frac{i}{2k}\frac{\partial^2 E(x,y,z)}{\partial y^2} + \frac{\alpha}{2}E(x,y,z) - i\frac{2\pi}{\lambda}n_2 I E(x,y,z) = 0 \tag{3.2}$$

Here $E(x,y,z)$ is the beam electric field distribution and is related to the beam intensity distribution by $I = \frac{1}{2}c\epsilon_0 n|E^2|$. x and y are the coordinates perpendicular and parallel to the chalcogenide layer, respectively, and z is the coordinate associated to the propagation direction. The second term of Eq. 3.2 corresponds to diffraction that only occur along y since the beam is guided along x-axis. The third term accounts for absorption α expressed as $\alpha = \alpha_1 + \alpha_2 I$, α_1 and α_2 being the linear and TPA coefficients respectively. The contributions of three-photon and higher order absorption are neglected [128]. Thus, the equation describing the evolution of the pulse with linear and TPA can be defined as:

$$\frac{\partial E(x,y,z)}{\partial z} - \frac{i}{2k}\frac{\partial^2 E(x,y,z)}{\partial y^2} + \frac{\alpha_1}{2}E(x,y,z) + \frac{\alpha_2}{2}IE(x,y,z) - i\frac{2\pi}{\lambda}n_2 I E(x,y,z) = 0 \tag{3.3}$$

The last term of Eq. (3.3) accounts for the contribution of the Kerr nonlinearity. For a positive n_2 coefficient and within certain power constraints, self-focusing effect can compensate for diffraction and the fundamental solution of Eq. (3.3) leads to a spatial soliton [128]. In our work, the Kerr coefficient will be deduced by fitting the experimental results with simulations given by the nonlinear Schrödinger equation Eq. (3.3) solved with a beam propagation method (BPM: a numerical method for evaluating the evolution of optical fields in waveguides) [196].

3.2.3/ EXPERIMENTAL SETUP

As mentioned in the previous section, following parameters have to be identified to extract optical nonlinearity by employing the beam self-trapping technique:

- input beam size for each wavelength.
- output beam size as a function of intensity
- linear refractive index (n_0)
- propagation length (l)
- linear and nonlinear absorption coefficients for greater accuracy.

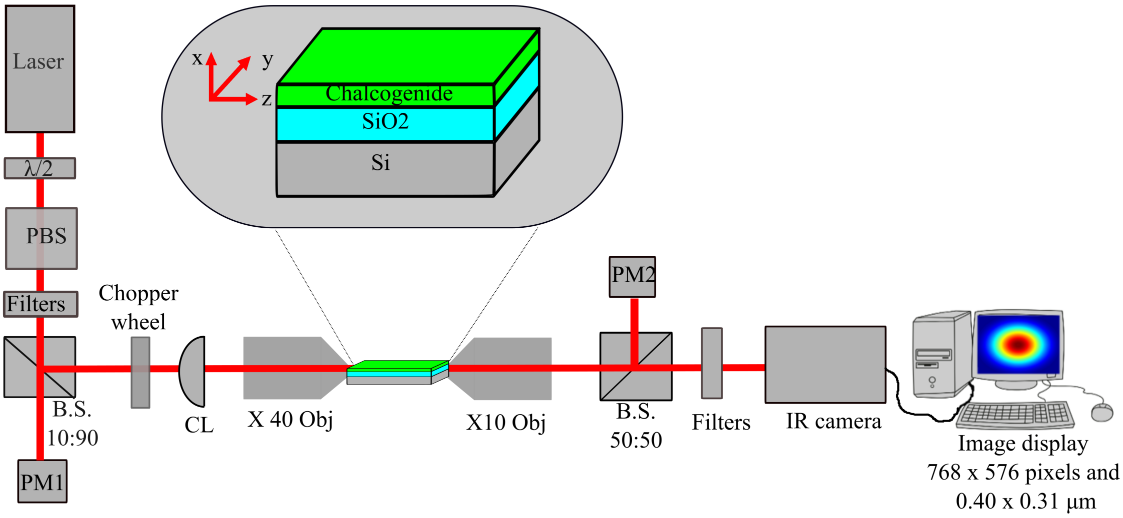

Figure 3.9: Experimental setup used to analyze the beam self-action in chalcogenide planar waveguides. $\lambda/2$, half-wave plate; PBS, polarizing beam splitter; CL, cylindrical lens; Obj, microscope objective; PM, power meters; B.S, beam splitter.

The experimental setup used for TPA measurements is thus modified with the introduction of a vidicon camera and an optical chopper as shown in Fig. 3.9. The laser system and the optical components are the same as in the setup of Fig. 3.2. The impact of the cumulative thermal effect is excluded with an optical chopper. Samples are kept on an XYZ translation stage to provide the maximum light coupling. The spot size of 4.3×33 μm (FWHM) at 1.55 μm and 3.3×27 μm at 1200 nm allows efficient end fire coupling to the fundamental mode of the waveguide. A coupling efficiency of $\sim 21\%$ is measured in our waveguides at the wavelength of 1550 nm. Beam distribution at the output face of the chalcogenide film as a function of intensity is monitored with a vidicon camera (the size in the image plane corresponding to 768 x 576 pixels is 0.40 x 0.31 μm) using a ×10 microscope objective. The experimental demonstration of beam self-action effects is presented in the following section.

3.2.4/ FORMATION OF SPATIAL SOLITONS IN THE SLAB WAVEGUIDES

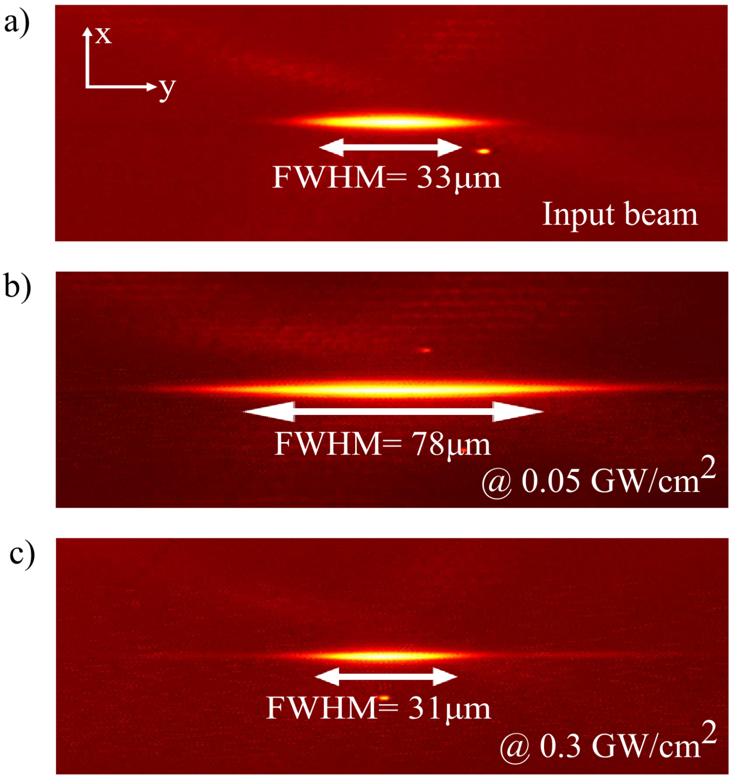

Figure 3.10: Experimental images of beam self-action analysis within a 1 cm long Se6 planar waveguide. (a) Input beam injected into the waveguide, (b) diffracted output beam in linear regime for an intensity of 0.05 GW/cm^2, (c) output self-trapped beam near soliton propagation with a peak intensitiy of 0.30 GW/cm^2.

We have performed the experiments in the three selenide waveguides at two different wavelengths. A typical observation made in a 1 cm long Se6 slab waveguide at 1550 nm is depicted in Fig. 3.10. Fig. 3.10(a) shows the shape of the beam at the entrance of the waveguide whose horizontal size is 33 μm FWHM. At low incident intensity, the beam propagates in linear regime and diffracts freely to give an output beam whose FWHM is about 78 μm (Fig. 3.10(b)). As we increase the input peak intensity, we observe a beam narrowing which reveals a positive n_2 coefficient. Adjustment of the beam input peak intensity to 0.30 GW/cm^2 even leads to the formation of a trapped beam close to a spatial soliton as depicted in Fig. 3.10(c). Formation of Kerr spatial soliton is confirmed when the input and output beam profiles are similar. In such a situation, diffraction and self-focusing compensates each other. Note that, the intensity required to form soliton is very low in this composition. Thus a strong Kerr coefficient can be expected.

Similar experiments have been performed in Se4 and Se2 samples at 1550 nm and 1200 nm. Fig. 3.11 represents the evolution of the output beam FWHM as a function of the input intensity for the three waveguides at 1550 nm (Fig. 3.11(a)) and 1200 nm (Fig.

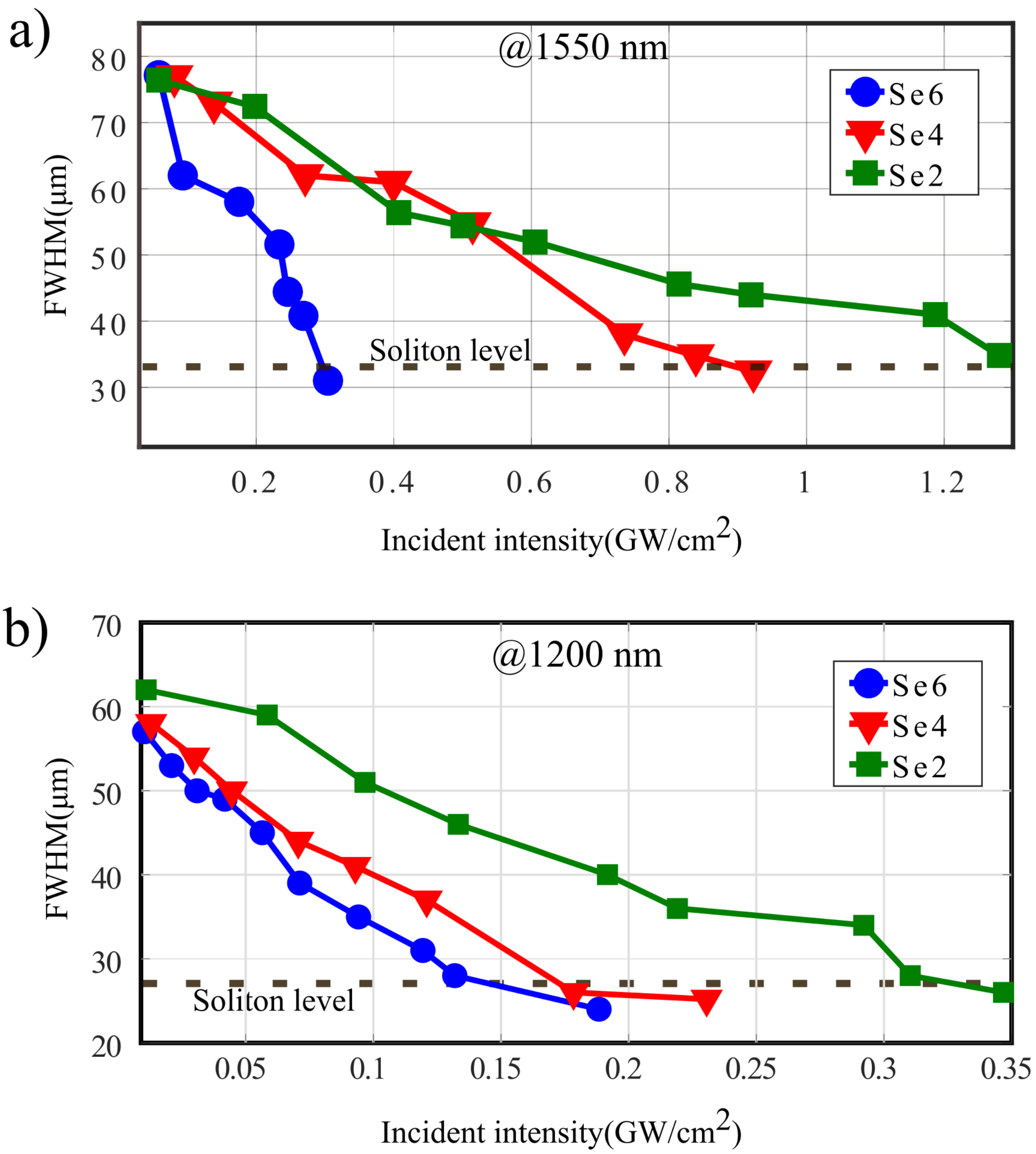

Figure 3.11: Measured output beam FWHM as a function of incident intensity in the three-selenide compositions: (a) at 1550 nm, (b) at 1200 nm.

3.11(b)). Since they are all about 1 cm long, diffraction regimes are similar. At low incident intensity, output beam diffracts to give a beam, which is 2.4 times larger than the input beam. For all samples, self-trapping is observed ($n_2 > 0$) and soliton formation can be reached. Soliton is formed at input peak intensities of 0.30 GW/cm^2 for Se6, 0.83 GW/cm^2 for Se4 and 1.28 GW/cm^2 for Se2, respectively at 1550 nm whereas the intensity required to form soliton at 1200 nm is 0.14 GW/cm^2 for Se6, 0.24 GW/cm^2 for Se4 and 0.35 GW/cm^2 for Se2. Note that to prevent input facet damage we voluntarily did not go beyond the soliton power in the tested samples.

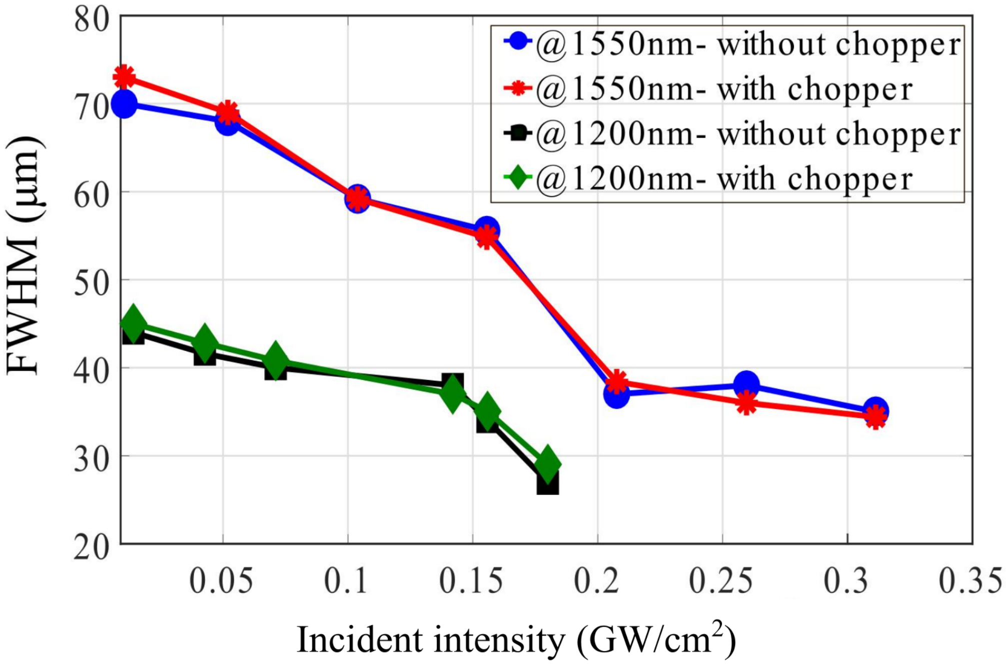

Figure 3.12: Evolution of output beam FWHM as a function of intensity in Se6 at 1550 and 1200 nm with and without optical chopper.

Since our measurements are made with a high repetition rate laser (80 MHz), it is important to evaluate the contribution of potential thermal effect or photo-induced effects that could be present in addition to the instantaneous electronic nonlinearity. Following the literature [197, 198, 199], we performed experiments with an optical chopper in order to lower the average power while maintaining the peak power. A chopping frequency of 1000 Hz and a duty cycle of 28% was used. Fig. 3.12 depicts the self-focusing behavior versus intensity in the Se6 sample with and without the chopper at both 1550 nm and 1200 nm. Note that the Se6 composition has the lowest bandgap energy and consequently the strongest absorption which should favour appearance of the thermal effect. Within the experimental errors, no change in FWHM beam behaviour is observed despite an average power divided by more than 3.5 times with the chopper compared to without chopper. It clearly demonstrates that thermal effect can be neglected in these glasses when working at near infra-red wavelengths with our femtosecond laser system. Furthermore, we have also verified that the self-focusing effect is reversible when we switched from high intensity to low intensity. It proves that no permanent modification of refractive index that could be due to the glass photosensitivity [140] is induced during the experiment. We have also confirmed the absence of thermal or photosensitivity effect in Se4 and Se2 samples.

While previous measurements are standard, the originality of our method to determine the coefficient n_2 is based on the beam self-action analysis. This will be presented in the next section along with examples.

3.2.5/ n_2 MEASUREMENTS BY THE BEAM SELF-TRAPPING TECHNIQUE

The experimental self-action regime is modelled using Eq. (3.3) to deduce the Kerr coefficient. Accuracy is however higher when the nonlinear regime reveals an obvious change in the experimental output profile. As an example we will consider the beam self-action effect observed in Se6 sample at first.

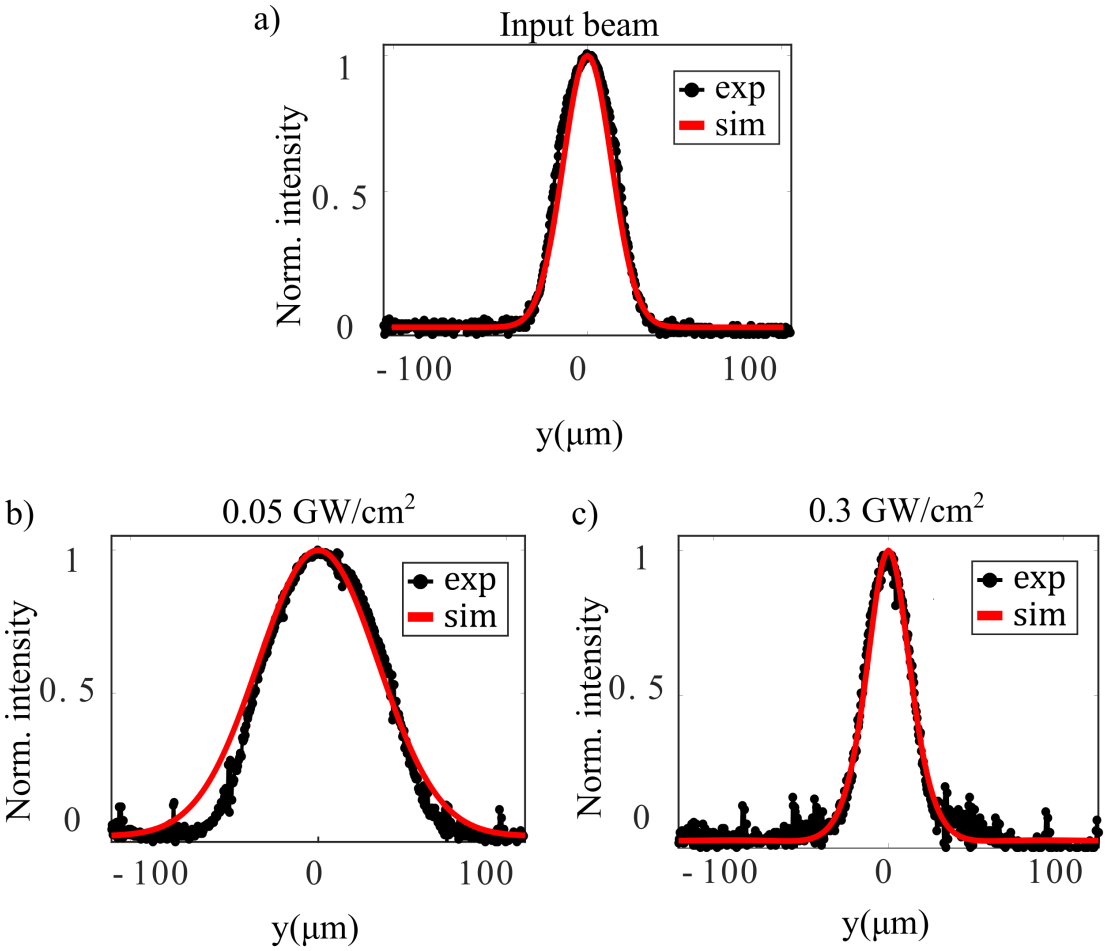

Figure 3.13: Comparison between experimental and numerical beam profiles of beam self-action analysis as a function of input intensity within a 1 cm long Se6 planar waveguide. (a) Input beam, (b) output beam in linear regime for an intensity of 0.05 GW/cm^2, (c) output beam in nonlinear regime for an incident intensity of 0.30 GW/cm^2. Circles and solid line profiles correspond to experimental and numerical fits, respectively.

We thus chose to consider the soliton regime for the fitting using the numerical simulations given by Eq. (3.3). The coefficient being the only free variable while absorption coefficients are taken from the previous section. More precisely, we look for the n_2 coefficient that predicts the experimental results numerically by the BPM method. A Gaussian input beam profile of identical width and same peak intensity than the experimental one is considered at the input of the numerical simulation. For instance, the solid lines in Fig. 3.13(a), (b) show the fitted beam profile in linear regime, respectively at the entrance and at the exit face of the 1 cm long Se6 sample at 1550 nm. Fig. 3.13(c) depicts the output beam profile in soliton regime for an input peak intensity I_0 = 0.30 GW/cm^2, α_2 = 1.66 cm.GW $^{-1}$, α_1 = 0.26 cm^{-1}, and n_2 = 17 x 10^{-18} m^2. W^{-1}. The numerical simulation results give a beam FWHM of 31.5 μm, 79 μm and 31.5 μm respectively for input beam, diffracted output beam in linear regime and soliton beam profiles, which are in good agreement with the experimental beam profiles as shown in Fig. 3.13.

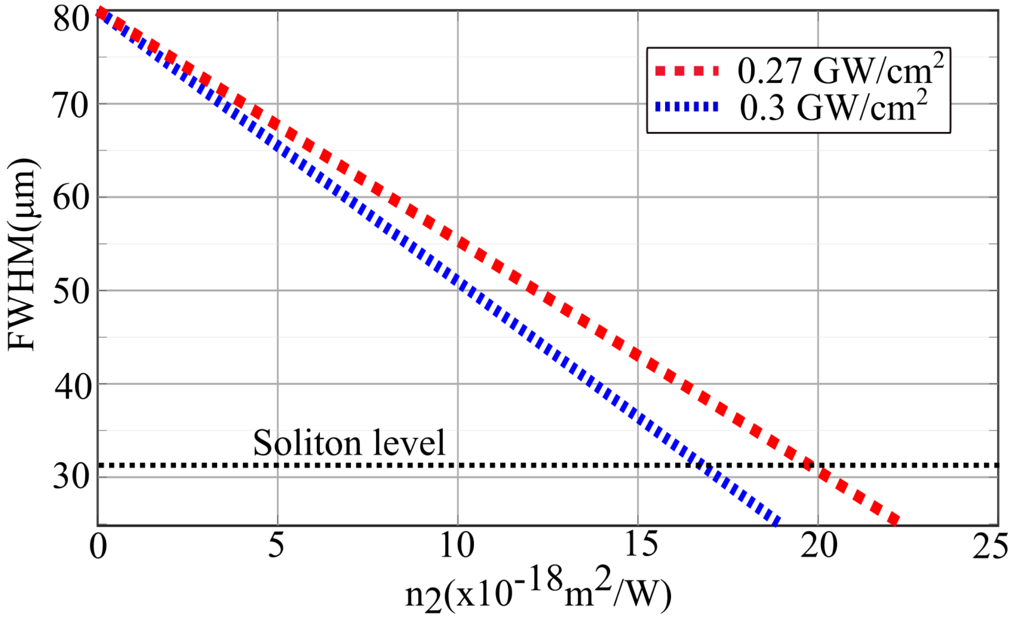

Figure 3.14: Computed output beam FWHM versus nonlinear refractive index for two different input intensity in Se6 chalcogenide waveguide. Parameters: Input beam FWHM = 33 μm, linear refractive index = 2.9, λ = 1550 nm, α_1 = 0.26 cm^{-1}, α_2 = 1.66 cm/GW, waveguide length = 1 cm.

Further increase of intensity leads to the formation of side wings and beam breakup. This could be explained by considering the contribution of TPA at high intensity [200, 201]. Moreover, waveguide facet damage occurs when the excitation intensity exceeds 0.82 GW/cm^2 for Se6 samples at 1550 nm. Two experimental parameters lead to some uncertainty in the evaluation of n_2, the input beam FWHM and the input beam intensity. The beam width uncertainty is about 2 μm while the uncertainty of the incident intensity is evaluated to be 10%. So, we first deduced n_2 corresponds to soliton formation intensity with the parameters of input beam FWHM, n_0, λ, α_1 and α_2. Then we calculated n_2 coefficients for an input peak intensity, which is 10% above and below the soliton intensity. Fig. 3.14 shows the calculated beam FWHM at the exit face of a 1 cm long waveguide as a function of n_2 coefficient for two different incident intensities. Dependence of the expected FWHM versus n_2 is found to be linear. The estimated uncertainty on intensity dependent n_2 is 17.6% for Se6.

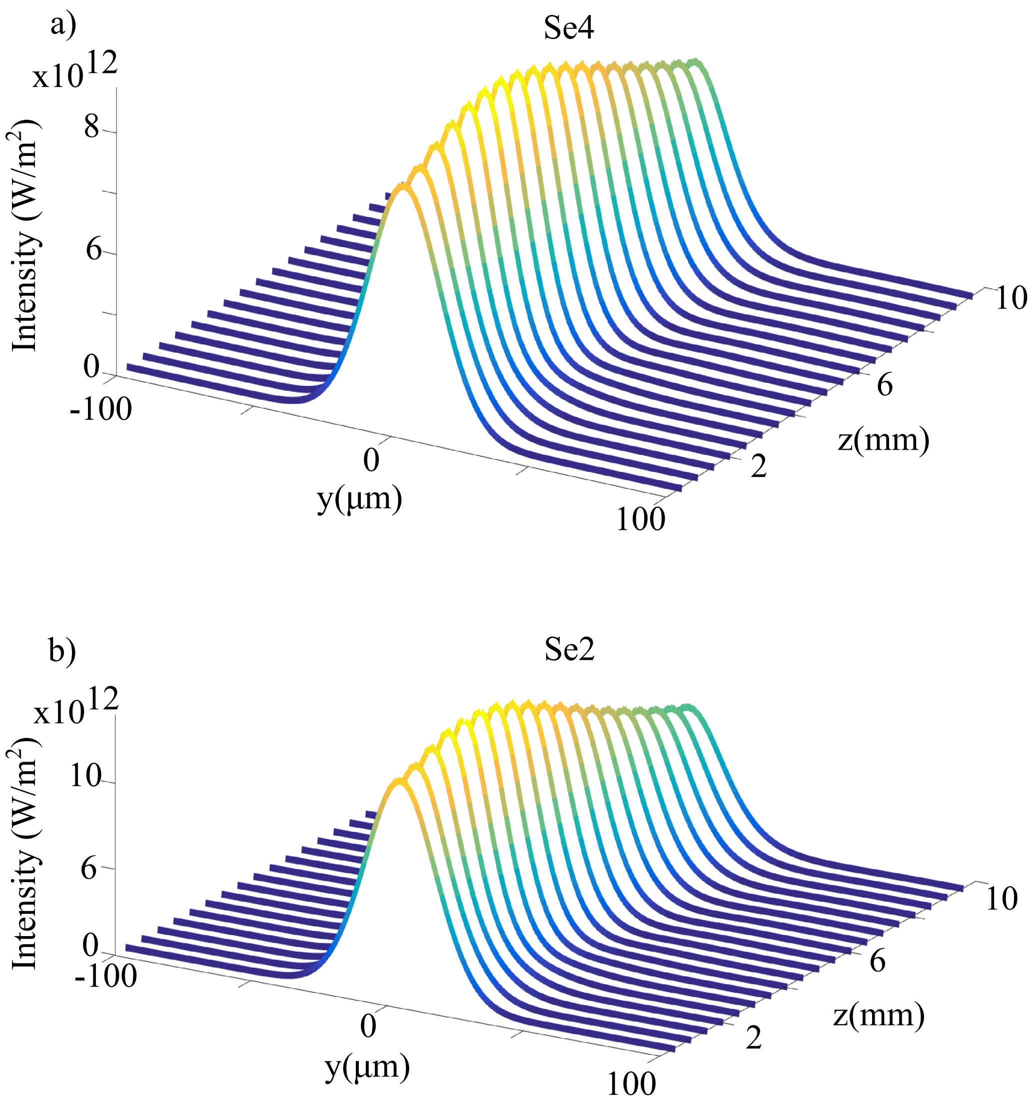

Figure 3.15: Simulated beam evolution corresponding to soliton propagation in a 1 cm long sample at λ = 1550 nm: In Se4 films for an input intensity of 0.8 GW/cm^2 (a), material parameters used are n_2 = 8 x 10^{-18} $m^2.W^{-1}$, α_1 = 0.24 cm^{-1}, α_2 = 0.37 cm/GW; in the Se2 films for an input intensity of 1.28 GW/cm^2 (b), material parameters used are n_2 = 5.5 x 10^{-18} $m^2.W^{-1}$, α_1 = 0.19 cm $^{-1}$, α_2 = 0.43 cm/GW^{-1}.

In addition , simulated beam evolution corresponding to the soliton propagation for Se4 and Se2 is depicted in Fig. 3.15. The intensity dependent changes in refractive index of the medium are attributed to the Kerr effect. As seen in Fig. 3.15(a) and 3.15(b), the reduction in intensity of the self-trapped beam is due to the nonlinear absorption. Comparison of BPM simulations with experimental results leads to a nonlinear index n_2 of 8 x 10^{-18} $m^2.W^{-1}$ with α_2=0.37 cm/GW for Se4 and n_2 of 5.5 x 10^{-18} $m^2.W^{-1}$ with α_2=0.43

cm/GW^{-1} for Se2.

The same technique is used to characterize the nonlinear properties of our selenide waveguides at 1200 nm (Fig. 3.11(b)). Since strong self-trapping and soliton formation is observed for an intensity lower than 1550 nm we can expect large nonlinear index coefficients at 1200 nm. Table. 3.3 summarizes the results of optical constant measurements for the three studied planar chalcogenide waveguides at the two different wavelengths. The measurements showed that both n_2 and TPA are smaller in Se2 in accordance with its larger band gap than Se4 and Se6.

Table 3.3: Measured values of the optical coefficients in the three chalcogenide waveguides at 1550 nm and 1200 nm. To validate the measurements, optical coefficients of the chalcogenide glases/waveguides obtained by other techniques are presented (BSA, beam self-trapping analysis (present study); DTA, direct transmission analysis; SRTBC, spectrally resolved two beam coupling.

Sample	λ (nm)	$\alpha_1(cm^{-1})$	$\alpha_2(cm.GW^{-1})$	$n_2(10^{-18}m^2.W^{-1})$	Method and references
Se6/$Ge_{12.5}Sb_{25}Se_{62.5}$					
Slab waveguide	1550	0.26	1.66 ± 0.18	17.0 ± 3	BSA
Slab waveguide	1200	0.76	5.5 ± 0.8	32.0 ± 5	BSA
Bulk	1550	0.20	0.84	20.3 ± 3	DTA [148]
Se4/$Ge_{19.4}Sb_{16.7}Se_{63.9}$					
Slab waveguide	1550	0.24	0.37 ± 0.05	8 ± 2	BSA
Slab waveguide	1200	0.71	5.4 ± 0.6	21.5 ± 3	BSA
Bulk	1550	0.15	0.31	9.97 ± 2	DTA [148]
Se2/$Ge_{28.1}Sb_{6.3}Se_{65.6}$					
Slab waveguide	1550	0.19	0.43 ± 0.06	5.5 ± 2	BSA
Slab waveguide	1200	0.63	2.7 ± 0.4	14 ± 3	BSA
Bulk	1550	0.15	0.29	9.0 ± 2	DTA [148]
$Ge_{29.9}Sb_{15.6}Se_{54.5}$ (waveguide)	1064	0.806-0.852			[183]
$Ge_{23}Sb_7Se_{70}$ (bulk)	1064		2.4		z-scan [187]
$Ge_{28}Sb_7Se_{65}$ (bulk)	1064		4.9 ± 0.6		z-scan [187]
$Ge_{23}Sb_7Se_{70}$(ridge waveguide)	1550			3.71	SPM [202]
Ge-Sb-Se (bulk)	1150-1686		0.05-7.44	7.33-20.3	z-scan [169]
As_2Se_3	1500			19	z-scan [155]
	1250		2.8 ± 0.4	30 ± 4.5	SRTBC [203]
As_2S_3 (bulk)	1250		0.16 ± 0.02	6.8 ± 1.0	SRTBC [203]

To validate our method, we compare our values with the ones obtained by other techniques. The experimental n_2 values obtained for Se4 and Se2 waveguides by the beam self-trapping analysis at 1550 nm are close to the values obtained in bulk samples of similar composition (See Table. 3.3) characterized by the Z-scan techniques [148]. In addition, our n_2 values measured for Se4 and Se2 are consistent with the values reported by Dai *et al.* in Ge-Sb-Se ternary system using the Z-scan technique in femtosecond regime [168]. They estimated values of n_2 vary from 5.3 x 10^{-18} m^2/W to 19 x 10^{-18} m^2/W at 1550 nm for different compositions of Ge-Sb-Se glasses. A recent paper [202] reported the nonlinear characterization of a $Ge_{23}Sb_7S_{70}$ ridge waveguide using the self-phase modulation to be 3.71 × 10^{-18} m^2/W at the wavelength of 1550 nm. In Ge-Sb-Se samples, we obtained n_2 as high as (17 ± 3) x 10^{-18} m^2/W at 1550 nm and (32 ± 5) x 10^{-18} m^2/W at 1200 nm for the sample with the smallest bandgap. This is in accordance with a nonlinearity four times larger in As_2Se_3 than in As_2S_3 [203, 155]. This clearly reveals that, n_2 increases as selenium is substituted for sulfur atoms. Moreover, n_2 increases as material bandgap decreases. This trend is consistent with values reported by Wang *et al.* where the wavelength was tuned from 1150 nm to 1686 nm [169]. It is also important to note that some properties of the bulk materials such as the chemical composition, the band gap energy and the refractive index are known to slightly differ from properties of deposited films [204]. Consequently, nonlinear optical properties of bulk target and deposited films do not exactly match. Nonetheless, the intensity dependent n_2 values measured by the beam self-trapping analysis follows the same trends than the one estimated by the z-scan method in Ge-Sb-Se glasses. All results validate our original technique.

3.2.6/ SELF-FOCUSING VERSUS WAVELENGTH

Nonlinear optical properties of chalcogenide glasses are very dependent on wavelength. We thus propose to perform a nonlinear characterization of Ge-Sb-Se on a wide wavelength range. Few results have been recently published for this material [168, 171]. These literatures have well characterized the nonlinear properties of chalcogenide glasses at shorter wavelength (1030 nm) [171] and mid-infrared wavelengths (2000 nm and 2500 nm) [168] by z-scan technique. Since the studies are on a fixed wavelength, a step by step wavelength varying study is necessary to understand the influence of wavelength on the propagation of self-trapped beam. In this section, we report the optical characterization of the waveguide Se2, by tuning the wavelength from 1200 nm to 1570 nm.

Input beam width is similar than in the previous experiment from Fig. 3.10(a). Output beam profile of best self-focusing behavior (strongly focused central beam) for different wavelength and its influence on power is depicted in Fig. 3.16. We note that self-focusing is observed for all tuned wavelengths. However, an almost clean or distinguishable beam

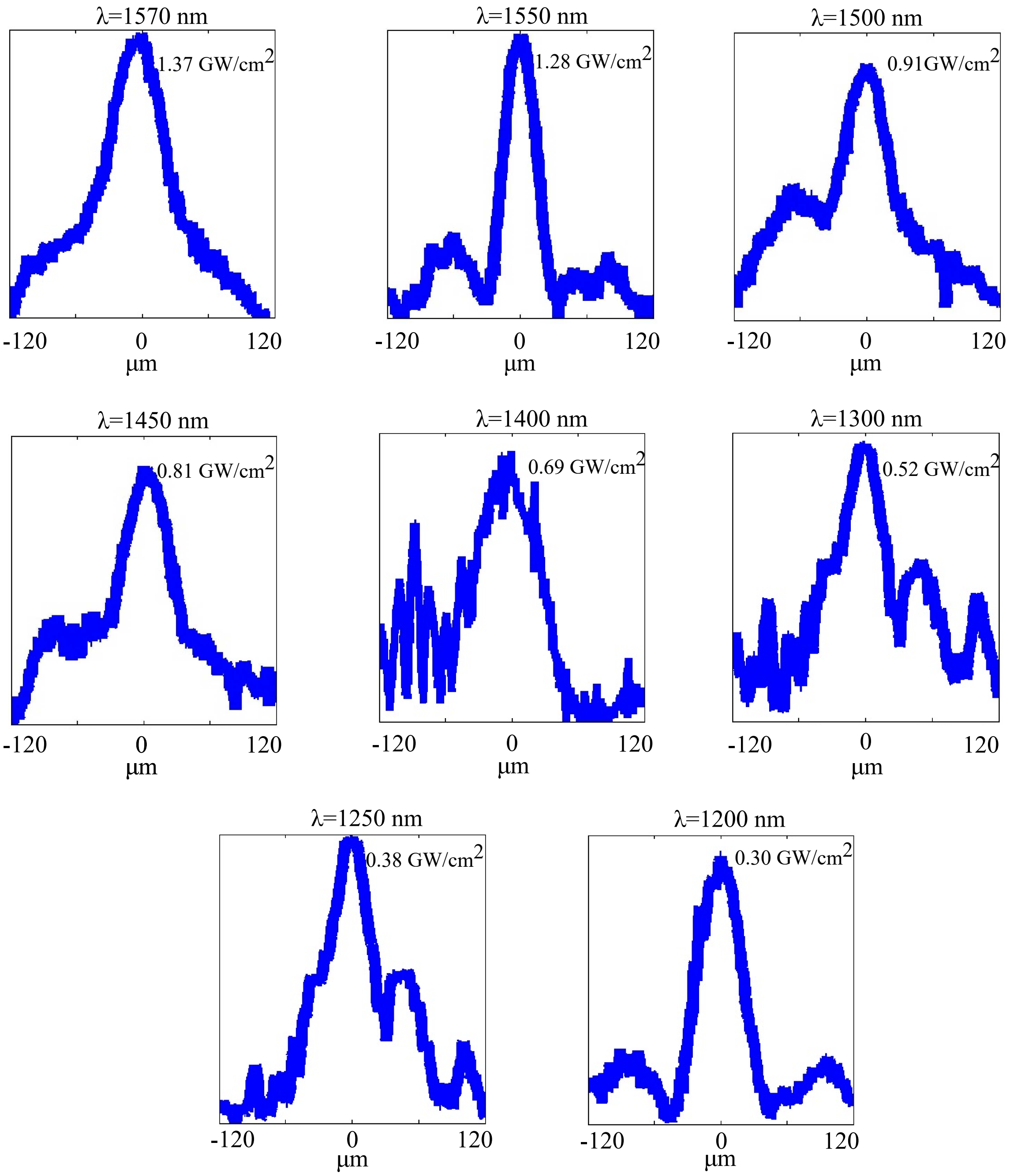

Figure 3.16: Experimental output beam profiles of the best self-focusing behavior obtained as a function of wavelength in the Se2 waveguide.

size of self-trapped beam is formed at 1550 nm and 1200 nm. Besides, a similar width at the exit face and at the entrance face (soliton formation) is observed at 1550 nm. For all studied wavelengths, self-trapped beam is accompanied with local maximum on each side. This is more dominant at shorter wavelengths. The strong Kerr coefficient in chalcogenide gives focusing in our experiment, but the contribution of absorption (TPA) opposes the focusing and brings out wings on both sides of the beam. Also, we note that, the energy required for self-focusing is lower at shorter wavelength than at longer wavelength. For longer wavelengths the focusing is given by weak nonlinear coefficients and three photon absorption [128]. Self-trapped beam quality (soliton like behaviour) couldn't improve by increasing the input power. If we increase the power above the self-focusing threshold, the wings become more intense and lead to beam splitting. The clean self-trapped beam observed at 1550 nm and 1200 nm could be easier compared to simulations and to extract the Kerr coefficient. The n_2 values extracted for 1550 nm and 1200 nm are listed in Table. 3.3. The high optical nonlinearity measured at shorter wavelength is interesting for photonic applications.

3.3/ PHOTOSENSITIVITY OF SAMPLES

In addition to the instantaneous nonlinear Kerr response presented before, we have observed a slow and irreversible self trapping of the optical beam when the illumination is maintained for a long time. We call this effect a photoinduced self-action. This refractive index variation under illumination has been studied for several decades and have been applied to the fabrication of devices such as gratings and waveguides notably in chalcogenide glasses [128]. As mentioned in the previous chapter, photoinduced effects can come from different mechanism and induce changes in the optical constants such as the refractive index, the absorption coefficients and the optical band gap. These effects are stronger when illumination is performed at a wavelength near the optical band gap of the material. Moreover, the photoinduced modification of refractive index takes place slower at lower laser power. In this section, we discuss the photoinduced beam self-trapping and photosensitivity studies in both Se2 and Se4 compositions.

3.3.1/ EXPERIMENTAL DEMONSTRATION OF PHOTOINDUCED SELF-TRAPPING IN CHALCOGENIDE WAVEGUIDES

In order to study this effect, the same experimental setup (Fig. 3.9) as for the beam self-action is used. The measurements were carried out at 1.55 μm in femtosecond regime for an illumination time of about an hour. Evolution of the beam distribution at the output of the Se2 waveguide as a function of time is shown in Fig. 3.17, for an input intensity of 1.2 GW/cm^2. At the beginning of light exposure, the input beam of 32 μm (FWHM) diffracts to 80 μm through the 1.2 cm long waveguide (Fig. 3.18(a)). Then the beam tends to reshape gradually to form weak peaks on each side of the central beam that tends to enlarges as seen in Fig. 3.18(b) and (c). As time progress, multiple peaks formation is observed (Fig. 3.18(d), (e), (f)). At t = 1380 s, the lateral peaks are as intense as the central peak, as

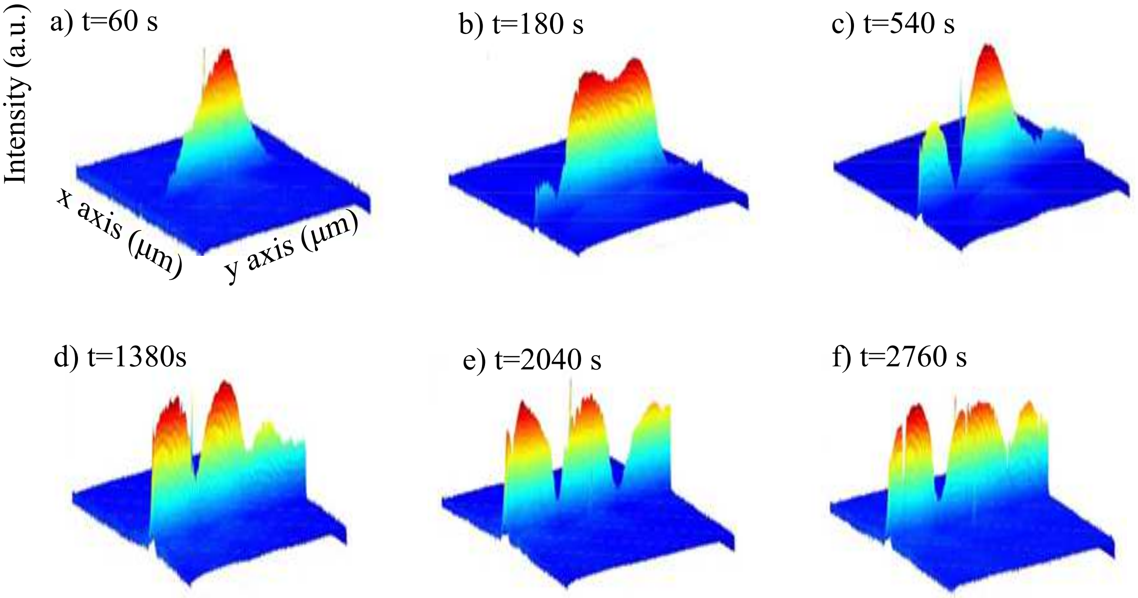

Figure 3.17: Evolution of beam with time for intensities of about 1.2 GW/cm^2 in Se2. (a) Profile of 84 μm wide output beam at t=60 s, (b-f) temporal evolution leads to multiple peak formation.

observed at t = 2040 s (Fig. 3.18(e)). At the end of photoinduced process the beam start to splits asymmetrically due to the strong photoinduced absorption. Photoinduced absorption and scattering are known to be present in chalcogenide on exposure to high power irradiation, when the photon energy is less than the band gap [128]. Hence, photoinduced losses (absorption) are present in this composition with an irradiation of lower energy photon (0.8 eV) than the material bandgap (2.11 eV). Waveguide Se2 is thus photosensitive at 1.55 μm under high illumination intensity. It gives rise to a strong beam dislocation.

Similar experiments are done in Se4 that has bandgap energy of 1.86 eV. Experimental results on the evolution of output beam size with time are shown in Fig. 3.18 for an illumination intensity of 0.81 GW/cm^2. At first, the 32 μm input beam width experience linear diffraction to 90 μm (t = 0 s). Then the beam starts to focus gradually as a function of time. At the end of photoinduced process, the output beam is clearly focused (32 μm, at t = 2640 s) and has a width similar than the input beam. The self-trapped beam maintain its shape for about 14 minutes. Since the process continues to evolve the beam width becomes smaller than the input beam. In other terms, diffraction is balanced by the photoinduced index change. Similarity of the input and output beam (at t = 2640 s) profiles is an indication of soliton formation by the photo- induced effect. These effects thus give an increase of the index of refraction in the illuminated area. If we stop the illumination a guiding structure is present. After comparing the results in both compositions, we found

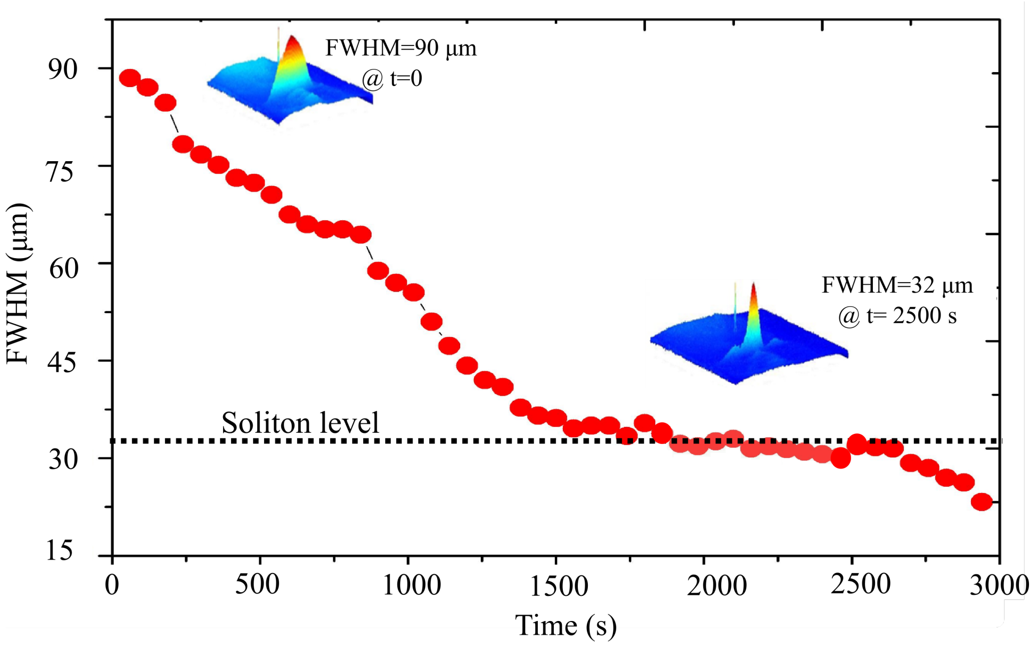

Figure 3.18: Temporal evolution of the optical beam width at the output of the Se4 waveguide for an input intensity of about 0.81 GW/cm^2. Insets show the profile of input beam at $t = 0$ s and $t = 2500$ s.

that studied compositions are photosensitive and the observed effects are irreversible because when the intensity is lowered, the diffraction regime is not recovered like when the Kerr effect is dominant.

3.4/ Summary

In this chapter we have characterized the nonlinear optical properties of the three different selenide waveguides at the wavelength of 1550 nm and 1200 nm. Nonlinear absorption losses of the selenide waveguides are determined by the transmission analysis. A decrease of TPA losses with increase of wavelength is observed. The obtained TPA values are negligible especially at 1550 nm and shows some changes with the increase of Se content. Since the photon energy of excitation wavelength is close to the band gap energy of Se6 films, largest absorption losses are detected. Whereas, minimum absorption losses together with highest damage threshold intensity to light exposure is found in Se2 guiding layer.

We have shown that beam profile analysis due to beam self-trapping is an accurate and simple technique to deduce optical Kerr effect in planar waveguides. This technique has been applied to measure ultrafast optical properties in three slab waveguides named Se6, Se4 and Se2 at the wavelengths of 1550 and 1200 nm. Beam broadening and narrowing results are compared with simulations of the nonlinear Schrödinger equation solved by the (1+1)-D BPM method to deduce the Kerr n_2 coefficients. The found nonlinear refractive index coefficients are consistent with values obtained by different techniques. The highest n_2 coefficient of $32 \pm 5.10^{-18} m^2.W^{-1}$ is found in Se6 films at 1200 nm while the lowest n_2 of (5.5 ± 2) x 10^{-18} m^2/W is obtained in the Se2 films at 1550 nm.

We have also studied the influence of parameters such as wavelength on self-focusing behaviour. Though self-focusing is obtained for a wide range of wavelengths, formation of solitons are limited to the wavelengths of 1550 nm and 1200 nm. In addition, we have reported the experimental observation of an efficient beam self-trapping and soliton-like behavior in Se4 chalcogenide waveguide due to a photo-induced effect. The analysis of nonlinear properties of the Ge-Sb-Se system is showing that the Kerr coefficient as well as TPA coefficient increases with increasing the content of antimony and decreasing the value of band gap energy. The strong ultrafast nonlinearities together with Kerr spatial soliton formation and low propagation losses of the Ge–Sb–Se fabricated planar waveguides make them suitable for nonlinear photonic devices.

After evaluating the optical properties of the fabricated waveguides, the best combination of all parameters for plasmon-soliton coupling such as lowest linear and TPA coefficients, highest damage peak intensity threshold and soliton formation are found in Se2. Thus, Se2 will be the selected composition to deposit plasmonic layer on top of it. The next chapter is dedicated to the experimental study of plasmon-soliton coupling.

4

DEMONSTRATION OF ENHANCED SELF-FOCUSING BY PLASMONS

This chapter provides an insight into the strength of plasmonics for enhancing nonlinear effects. It is divided into two main parts. The theoretical design and fabrication of the chalcogenide plasmonic waveguide is presented in the first part. The second part concentrates on the experimental demonstration of the plasmon-soliton coupling in the designed structure.

PART I

4.1/ THEORETICAL DESIGN AND FABRICATION OF THE PLASMON-SOLITON STRUCTURE

As already mentioned in the introduction, the idea of coupling a SP and a spatial soliton started in the 1980's with the seminal paper by Agranovich *et al.* [13]. However, experimental evidence confirming the existence of these nonlinear waves have not yet been revealed. To observe the plasmon-soliton waves, the designed structure should have specific properties. Firstly, we need a structure that supports solitonic propagation at moderate input intensity. Secondly, the structure should allow the propagation of plasmon with moderate losses. Finally, the structure has to be compatible with fabrication techniques and it is also beneficial to design a structure in which plasmonic field is accessible for measurements using scanning near field microscope (SNOM) tip.

In this part, we focus our attention on the structure design to reach this experimental observation of plasmon-soliton waves. We begin with the section describing the structure of our interest and its theoretical design. Specifically, we present the influence of various parameters such as buffer layer thickness, polarization and wavelength on plasmon-soliton coupling with the help of the model developed by our collaborators from the Fresnel institute in Marseille. Following sections focus on the fabrication and characterization of the chalcogenide plasmonic waveguide.

4.1.1/ STRUCTURE OF INTEREST AND MODELLING APPROACH

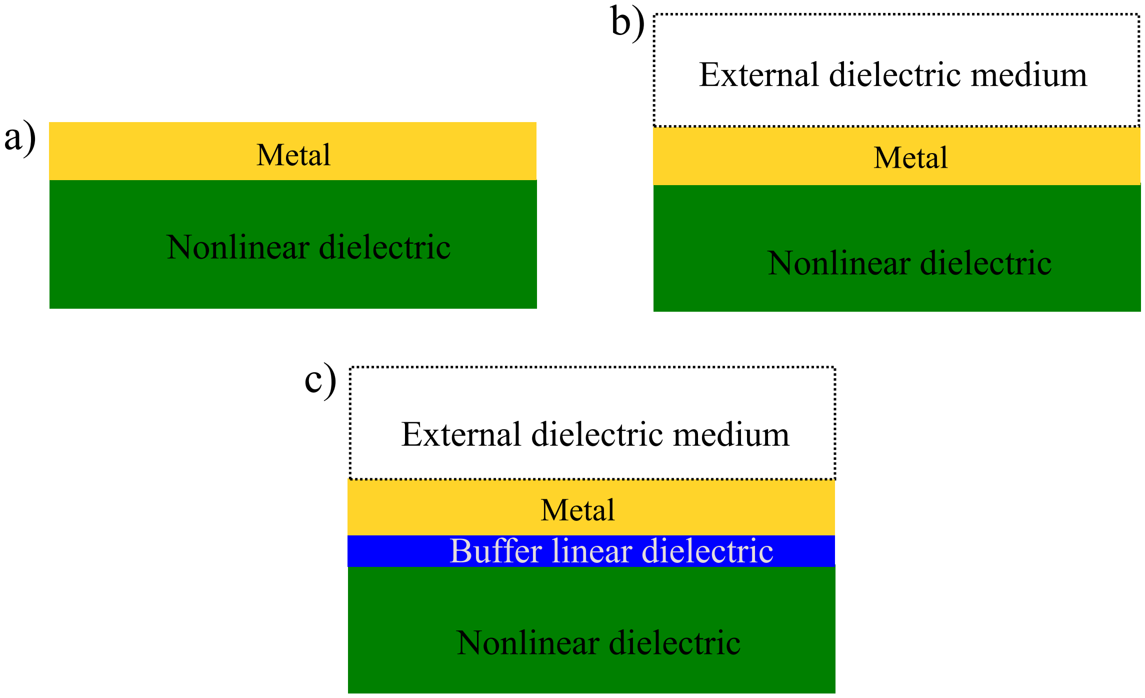

Figure 4.1: Plasmon-soliton waveguide structures: (a) two-layer configuration, (b) three-layer configuration, and (c) four-layer configuration.

The basic waveguide geometry for plasmon-soliton propagation consists of a single interface made of a nonlinear dielectric and a metal as shown in Fig. 4.1(a). Different waveguide configurations are also proposed including the metal-slot [30], the insulator-metal-insulator [102], channel waveguides [107], the dielectric loaded metal and metal wedge [12] to better confine the field and make the light coupling more efficient. Among them the simplest structure in which it is possible to obtain the solutions of plasmon-soliton wave is the three-layer configuration. It is composed of a nonlinear dielectric/metal/external linear dielectric (air) layers (see Fig. 4.1(b)). The study presented in Ref. [29] shows that a three-layer structure supports both plasmonic and solitonic type solutions at low light power. However, these solutions are found only in the case of small refractive index contrast between the nonlinear and the external dielectrics. Importantly, to support low power solitons, a nonlinear medium of high n_2 is required. Moreover, the linear dielectric also has to be a high-index material if the nonlinear dielectric has a high index. Under these circumstance, it is not possible to measure directly the plasmonic part of the solution if the external layer is filled with a solid. Though three-layer configuration can fulfil the main conditions described at the beginning of this section the last one such as plasmon detection by SNOM cannot be fulfilled. To reach this goal, configuration possesses a low refractive index external layer has to be identified.

To overcome the limitations of three layer configuration, a four layer configuration is introduced. As illustrated in Fig. 4.1(c), a thin layer of a linear dielectric (or buffer layer) has been added between the metal and the nonlinear dielectric medium. The detailed study conducted by Walasik *et al.* reports that these structures support low power plasmon-soliton solutions even for high refractive index contrast between the nonlinear and the external dielectrics [28]. In addition, the constraints of material parameters (e.g., buffer layer thickness and metal thickness) are much broader than the three layer case and it can satisfies the three main conditions set for a feasible structure. However, light coupling is not very easy in this structure due to the absence of a guiding layer.

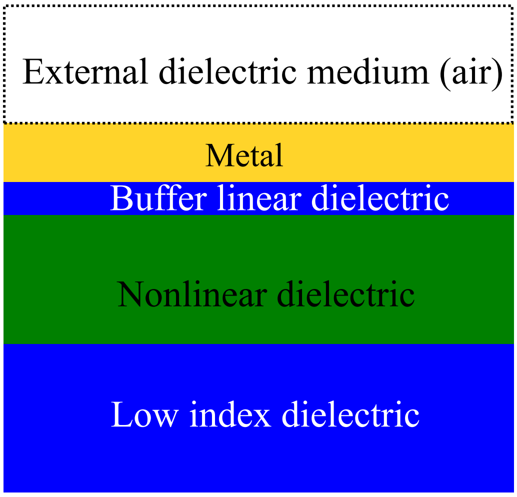

Figure 4.2: Designed 5-layer configuration for plasmon-soliton coupling.

The configuration we propose overcome the limitations of the above mentioned structures. The origin of our structure is a planar chalcogenide waveguide that offers suitable nonlinear properties to form Kerr spatial solitons at near infrared wavelengths as demonstrated in Refs. [205, 161]. For the propagating wave to generate a plasmon polariton a thin metal film must be present at the top surface. However, a compromise has to be found between the improved confinement provided by the plasmon wave, that we want to exploit to efficiently exalt the Kerr effect, and its propagation losses that can be too high and prevent observation of the self-focusing. The chosen solution is to insert a thin low refractive index dielectric layer in between the metal and the nonlinear dielectric layer. Basically our structure consists of a five layer geometry of low index dielectric (SiO_2)/nonlinear dielectric (chalcogenide)/buffer linear dielectric (SiO_2)/metal (Au)/external dielectric (air) (see Fig. 4.2). The designed structure originates from the theoretical study of Walasik *et al.*

[28, 26]. It is expected to allow propagation on a distance long enough to form and maintain a self-focused beam that takes advantage of an enhanced Kerr effect thanks to the electric field plasmon tail that extends deep in the nonlinear dielectric layer. Principally, this particular configuration can be used to excite the plasmon-soliton waves at low input peak intensity. Another advantages are the feasibility to detect the plasmonic part at the interface between the metal and the external dielectric using near-field optics and the suitability for sensor applications.

The influence of various parameters on the formation of hybrid wave is described in the following section.

4.1.2/ DESIGN OF THE PLASMONIC STRUCTURE

As we discussed in chapter 1, the field confinement should be optimized by choosing the waveguide characteristics. Numerical simulations have been performed to determine the optimum thickness for the top layers. It shows that the buffer silica layer thickness is the most critical parameter in the design. Moreover, polarization and wavelength have an influence on plasmon-soliton coupling. In this section we examine the effects of these various parameters on plasmon mode profile.

EFFECTS OF BUFFER LAYER THICKNESS AND POLARIZATION

Let's first examine the influence of buffer layer thickness and polarization. Fig. 4.3 shows the calculated TM and TE mode profiles for SiO_2 layer thickness equal to 30 nm, 15 nm and 5 nm (left column) and zoom in on the field profiles close to the interface area (right column). As depicted in Fig. 4.3(a), if the silica layer thickness is 30 nm, TM and TE transverse profiles of guided beams are very similar. The presence of the metal marginally influences their profiles which are then similar to the fundamental guided modes of the SiO_2/chalcogenide/SiO_2 slab waveguide. For a 15 nm buffer layer, the TM field profile is significantly different from the TE profile (Fig. 4.3(b)). In this case, TM wave is confined in the buffer layer and in the nonlinear layer. A decrease in buffer layer thickness even improve this confinement. For example, when a SiO_2 layer as thin as 5 nm is considered (Fig. 4.3(c)) the TM wave is strongly affected by the metal and its plasmonic nature is clear with a strong localization at the metal/dielectric interface. No such characteristic is observed for TE waves since they do not have electric field component perpendicular to the interface. Note that the intensity in the nonlinear medium is greater for a 5 nm thick buffer layer compare to a 15 nm one. However, absorption is also greater for a 5 nm layer.

We chose to fabricate a structure with a 10 nm thick SiO_2 layer. We considered this particular thickness as a fair compromise between light confinement and moderate propagation losses. In addition, simulations show that plasmonic mode is TM in nature.

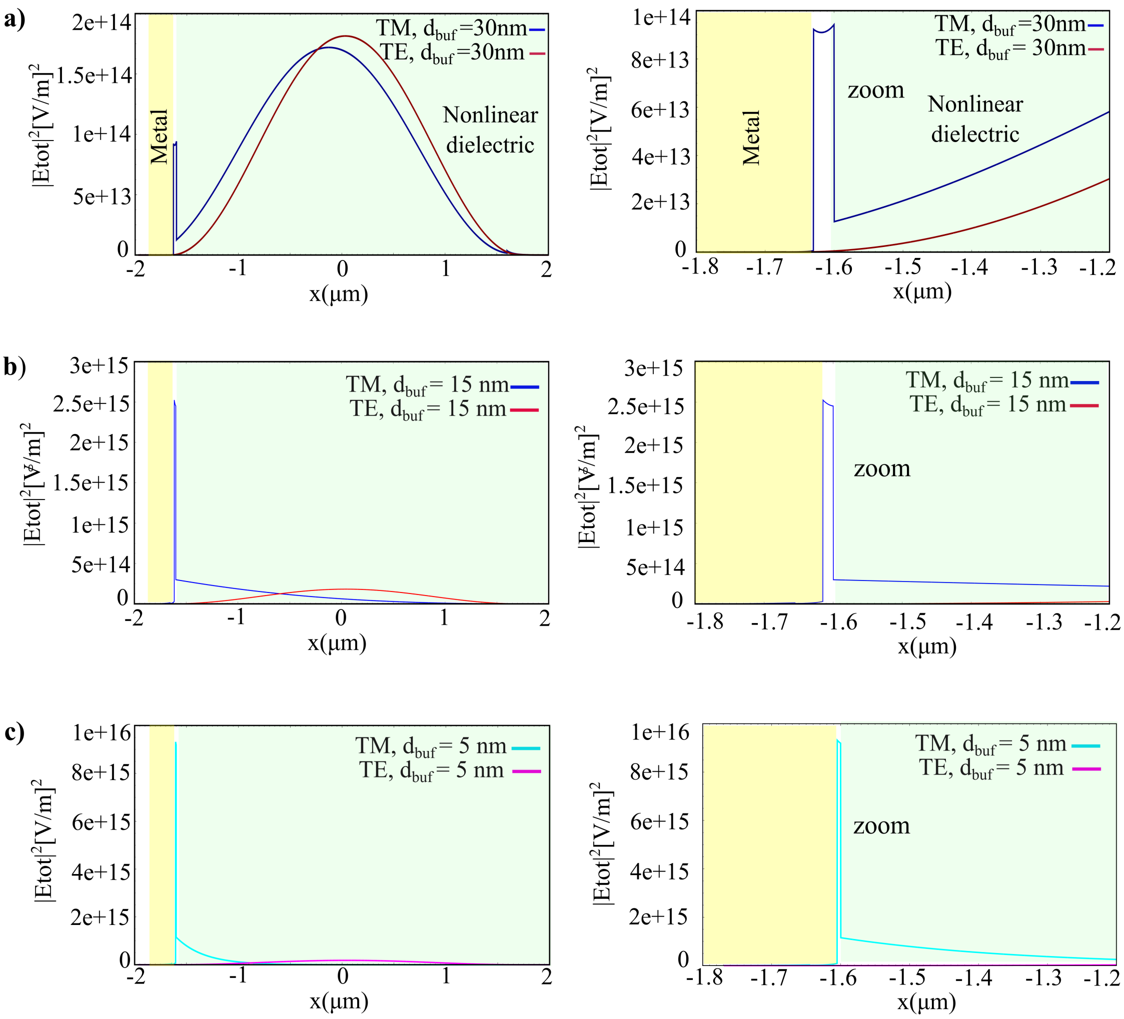

Figure 4.3: Calculated fundamental TM and TE mode profiles for SiO_2 buffer thickness equal to (a) 30 nm, (b) 15 nm and (c) 5 nm respectively.

EFFECTS OF WAVELENGTH

The intensity profile of modes for the wavelength range of 1.6 μm to 1.0 μm in the presence and absence of metallic layer with a buffer layer thickness of 15 nm are shown in Fig. 4.4. As can be seen in Fig. 4.4(a) and (b), light shift toward the metal layer is increased as the wavelength increases. The plasmonic character is less and less evident as the wavelength is shorter (Fig. 4.4(c) and (d)). It is expected because for a given guiding chalcogenide layer thickness light penetrates deeper into the cladding for longer wavelengths. Further, as we move to longer wavelengths, an increase in peak intensity at the interface is noticed with metal. Since we are looking for a solution to excite Kerr solitons, it is better to work at long wavelength. So, with an aim to achieve strong confinement while keeping the propagation losses low, we selected 1550 nm as the excitation wavelength for plasmon-soliton wave which is the longest wavelength achievable with our tunable parametric oscillator.

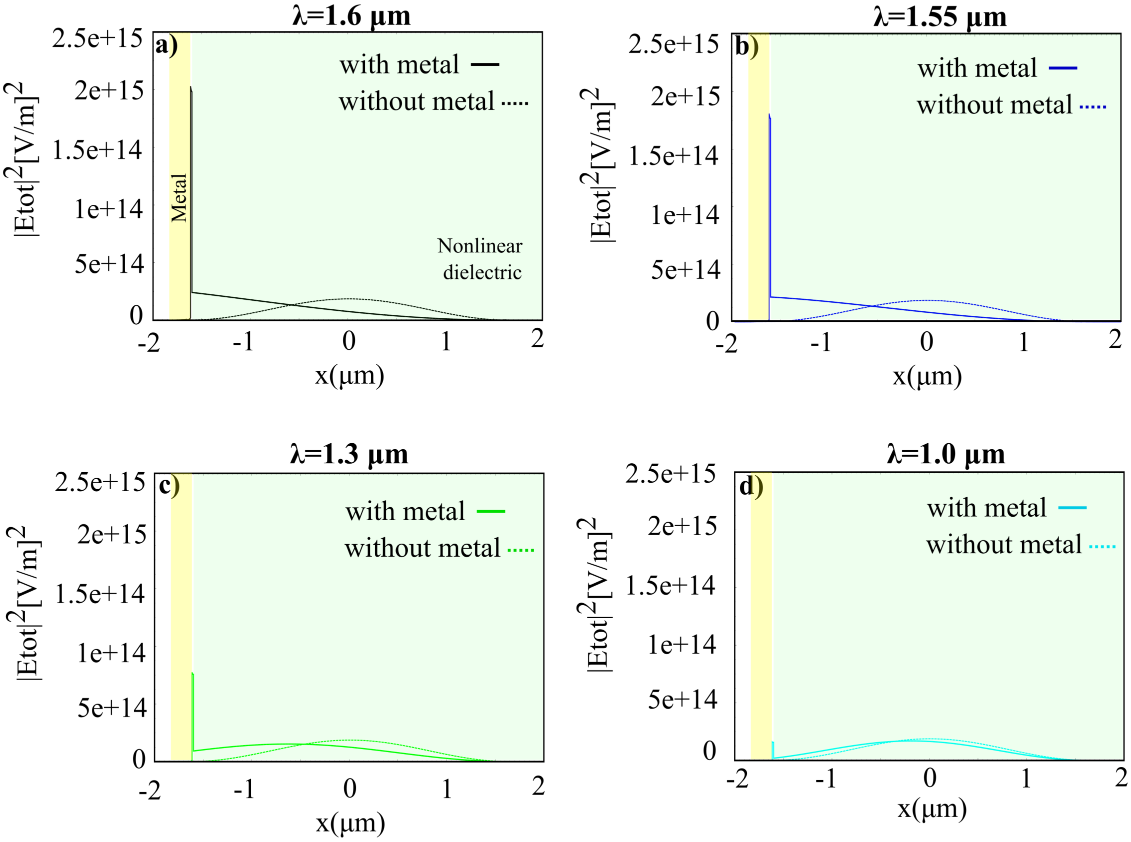

Figure 4.4: Intensity distribution of TM polarized light in the presence and absence of metal for an excitation wavelength of (a) 1.6 μm, (b) 1.55 μm, (c) 1.3 μm and (d) 1.0 μm. Buffer layer thickness is 15 nm.

4.1.3/ FABRICATION AND CHARACTERIZATION OF CHALCOGENIDE PLASMONIC STRUCTURE

In this section we focus our attention on the fabrication of the designed Plasmonic Structure (PS).

As a first step in the fabrication of the structure, the chalcogenide deposition parameters such as Ar pressure and sputtering power were optimized to have a low surface roughness to reduce propagation losses and enabling an efficient deposition of top layers at the surface. Detailed description of the planar structure fabrication steps and its optical characterization have been described in chapter 2 and chapter 3 since it corresponds to the previously characterized waveguide. As we mentioned in the summary of chapter

3, we selected Se2 ($Ge_{28.1}$ $Sb_{6.3}Se_{65.6}$) composition for the nonlinear dielectric medium. This glass compositions have been chosen due to its large Kerr nonlinearity (n_2 = 5.5 x $10^{-18}m^2.W^{-1}$), moderate two-photon absorption coefficient (α_2 = 0.43 cm/GW) at the wavelength of interest of 1.55 μm [205] and high damage threshold intensity evaluated to 2 GW/cm^2. In addition, this film composition present a lower photosensitivity than glasses with higher antimony content.

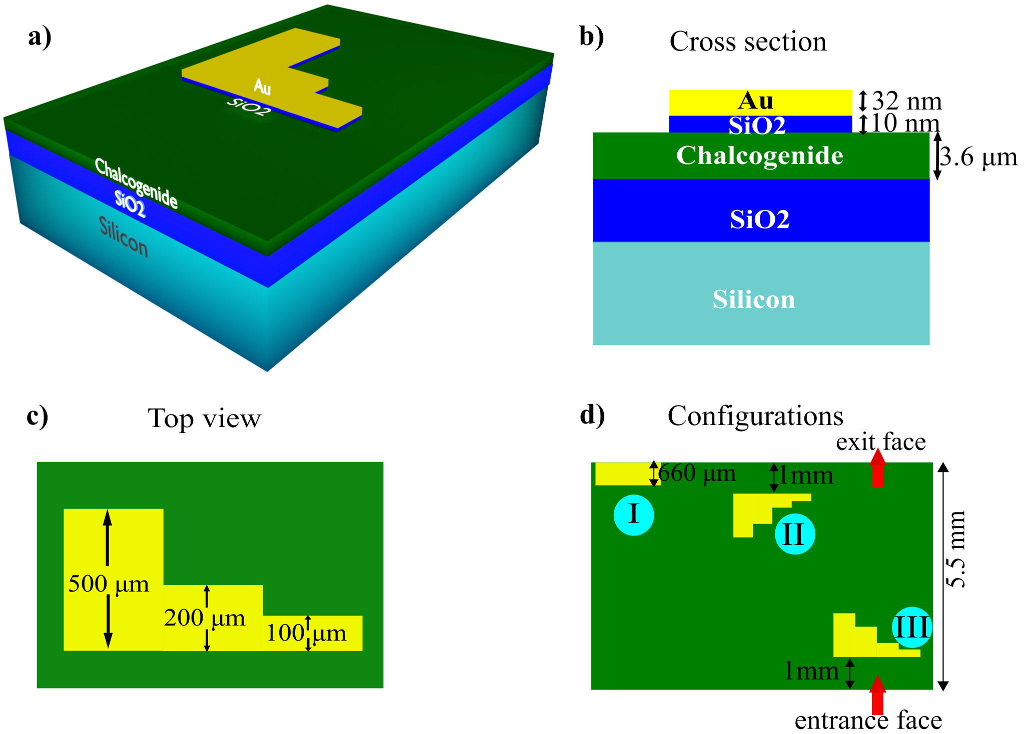

Figure 4.5: (a) 3-D view of the PS. (b) Schematic description of the cross section of the sample with the metal cover. (c) Detailed top view of the staircase metallic pattern. (d) Schematic overall top view of the studied configurations.

The Kerr layer is 3.6 μm thick, it is made of Se2 chalcogenide glass deposited by RF sputtering on an oxidized silicon wafer [162] as shown in Fig. 4.5(a). Top silica buffer layer of 10 nm thickness is deposited by the same RF sputtering technique. Note that deposition of thinner SiO_2 layer of good quality is very challenging with the used deposition technique. The next step is the deposition of a gold layer on top of the SiO_2 buffer layer. For that, a 2.54 cm diameter gold target constituted of a pure gold foil (99% purity, 0.5 mm thick) is selected. Then, a 32 nm thick gold layer was sputtered (DC sputtering) on top of SiO_2, at room temperature under pure Ar atmosphere with a pressure of 5.10^{-3} mbar which gives the hybrid stack described in Fig. 4.5(b). Note that we didn't deposit the SiO_2 buffer and the gold layer on the whole surface of the chalcogenide film, we limited it to a small area. The coated area can be called as with PS and the uncoated area can be called as without PS. In this way one can study the propagation of spatial soliton and the coupled plasmon-soliton waves separately by choosing the light coupling zone. A good adherence of gold on the surface of SiO_2 layer was obtained.

The metal layer was then patterned to form a staircase shape as described in Fig. 4.5(a) and Fig. 4.5(c). This shape provides a way to analyze the influence of the metal length on the propagating wave by choosing the position of the launched beam. Metallized length can be chosen between 0 to 660 μm as shown in Fig. 4.5(c) and Fig. 4.5(d).

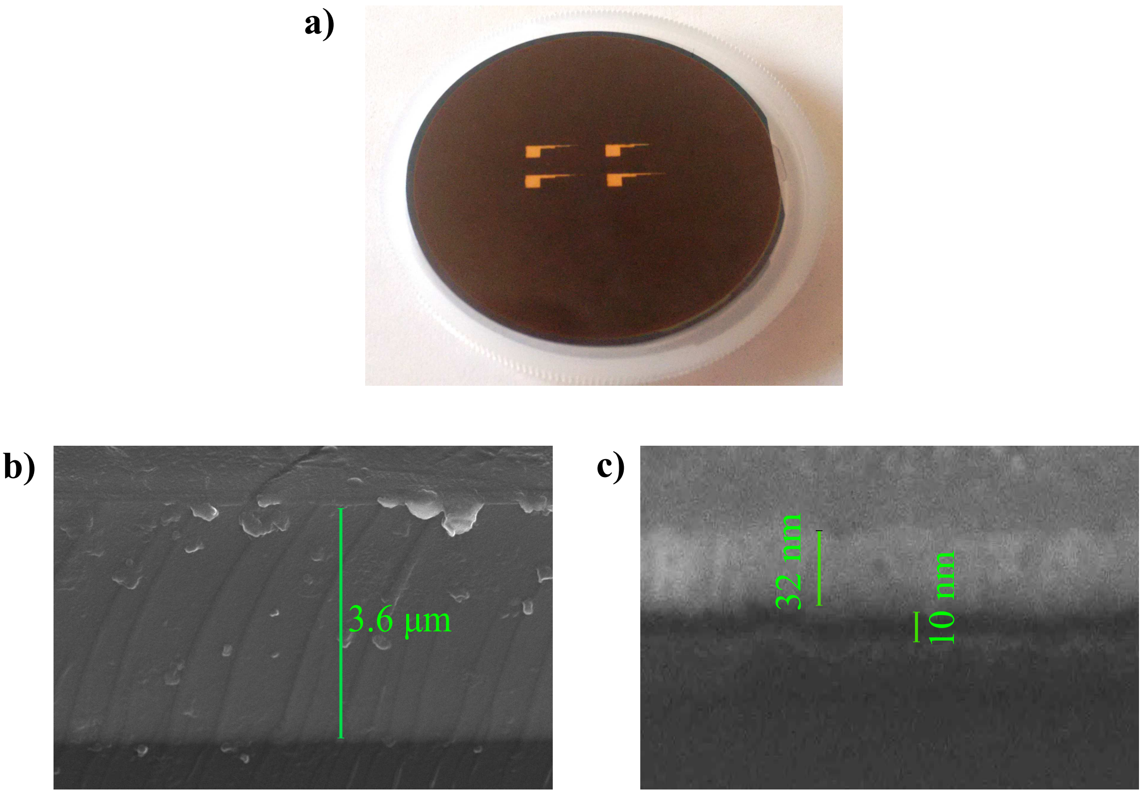

Figure 4.6: (a) Photograph of the chalcogenide plasmonic wafer (Se2+Au) used in our study. (b) SEM image of the chalcogenide layer. (c) SEM image of the Au/SiO_2/chalcogenide interfaces.

The photograph of the fabricated nonlinear plasmonic wafer is shown in Fig. 4.6(a). Finally, two samples 5.5 mm long and one sample 5.1 mm long along the propagation direction are obtained by cleaving the processed wafer. Each sample possesses different plasmonic patterns located at different positions that thus constitutes three different configurations as described in Fig. 4.5(d). The first considered configuration (Fig. 4.5(d), top left) is a rectangular plasmonic pattern of 660 μm long located near the exit face of the sample (configuration I). The two other configurations correspond to staircase metallic patterns present either 1 mm before the exit face (Fig. 4.5(d), top center), or 1 mm after the entrance face of the sample (Fig. 4.5(d), bottom right) which are called configurations II and III, respectively.

Furthermore, the thickness of the chalcogenide, buffer SiO_2 and Au layer are analysed by SEM (Fig. 4.6(b), (c)). Characterization shows that chalcogenide layer is 3.6 μm, SiO_2 layer is 10 nm thick and gold layer is 32 nm thick which proves that the targeted and fabricated layer thicknesses are in accordance.

4.1.4/ DISCUSSION

In the previous part, a feasible structure was designed and fabricated to allow the experimental characterizations. We have investigated the effects of the SiO_2 buffer layer thickness, polarization and wavelength on the characteristics of the mode. The proposed configuration combines a pure dielectric and localized plasmonic structures via a thin buffer layer. It can provide a strong confinement while retaining a long propagation length. Samples have been fabricated by the sputtering technique.

PART II

4.2/ EXPERIMENTAL DEMONSTRATION OF PLASMON-SOLITON COUPLING

The main goal of this PhD thesis is the experimental demonstration of an enhanced self-focusing with the help of a plasmonic structure . The results are presented in the following development. We start with the presentation of the experimental setup used for plasmon-soliton coupling. The following sections focus on the various experimental results that unambiguously reveal the coupling between plasmon and soliton. We also present photoinduced effect observed in the fabricated chalcogenide plasmonic waveguide.

4.2.1/ EXPERIMENTAL SETUP

The same experimental setup as for the beam self-trapping analysis (Fig. 3.9) is used for the characterization of plasmonic structure. 3-D artistic view of the experimental setup is replicated in Fig. 4.7. Further to the setup descriptions given in section 3.2.3 of chapter 3, a polariser and half wave plate are also used to adjust the polarization state of the injected beam.

The experiments consist in injecting a 4 x 31 μm^2 (FWHM along X and Y-axis, respectively) elliptical beam either with a TM or a TE polarization in to the chalcogenide layer in which the spot size along y-axis is focused 2 mm inside the sample. Such a way of beam focusing inside the sample helps to prevent the input facet damage at high intensity since the intensity at the entrance face is lower than the intensity inside the waveguide.

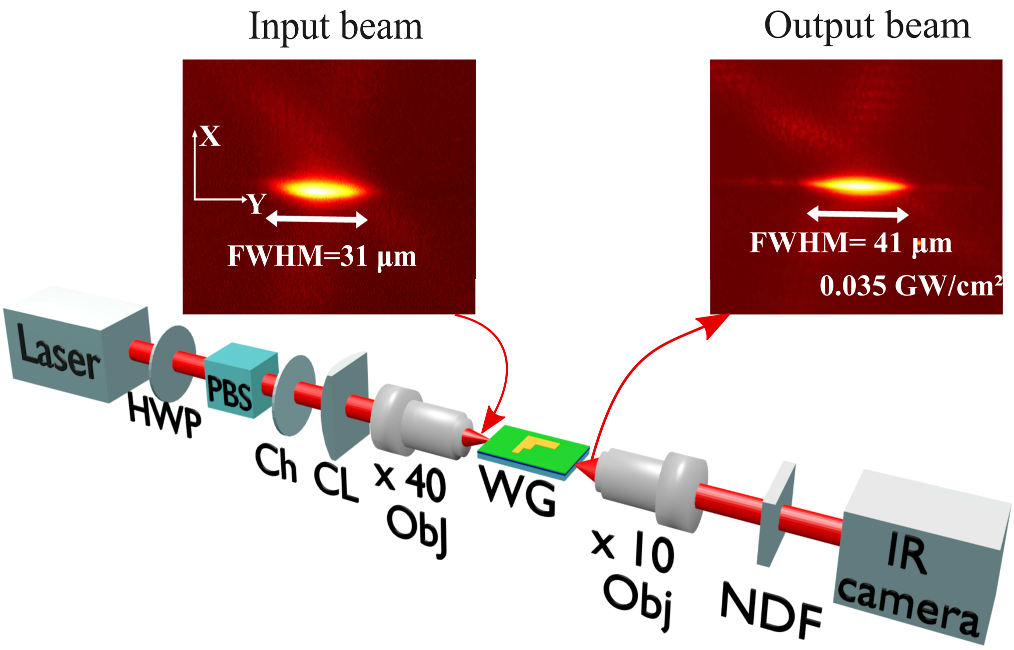

Figure 4.7: Experimental setup used for the observation of plasmon-soliton coupling and images of the injected beam and output beam in linear regime. HWP, half wave plate; PBS, polarizing beam splitter; Ch, chopper; CL, cylindrical lens; Obj, microscope objective; NDF, neutral density filters.

Moreover, it results a weakly diffracting beam over the 5.5 mm long propagation distance. This spot size is also carefully end-fire coupled into the waveguide in order to excite the fundamental guided mode. No higher order modes are observed at the output of the waveguide thanks to a weak overlap with the injected beam. Input and output powers are monitored to deduce the coupling efficiency and the waveguide transmission. The output beam spatial profile evolution versus light power is then monitored with a vidicon infrared camera using a x10 microscope objective. After 5.5 mm propagation inside the waveguide, the diffracted beam reaches a 41 μm FWHM along Y-axis (Fig. 4.7) in linear regime. In this regime a ≈21% waveguide transmission is measured for both TM and TE polarizations when light propagates outside the metallized area. This transmitted power is consistent with a coupling efficiency of 28% and propagation losses of about 0.19 cm^{-1}. The incident intensity is latter determined by dividing the coupled light peak power by the section of the guided mode.

4.2.2/ CONCEPT OF PLASMON-SOLITON COUPLING

As we discussed in chapter 1, plasmons can be excited via evanescent waves generated at the total internal reflection or using appropriate periodic structures producing evanescent waves [23]. In contrast to this usual way of plasmon excitation, we used the plasmon waveguide to inject light below the metallic structure and excite the plasmon.

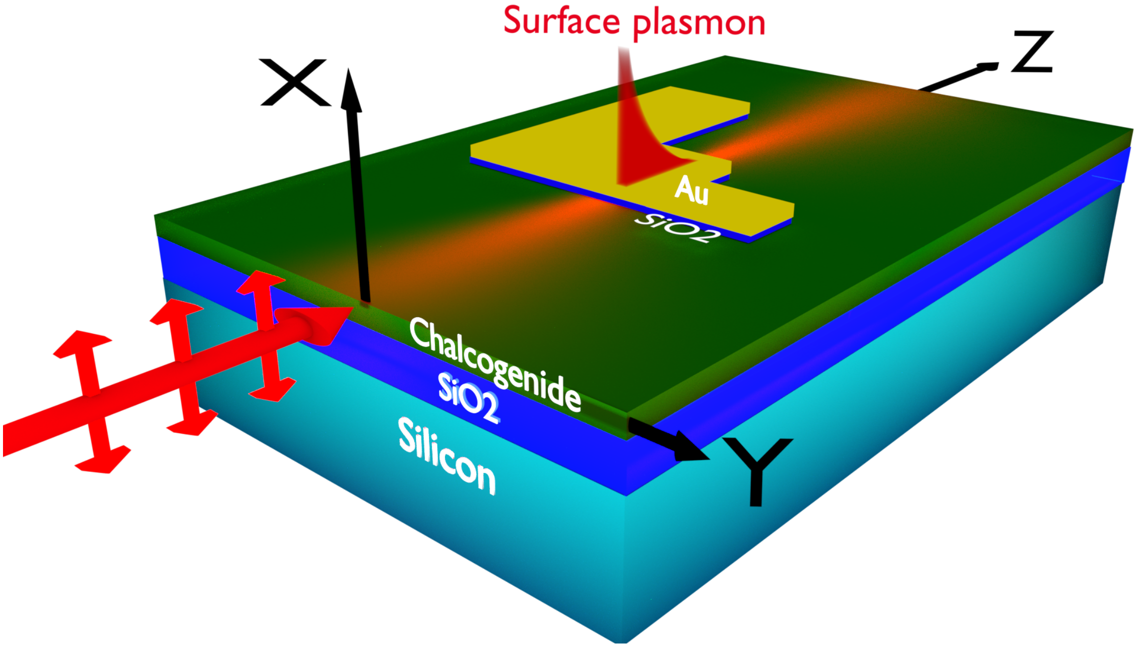

Figure 4.8: 3-D artistic view of plasmon-soliton coupling in a nonlinear plasmonic waveguide.

The basic principle of the excitation mechanism is illustrated in Fig. 4.8. It consists in injecting light into the nonlinear dielectric layer without metal and the plasmon wave will form only when this guided wave enters in area where a PS is present. In nonlinear regime, we can utilize the property of diffraction compensation by nonlinear effects in the Kerr medium i.e., formation of Kerr spatial soliton to excite the plasmon mode and could even generate the non-diffracting plasmon-soliton waves. As illustrated in Fig. 4.8, light propagating through the chalcogenide layer is coupled with the plasmon when reaching the PS and results in a stronger localization of light. As a result, an enhancement in intensity is expected under the PS. The strong intensity provided by the plasmon can thus provide a stronger Kerr nonlinearity and reduce the power requirement to induce a self-trapping effect.

Experimental demonstration of the spatially self-trapped plasmonic wave is presented in the following section.

4.2.3/ FIRST EXPERIMENTAL EVIDENCE OF PLASMON ENHANCED SELF-FOCUSING

In order to disclose the coupling between the SPP and the optical Kerr nonlinearity, we first characterize the self-trapping behavior in the absence of metallic layer. These preliminary experiments can thus be considered as a benchmark. As shown in references

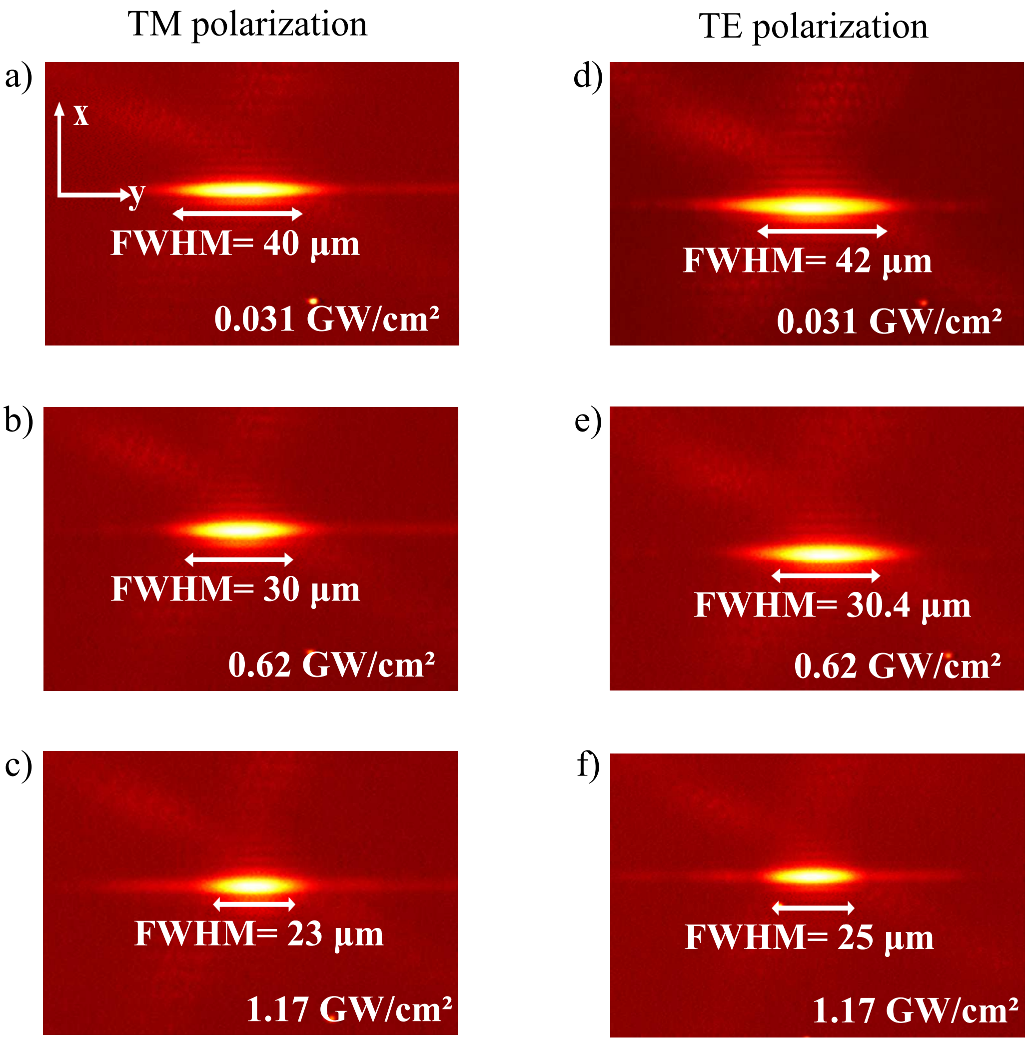

Figure 4.9: Experimental images taken at the output of the 5.1 mm long sample showing both soliton formation and self-focusing behavior in the absence of PS.

[205, 161] and in chapter 3 the optical Kerr nonlinearity in such chalcogenide slab waveguides can support spatial solitons at near-infrared wavelengths. In the tested sample, input beam undergoes free diffraction in a 5.1 mm long sample at low incident intensity of 0.031 GW/cm^2 and give a beam size of about 41 μm (Fig. 4.9(a), (d)) regardless of the state of polarization. As we increase the incident intensity, a beam narrowing effect is observed. With an input intensity of 0.62 GW/cm^2, we observe that the beam diffraction is compensated by the self-focusing effect as shown by the output width (Fig. 4.9(b), (e)) similar to the injected one (Fig. 4.7). If the input intensity is further raised a stronger focusing effect occurs. For an intensity of 1.17 GW/cm^2 a 23 μm FWHM is obtained at the output (Fig. 4.9(c), (f)). Note that the very same behavior is observed for both TM and TE polarizations for this configuration without PS.

The sample is then shifted laterally so that the PS is on the trajectory of the launched beam. To be more specific, configuration I (PS is at the exit facet) is first considered

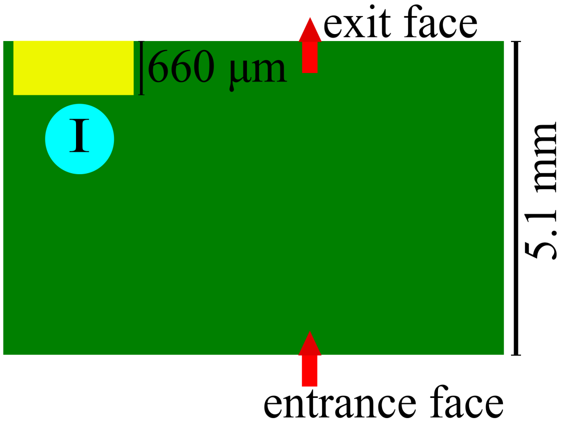

Figure 4.10: Schematic illustration of top view of configuration I with a PS length of 660 μm positioned at the exit face.

with a PS length of 660 μm (see Fig. 4.10). To analyse the polarization dependence and to understand the influence of the incident intensity, experiments are performed for both polarizations by varying the input intensity.

In linear regime the presence of this metallic structure located near the end of the waveguide does not modify the observed output beam distribution (Fig. 4.11(a), (d)). The linear transmission is however reduced due to additional propagation losses. Compared to the situation without the PS, additional attenuation (power loss under the PS) of 0.572 cm $^{-1}$ and 28 ± 1 cm^{-1} are deduced for TE and TM polarized light, respectively. The strong absorption loss for TM wave is expected due to plasmon. As the intensity is raised, a strong enhancement of the self-focusing behavior is observed at the output of the waveguide for a TM polarization. For instance, for an input intensity of 0.62 GW/cm^2 (Fig. 4.11(b) the output beam is already narrower (19 μm FWHM) than the injected one (31 μm FWHM) while an input intensity of 1.17 GW/cm^2 leads to a very efficient trapping of the beam as witnessed by the output beam of 12 μm FWHM (Fig. 4.11(c). This enhanced focusing is also evident in Fig. 4.11(A).

To show the difference in self-focusing effect in the presence and absence of the PS, the results for the case without PS is reproduced in column 3 of Fig. 4.11(g-i). By comparing the result shown in Fig. 4.11(c) with the one obtained at the same intensity without PS (Fig. 4.11(i)), we can deduce that the plasmonic enhanced nonlinear effect focuses the beam from 23 μm to 12 μm FWHM over the 660 μm long structure. It is important to note that this exalted focusing is not observed for the TE polarization. Indeed, as shown in Fig. 4.11(e), (f) and (B), the TE mode shows no improved self-focusing compared to the configuration without the PS (Fig. 4.11(g-i) and (C)). This polarization dependent behavior is a characteristic marker of the plasmonic effect.

Otherwise, the possible influence of a thermally induced self-focusing has to be consid-

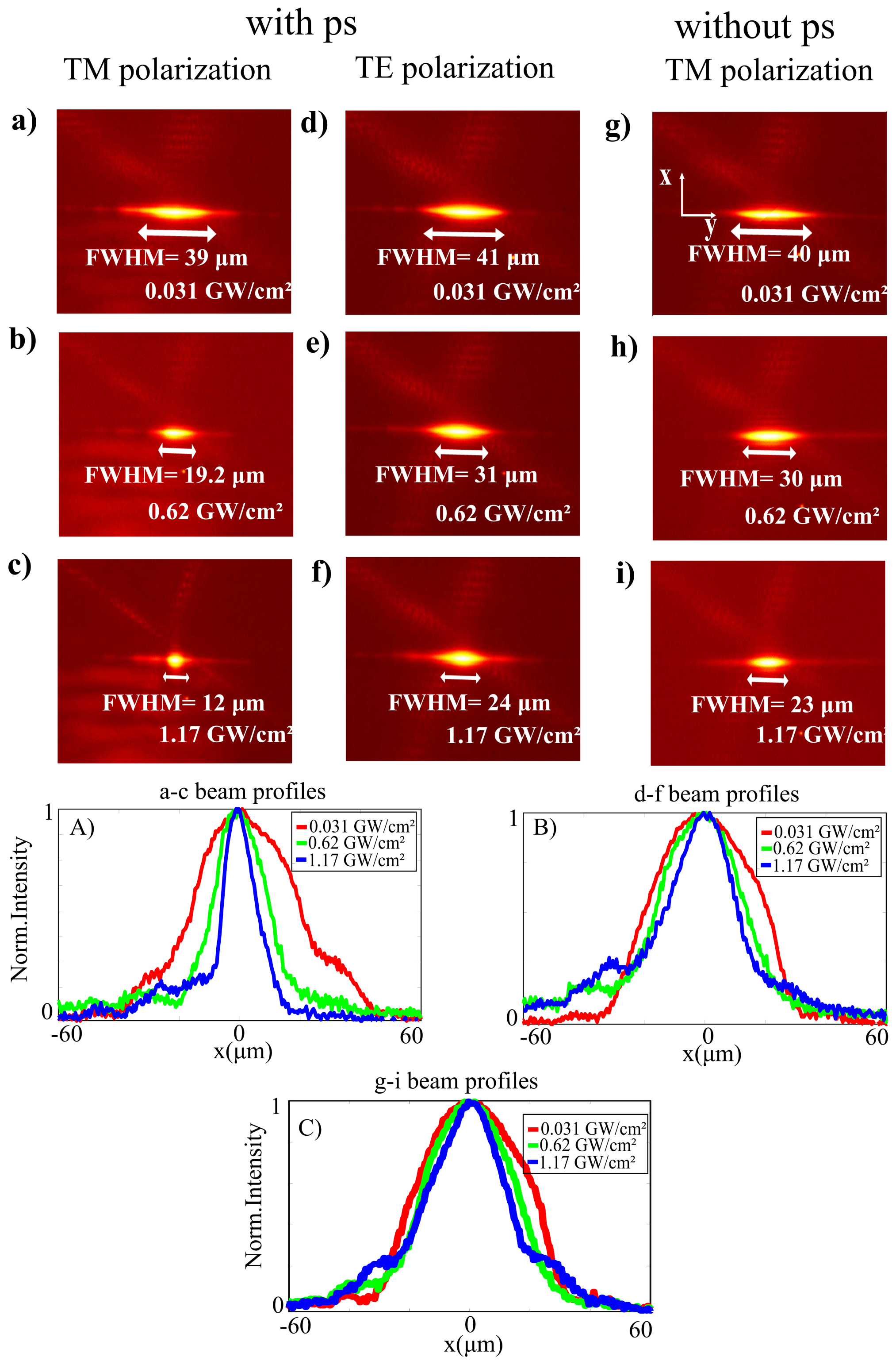

Figure 4.11: Comparison of self-focusing behavior of light as a function of input intensity in the hybrid plasmon-soliton waveguide under TM polarization (a-c), for TE polarization (d-f) and without PS (g-i). Output beam profiles corresponding to Figs; a-c (A), d-f (B) and g-i (C).

ered since absorption is higher when a plasmon is generated. To this end, the experiment is repeated by inserting a mechanical chopper that diminishes the average power to 40% while keeping the same peak power. As in the experimental results shown in section 3.2.4 of chapter 3, no measurable change of the self-trapping was observed which excludes any significant role of the temperature.

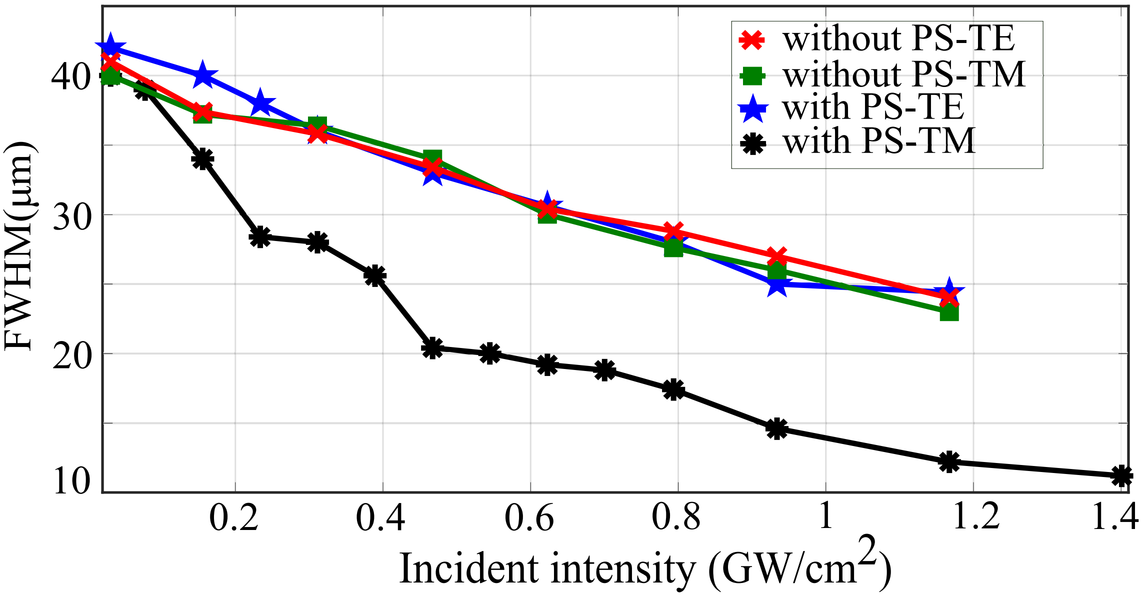

Figure 4.12: Measured output beam FWHM as a function of input peak intensity for both TM and TE polarization. Metallic layer is 660 μm long and it is positioned exactly at the exit face of the sample(configuration I).

The striking self-focusing enhancement due to the plasmonic effect is also evident in the graph from Fig. 4.12 where the output FWHM beam is plotted as a function of the beam intensity for TE and TM polarizations both with and without the PS. For the three arrangements for which plasmon generation is not achievable, i.e., without PS-TM and TE, and with PS-TE polarization, a similar behavior is observed. It is characterized by a gradual focusing with a linear evolution of the beam width versus intensity. As discussed earlier, similar FWHM of 31 μm at the input and output, indication of a regime very close to the spatial soliton, is reached at an intensity of about 0.62 GW/cm^2. The behaviour for a TM polarized mode in presence of a PS differs significantly with a rapid focusing as the intensity is raised. About three times less intensity (0.21 GW/cm^2) is needed to reach a 31 μm output beam compare to the case without plasmon. In addition, the width evolves with a nonlinear trend and tends to saturate when beam size approaches a 12 μm FWHM. This hybrid plasmonic geometry is thus definitely providing an enhanced self-focusing nonlinearity for TM polarization.

Further to these experimental results, BPM simulations are performed to identify the intensity enhancement expected by the plasmons which is depicted in Fig. 4.13. To be

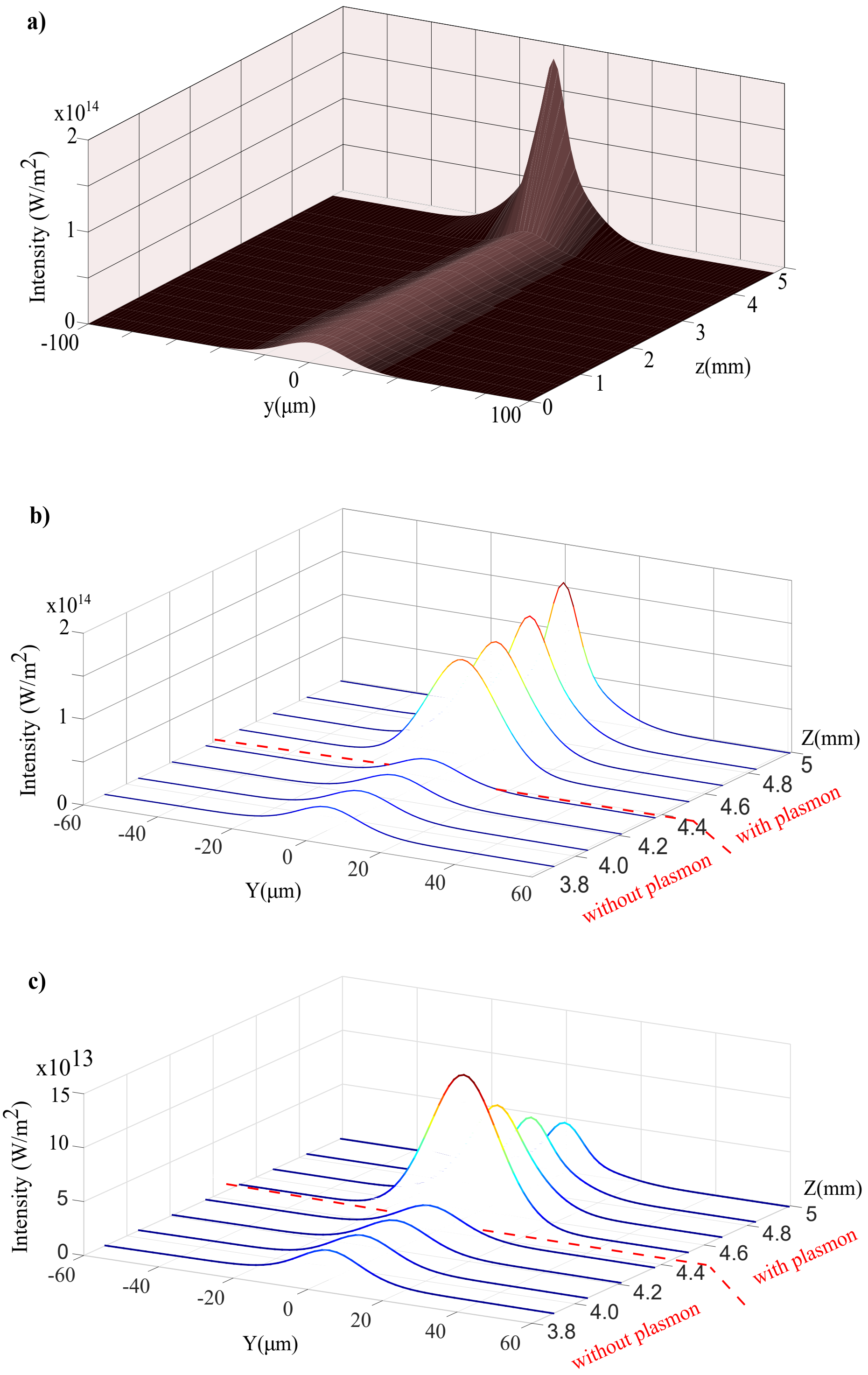

Figure 4.13: (a) Numerical simulation showing the predicted evolution of the pulsed beam in a 5.1 mm long nonlinear plasmonic waveguide. (b) Zoom in on the beam profile for distance from 3.8 to 5.1 mm in the absence of metallic absorption, (c) in the presence of metallic absorption. Material parameters: λ = 1550 nm, n_2 = 5.5 x 10^{-18} $m^2.W^{-1}$, α_1 of waveguide = 0.19 cm^{-1}, α_1 of PS= 28 cm^{-1}, α_2 = 0.43 cm/GW, input beam FWHM = 31 μm, input intensity = 1.17 GW/cm^2.

more specific, BPM is done for a (1+1)-D case to model the behavior of the pulse optical beam in the Nonlinear Plasmonic Waveguide (NPW). Material parameters for the simulations are taken from our previous studies (chapter 2, 3) on the nonlinear characterization of chalcogenide waveguides by the beam self-trapping technique. Firstly, we consider the propagation of light through the NPW by neglecting the absorption due to the PS (Fig. 4.13(a), (b)). As in the experiment an input intensity of 1.17 GW/cm^2 and a propagation length of 5.1 mm (length without PS (4.4 mm) + length with PS (660 μm) = 5.1 mm) are considered in the BPM simulation. In this case, the input beam of 31 μm undergoes beam narrowing and reaches a spot size of 23 μm after a propagation length of 4.4 mm. When entering the PS we have to increase the intensity 5 fold than before the PS to observe the tight focusing to 12 μm as in the experiment. In other words, if we want to achieve a similar giant focused beam of 12 μm due to the Kerr effect, it requires an intensity of 5.8 GW/cm^2 at the entrance of the PS. Note that such a high power would not be possible to butt coupled in the sample since it is much higher than the damage threshold of 2 GW/cm^2.

We repeated similar simulations by considering the metallic losses. The BPM result is depicted in Fig. 4.13(c). We observed that the imposed intensity has now to be close to 8.5 times higher at the entrance of the PS compare to before the PS to retrieve the strong trapping and compensate the large losses associated with the metal. At this point the expected intensity under the metallic structure is 11 GW/cm^2. Moreover, a decrease in the beam amplitude along the propagation distance of PS is noticed due to the large plasmonic losses.

We show that a clear improvement of the self-focusing is present in the fabricated NPW, when a TM polarized light propagates through the structure. We attribute this enhancement to the plasmonic effect. As a consequence a strong focusing effect occurs even at low input intensity. Theoretical predictions of enhanced nonlinearity through plasmonic effect is thus confirmed experimentally for the first time. Note that a potential Kerr effect due to the metal could be suspected to play a role in the enhancement. In the following part we will further characterize the discovered effect.

4.2.4/ CHARACTERIZATION OF THE PLASMON ENHANCED FOCUSING

To get a better understanding of the disclosed plasmon-soliton coupling for TM waves and further confirms the propagation and behavior of light in the proposed structure, different configurations are then tested.

We first studied the influence of the position of the PS along propagation as shown in Fig. 4.14. Three different cases are considered. The previously considered one (configuration

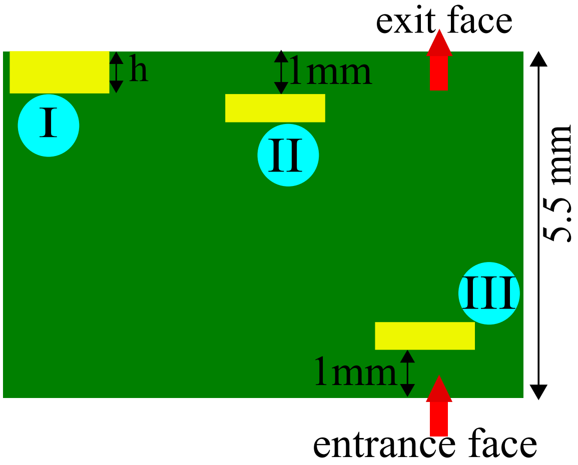

Figure 4.14: Schematic illustration of the considered configurations. PS length (h) of configuration I is 660 μm, Configuration II and III are for h= 500 μm respectively.

I) with a 660 μm long PS (Fig. 4.14, top left). The second (configuration II) is a 500 μm long PS positioned 1 mm before the exit face (Fig. 4.14, top center). The last one (configuration III) is made of a 500 μm long PS located 1 mm after the entrance face (Fig. 4.14, bottom right). Experimental results of the observed beam width as a function of incident intensity in the three configurations are summarized in Fig. 4.15. At low intensity the beam undergoes the very same free diffraction in the 5.5 mm long sample regardless of the electrode location which precludes any linear beam distortion from the PS. As soon as the intensity is raised the output beam clearly focuses which is mainly attributed to the Kerr-lens effect in the PS. However, a beam spreading is observed when the intensity is increased above an intensity threshold that depends on the considered configuration. The threshold is about 0.87 GW/cm^2 and 0.35 GW/cm^2 for a PS positioned 1 mm before the exit face (configuration II) or 1 mm after the entrance face (configuration III), respectively. This behavior can once again be explained by the strong localized self-focusing induced by the PS. Indeed, when such a focusing leads to a narrow spot the beam diffraction cannot be compensated by the weaker nonlinearity present after the PS and the beam diffraction is dominant. Consequently, beam spreading is observed at the output face.

For instance, if we consider a 11 μm (FWHM) spot size formed after the PS, linear diffraction predicts that an 83 μm wide beam is formed after a 4 mm long propagation. This calculation is in accordance with the beam size (84 μm) observed at high intensity in configuration III from Fig. 4.15. The diffraction is weaker in configuration II since the PS is only 1 mm from the output observation face. Note that, as observed experimentally, the input threshold intensity is expected to be weaker when the PS is close to the entrance face. Indeed, due to the linear and two photon absorptions, the intensity reaching the PS is not reduced as much as in configuration II where the PS is far from the input face. It is also important to note that diffraction is not present in configuration I but a

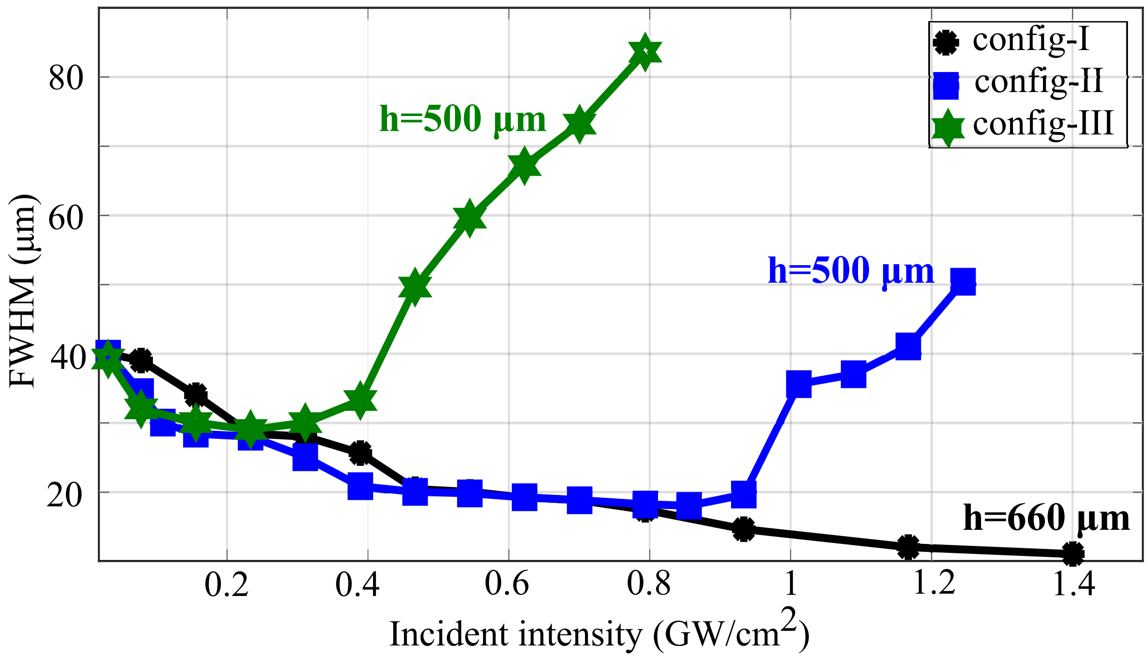

Figure 4.15: Evolution of output beam width as a function of input peak intensity for the three configurations I, II and III for TM polarization.

strong self-focussing followed by the localization of light in very small volume is observed as we increase the intensity. The observed focusing and widening of light in relation to the PS position on the dielectric allows tunability in the light propagation or in the beam self-action effects.

4.2.5/ INFLUENCE OF METAL LENGTH ON FIELD ENHANCEMENT

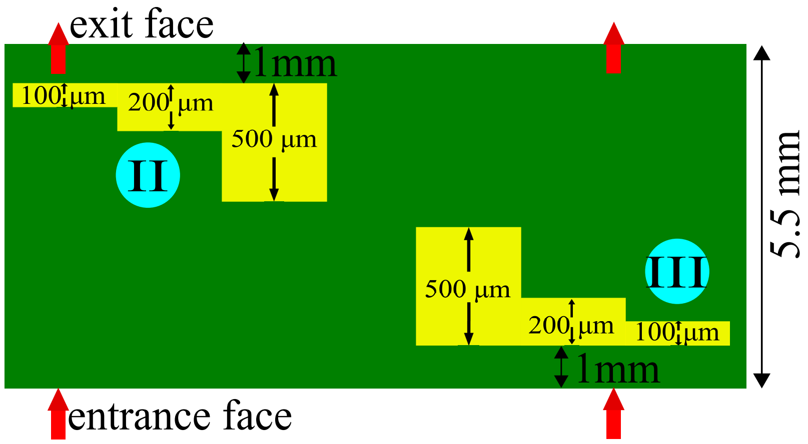

Figure 4.16: Schematic illustration of top view of the PS staircase pattern.

The previous characterization has been realized with 500 μm and 660 μm long PS. To analyse the impact of the PS length for TM polarized waves, experiments have also been conducted for PS lengths of 100 μm, 200 μm and 500 μm for configuration II and configuration III (Fig. 4.16).

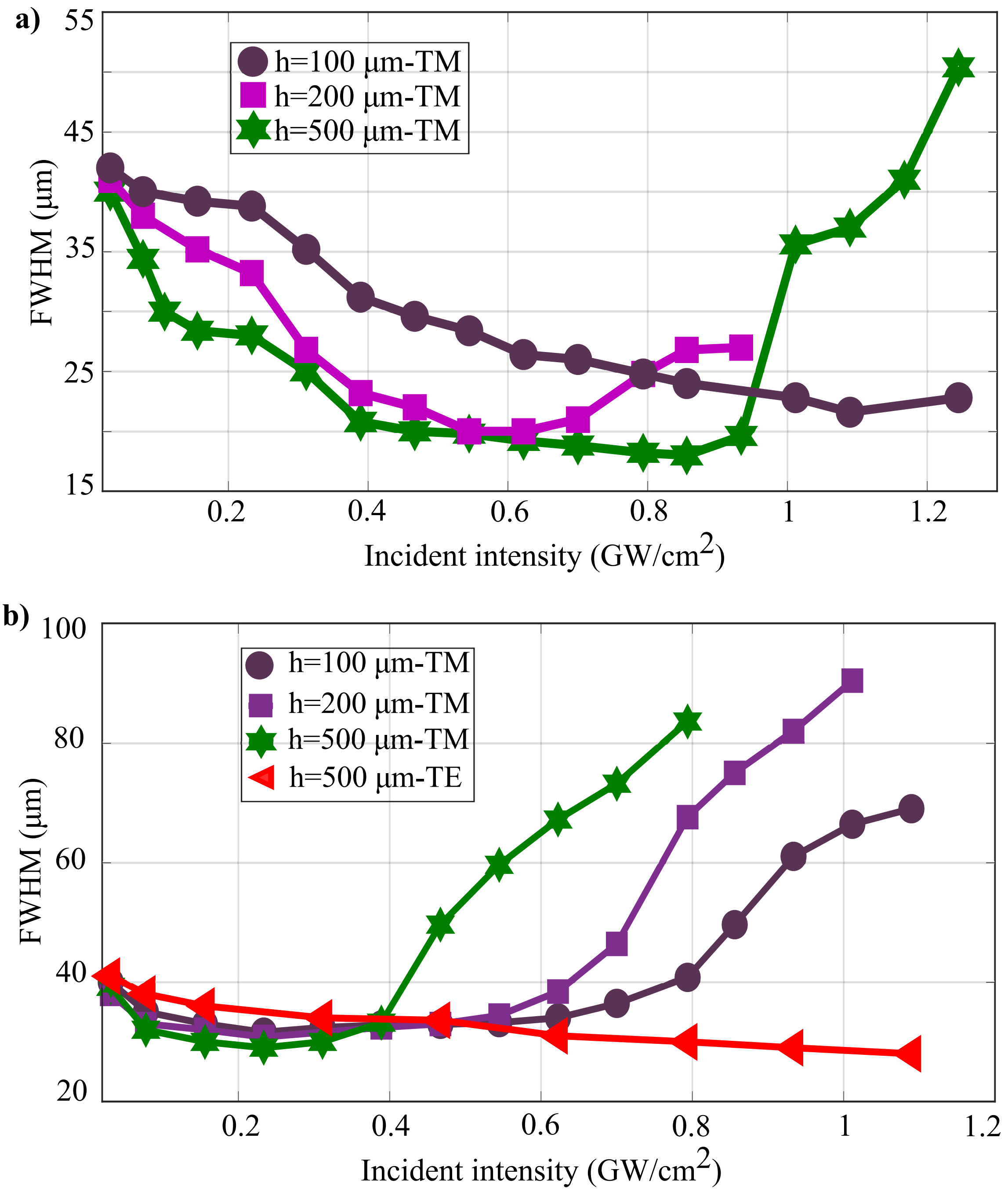

Figure 4.17: (a) Evolution of output beam width for PS length of 500 μm, 200 μm and 100 μm for configuration II for TM and TE polarizations, (b) for configuration III with TM polarization.

The obtained results are presented in Fig. 4.17(a) and (b). Measurements made with TE polarization is shown as a reference in Fig. 4.17(b). For TM modes, beam narrowing and widening effects are observed. At low intensity, the PS enhances the self-focusing effect observed at the output face. Shorter PS give rise to weaker nonlinear focusing for the two configurations. For instance, for configuration II, at an intensity of 0.23 GW/cm^2 the measured output beam FWHM is 39 μm , 33.2 μm and 28 μm for 100 μm, 200 μm and 500 μm PS length, respectively. With configuration III at an intensity of 0.23 GW/cm^2 the measured output beam FWHM is 31.6 μm, 30.7 μm and 29 μm for 100 μm, 200 μm and 500 μm PS length, respectively. As the intensity is further increased, the improved confinement brought by the PS gradually diminishes until the threshold intensity is reached which is characterized by the sudden defocusing. This threshold intensity raises as the PS length is reduced. Such a behaviour is expected since short PS lengths necessitate larger intensity to induce the same small spot size than in a longer PS. It is however remarkable that beam width, that we can infer to be on the order of 10 to 12 μm, can be induced by a PS as short as 100 μm. Note that, beam widening effect in accordance with the PS length is weaker in configuration II than configuration III since the PS is closer to the exit face. So we conclude that, we can control the behaviour of light in a NPW by choosing the PS length. In addition, these results could be used for the design of photonic circuits where large nonlinear effects over short distance are requested.

4.2.6/ SPATIAL MODULATION INSTABILITY

Furthermore, analysis of the output beam profile provides additional information on the strong nonlinearity seen by the propagating beam. Same characteristics than that modulation instability (MI) is present at high incident intensity. The nonlinearities induced spatial and temporal instabilities have been studied in a variety of fields such as nonlinear fibre optics, plasma physics and fluid dynamics [206]. Fundamentally, MI is a phenomenon in which a beam propagating in a nonlinear media undergoes modulation of its amplitude triggered by initial small perturbations or noise. This process may eventually grow until the beam break-up into sub beams. In the spatial domain, MI occurs due to the interplay between the nonlinear self-focusing and the diffraction in the medium, whereas in the temporal domain, MI occurs through the interplay between the nonlinearity and the dispersion effects. The existence of MI in a medium can be used for several applications including white light generation [206] and the generation of ultrashort pulses [38]. This section will present some clues that indicate that spatial MI is playing a role in the plasmon enhanced self-focusing.

In Fig. 4.18 the output beam profile is plotted for 6 intensity values for a 500 μm long PS positioned 1 mm from the output face (configuration II). The previously described beam diffraction at low intensity is shown in Fig. 4.18(a). The efficient focusing effect forms a smooth profile beam (Fig. 4.18(b)). This beam then enlarges and develops symmetric side lobes on both sides of the main peak as the intensity is raised (Fig. 4.18(c-d). The

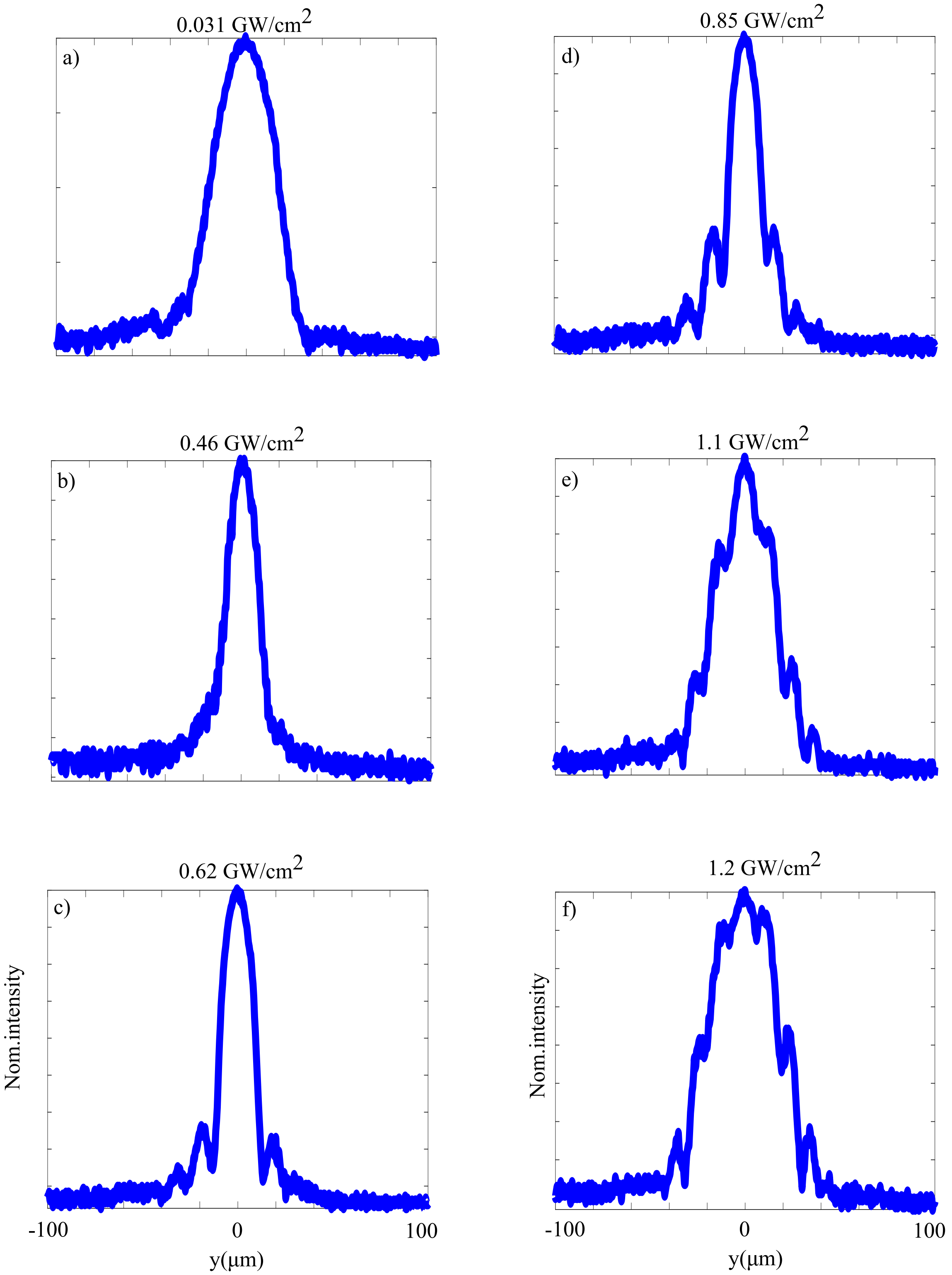

Figure 4.18: Beam profile at the output of the 5.5 mm long sample as a function of incident intensity for TM polarization. PS length is 500 μm, configuration III.

amplitude of the generated side lobes increases as we increase the incident intensity. At an intensity of 1.1 GW/cm^2 (Fig. 4.18(e)) additional peaks and the splitting to form a top hat beam is observed. For an intensity of 1.2 GW/cm^2 (Fig. 4.18(f)), a more pronounced beam broadening is observed. Such beam profiles are a signature of the MI that has been observed in the time domain in presence of strong nonlinearity [207, 208]. Note that, we didn't go above an intensity of 1.2 GW/cm^2 to prevent the input facet damage. Moreover, when the intensity is lowered, the diffraction regime observed at 0.031 GW/cm^2 is recovered which excludes the presence of permanent photoinduced effects.

MI is thus an additional consequence of the plasmon enhanced nonlinearity even if we miss a theoretical study to validate the observations. A detailed study has to be conducted in the future to have a clear understanding of the lateral maximum induced by the plasmonic effects.

4.3/ PHOTOSENSITIVITY OF CHALCOGENIDE PLASMONIC WAVEGUIDE

Besides the above mentioned results, we studied the photosensitivity of the fabricated chalcogenide plasmonic waveguide at the wavelength of 1550 nm. By comparison with the similar studies on chalcogenide planar waveguides discussed in chapter 3, we used a lower input intensity of 0.3 GW/cm^2 to analyse the presence of irreversible index changes. Light was coupled in the sample for almost an hour. The used experimental setup is the same as in Fig. 4.7. Since we observed a very strong self-trapping and plasmon enhanced nonlinear effects in configuration I, we chose the same sample piece for photosensitivity studies. The obtained results are shown in Fig. 4.19. At the beginning ($t = 0$ s), an input beam of 31 μm FWHM undergoes free diffraction to 42 μm within a 5.1 mm long sample like in the beam self-action analysis (Fig. 4.19(a). As time progresses, a gradual increase in beam width is observed (Fig. 4.19 (b-d)). At $t = 1860$ s, the FWHM of the diffracted beam is 57 μm (Fig. 4.19(e)). It is obviously accompanied with a reduction in the peak intensity. Beam widening and reduction in peak intensity became conspicuous with time. At $t = 2340$ s, strong widening and beam splitting is recorded (Fig. 4.19(f)). It is important to note that the observed effects are non reversible and a permanent index change is recorded even after the illumination is removed.

By comparing this results with the one observed in the pure dielectric waveguide made of Se2 mentioned in chapter 3, we found that the photoinduced effect follows the same trend in both structures. The presence of the PS on top of chalcogenide guiding layer has no particular influence on the photosensitive effects. Note that the incident intensity used for the photosensitivity study described in chapter 3 and the above mentioned study are not the same thus a longer illumination time is required at low intensity to obtain similar results than as high intensity.

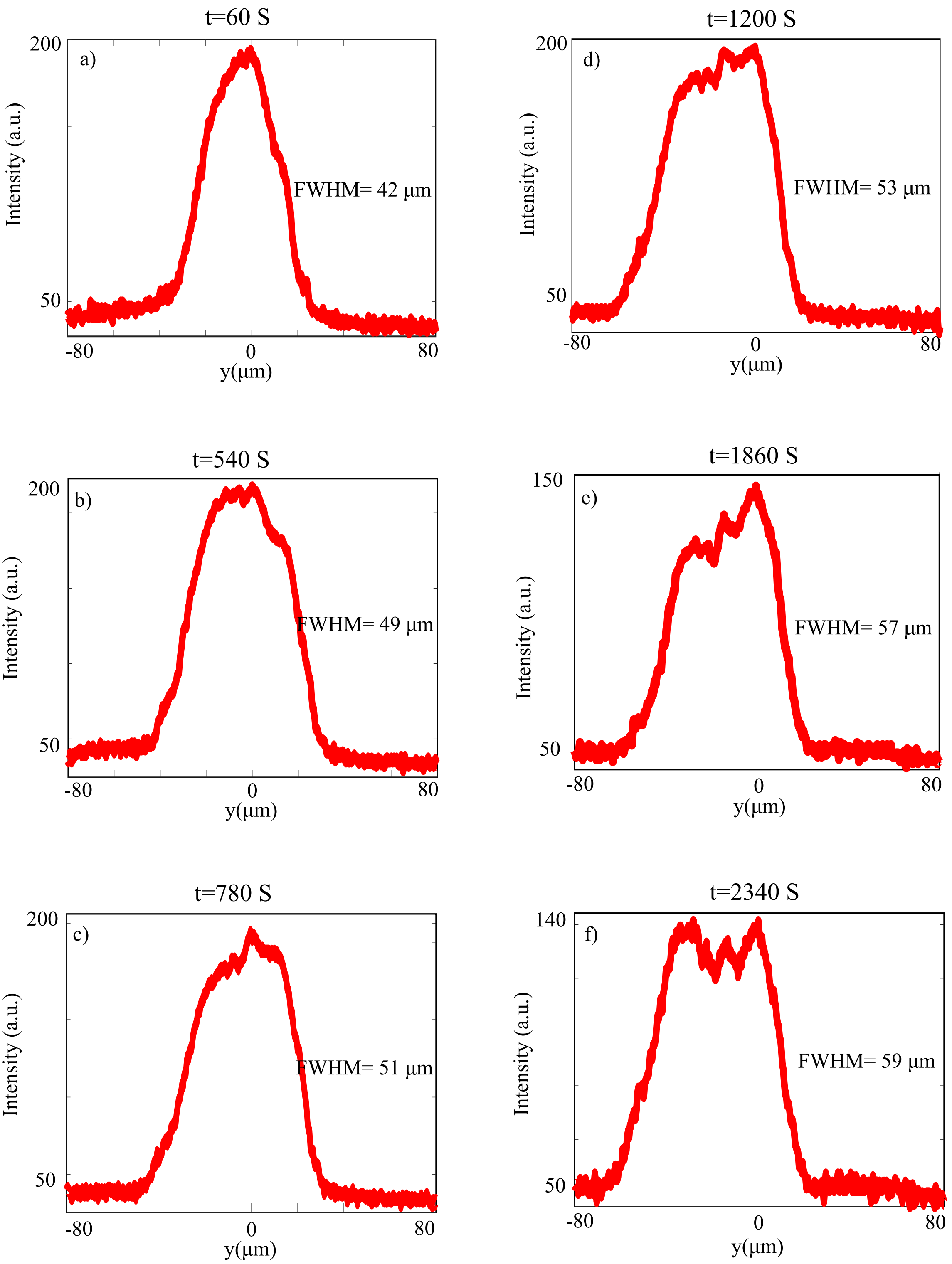

Figure 4.19: Temporal evolution of the optical beam distribution at the output of the NPW for an input intensity of about 0.3 GW/cm^2 (a- f). Configuration I, metallic layer length is 660 μm.

4.4/ SUMMARY

In this chapter, we have reported for the first time the experimental observation of plasmon-soliton coupling that have been predicted in many theoretical publications since the 1980's. To reach this goal a proper structure has been designed and fabricated. The analysed structure consists of a highly nonlinear chalcogenide layer, on a SiO_2 substrate, covered by a 10 nm thick SiO_2 buffer layer and a thin layer of gold deposited on top of it. The thickness of the silica layer has been chosen to optimize the plasmonic confinement while limiting the propagation losses. The structure was successfully used to demonstrate the plasmonic enhanced nonlinear effects.

We have analysed the characteristics of plasmon enhanced self-focusing through various experimental results. The strong confinement and localization of light observed only for the TM polarization confirms its plasmonic character. A strong confinement of light is directly observed for PS exactly located at the exit face of the waveguide. (1+1)-D BPM simulations have been used to estimate the intensity improvement provided by the PS compared to a simple chalcogenide waveguide.

We have shown that Kerr focusing can lead to dramatic beam widening by positioning the PS away from the sample output. The studied structure can thus act as an efficient beam intensity limiter whose threshold is set by the position of the PS. The study conducted for different PS lengths reveals that a giant focused beam of 12 μm can also be induced in PS lengths as short as 100 μm but with higher intensity than in a longer PS lengths. In addition, we have presented the features of spatial MI induced by the plasmon enhanced Kerr nonlinearity as well as the photoinduced effects in the fabricated NPW.

CONCLUSIONS AND PERSPECTIVES

This PhD thesis deals with a study in the field of nonlinear plasmonics. The main goal of this thesis is to demonstrate the formation of self-trapped plasmons that lead to a new type of hybrid wave: soliton-plasmon. This concept has been theoretically studied in many publications since the 1980's but no experimental observations had been reported to date. The principle reason is that the nonlinear refractive index change required for the formation of hybrid plasmon-soliton wave in all the proposed configurations necessitates light intensity that exceeds the damage threshold of typical nonlinear materials. Another reason is the large metallic losses that limit the propagation length. To achieve this goal, combination of modelling, design of structure and experimental investigation was required. Hence, this project was developed in collaboration with the theoreticians from the Fresnel Institute of Marseille in France and material specialists from the Institute of Chemical Sciences of Rennes in France. I have conducted a series of experiments and simulations to reach our goal. The main contributions of this thesis are summarized below.

We started with the design and fabrication of a planar waveguide that supports the propagation of spatial solitons at low intensity. Chalcogenide glasses are opted due to their large Kerr nonlinearities, low linear and nonlinear absorption losses and low-cost fabrication techniques. Chalcogenide glass composition of Ge-Sb-Se was specifically chosen since it has good thermal, mechanical and chemical properties. The fabrication of planar waveguides were carried out by the RF sputtering technique. Three type of selenide compositions are selected, $Ge_{12.5}Sb_{25}Se_{62.5}$, $Ge_{19.4}Sb_{16.7}Se_{63.9}$ and $Ge_{28.1}Sb_{6.3}Se_{65.6}$ later called Se6, Se4 and Se2 respectively. They have excellent mid-IR transparency, high stability against crystallization and refractive index contrast allowing optical waveguiding when associated with silica cladding.

Optical properties of the selected compositions have been analysed by scanning electron microscopy (SEM), variable angle spectroscopic ellipsometry (VASE) and prism coupling technique. The results show that Se6 has the lowest bandgap energy and the highest value of linear refractive index. In addition, cutback method is used to determine the propagation losses of the planar waveguides at the wavelengths of 1200 nm and 1550 nm. At the wavelength of 1550 nm linear losses range from 0.19 cm^{-1} to 0.26 cm^{-1} depending on the chalcogenide compositions whereas larger losses range from 0.63 cm^{-1} to 0.76

cm^{-1} are measured at 1200 nm. Among the three studied composition, the minimum value of linear loss is found in Se2 due to its larger band gap energy.

Subsequently, we have explored the nonlinear optical properties of these waveguides. We have designed and set up an optical bench based on a tunable femtosecond optical parametric oscillator. Nonlinear absorption coefficients were determined by transmission analysis at 1550 nm and 1200 nm. Measurements show that the nonlinear losses are negligible in our waveguides especially at 1550 nm.

To analyse the Kerr effect we have introduced a new experimental technique based on the analysis of the beam-self-trapping as an alternative to the well-known z-scan, SPM or wave mixing that cannot be applied to easily characterize planar waveguides. Optical nonlinearities in chalcogenide waveguides are studied at 1200 nm and 1550 nm wavelengths. Characterizations show that the fabricated slab waveguides can support low power spatial solitons. The largest Kerr coefficient of (32 ± 5) x 10^{-18} m^2/W is measured in the Se6 films at 1200 nm, whereas lowest Kerr coefficient of (5.5 ± 2) x 10^{-18} m^2/W is found in the Se2 films at 1550 nm. The obtained n_2 values are consistent with measurements performed with other techniques in bulk samples of similar composition. The experimental observation of an efficient beam self-trapping and soliton-like behavior in Se4 chalcogenide waveguide due to a non reversible photoinduced effect is also reported.

Thereupon, we have presented the theoretical design and fabrication of a nonlinear plasmonic structure. A five layer structure composed of a low index dielectric substrate (SiO_2)/ nonlinear dielectric (chalcogenide)/ buffer linear dielectric (SiO_2)/ metal (Au)/ external linear dielectric (air) has been designed and studied. This configuration is made to support plasmon-soliton with moderate losses. In addition, the proposed structure is compatible with the available fabrication technique. Performed numerical simulations show that the designed planar structure supports a fundamental TE mode profile at NIR wavelengths whose transverse profile is not affected by the metal layer while the TM mode is clearly confined at the SiO_2-metal-chalcogenide interfaces due to the plasmonic effect. In nonlinear regime an enhanced self-focusing effect is thus expected for this TM wave since its intensity is higher compared to the TE polarized one. We have also shown that the field confinement at the metal-dielectric interface can be tailored by adjusting the thickness of buffer SiO_2 layer. Furthermore, we have chosen the thickness of the chalcogenide layer to ease the experimental observation of plasmon-soltion waves.

Se2 composition has been selected as a nonlinear medium for the fabricated PS due to its large Kerr nonlinearity (n_2 = 5.5 x $(10^{-18} m^2.W^{-1})$, low nonlinear absorption coefficient (α_2 = 0.43 cm/GW) and high intensity damage threshold evaluated to 2 GW/cm^2. Sputtering technique was used to deposit the chalcogenide layer on an oxidized silicon substrate.

A SiO_2 pattern followed by a gold layer was then laid on top. We have analysed the thickness of each layer by SEM. The chalcogenide layer is 3.6 μm, the SiO_2 buffer layer is 10 nm, and the gold layer is 32 nm in thickness which are found to be in good agreement with the targeted thickness.

Using these nonlinear plasmonic structures, we have then successfully demonstrated an enhanced self-focusing by the plasmon-soliton coupling. The extreme self confinement observed only with TM polarization is a key characteristics of the plasmonic effect. BPM simulations have been performed to evaluate the intensity enhancement induced by the plasmon. It shows that the intensity under the plasmonic structure (PS) is at least 5 fold higher than the non PS zone.

A detailed characterization has also been conducted which clearly exposes the properties of the plasmon enhanced focusing. The different tested configurations reveal that two types of behavior exist in the nonlinear plasmonic waveguide (NPW). When the PS is positioned close to the input facet of the sample, self-focusing is obtained at low intensity but transform to defocusing above an intensity threshold. Contrarily, the positioning of the PS at the output facet of the sample results in a tight focusing without beam broadening. We have also shown that the tightly confined beam of 12 μm FWHM can be achieved even in a PS length as shot as 100 μm. Moreover, we have observed modulation instabilities in the output beam profiles due to the plasmon enhanced nonlinearity.

This first experimental proof validates the concept of the nonlinear spatial optical self-trapping enhanced by the assistance of a plasmon polariton. It also let envision the possibility to extend the demonstration to other nonlinear surface waves. A more detailed study of the surface waves will provide better insights into the mechanism of enhanced nonlinear/plasmonic effects disclosed in this thesis. Nonlinearity predicted by the metal could be suspected.

In essence, there are a lot of exciting things we can do with the plasmonic enhanced self-trapped wave. First, to better analyse the effect, observations of the trapped beam using scanning near field optical microscopy are planned. Samples with thinner gold layer could be fabricated to ease the SNOM imaging as the plasmon propagates in the PS. Similarly, characterization of the hybrid wave in the temporal domain could provide a deeper understanding of the presented results.

The extension of plasmon-soliton studies to other materials can lead to many interesting results. For instance, plasmon-soliton formation in graphene can further enhance the optical properties of this versatile material via the improved light-matter interactions in graphene [209]. Further, more research on structure improvement and material parameters will be of great interest from the view points of fabrication, experiment and control of the plasmon-soliton properties.

Finally, the first experimental evidence of enhanced optical nonlinearity by plasmons reported in this work can act as a guideline for the realization of exciting applications, the formation of shape preserving plasmon-soliton wave and the demonstration of new physical phenomena.

BIBLIOGRAPHY

[1] BOYD, R. W. **Nonlinear optics**, 3rd ed ed. Academic Press, Amsterdam ; Boston, 2008.

[2] CHIAO, R. Y., GARMIRE, E., AND TOWNES, C. H. **Self-trapping of optical beams**. *Physical Review Letters 13*, 15 (1964), 479.

[3] TRILLO, S., AND TORRUELLAS, W. **Spatial solitons**. Springer Berlin Heidelberg, 2001. OCLC: 861705592.

[4] KAURANEN, M., AND ZAYATS, A. V. **Nonlinear plasmonics**. *Nature Photonics 6*, 11 (Nov. 2012), 737–748.

[5] MAIER, S. A. **Plasmonics: fundamentals and applications**. Springer, New York, 2007.

[6] CUNNINGHAM, S. L., MARADUDIN, A. A., AND WALLIS, R. F. **Effect of a charge layer on the surface-plasmon-polariton dispersion curve**. *Physical Review B 10*, 8 (1974), 3342.

[7] BRONGERSMA, M. L. **Introductory lecture: nanoplasmonics**. *Faraday Discuss. 178* (2015), 9–36.

[8] ATWATER, H. A. **promise of plasmonics**. *SCIENTIF IC AMERIC AN 4* (2007), 296.

[9] SKRYABIN, D. V., GORBACH, A. V., AND MARINI, A. **Surface-induced nonlinearity enhancement of TM modes in planar subwavelength waveguides**. *JOSA B 28*, 1 (Jan. 2011), 109–114.

[10] MARINI, A., SKRYABIN, D. V., AND MALOMED, B. **Stable spatial plasmon solitons in a dielectric-metal-dielectric geometry with gain and loss**. *Optics Express 19*, 7 (Mar. 2011), 6616–6622.

[11] SIMON, H. J., MITCHELL, D. E., AND WATSON, J. G. **Optical Second-Harmonic Generation with Surface Plasmons in Silver Films**. *Physical Review Letters 33*, 26 (Dec. 1974), 1531–1534.

[12] ALAM, M. Z., AITCHISON, J. S., AND MOJAHEDI, M. **A marriage of convenience: Hybridization of surface plasmon and dielectric waveguide modes**. *Laser & Photonics Reviews 8*, 3 (May 2014), 394–408.

[13] M.AGRANOVICH, V., BABICHENKO, V., AND CHERNYAK, V. **Nonlinear surface polaritons**. *JETP Lett 32* (1980), 512–515.

[14] TOMLINSON, W. J. **Surface wave at a nonlinear interface**. *Optics Letters 5*, 7 (July 1980), 323–325.

[15] N.AKHMEDIEV, N. **Novel class of nonlinear surface waves: asymmetric modes in a symmetric layered structure**. *Sov. Phys. JETP 56* (1982), 299–303.

[16] ARIYASU, J., SEATON, C. T., STEGEMAN, G. I., MARADUDIN, A. A., AND WALLIS, R. F. **Nonlinear surface polaritons guided by metal films**. *Journal of Applied Physics 58*, 7 (Oct. 1985), 2460–2466.

[17] MARADUDIN, A. A. **Nonlinear surface electromagnetic waves**. World Scientific, Singapore, 1983.

[18] STEGEMAN, G. I., SEATON, C. T., ARIYASU, J., WALLIS, R. F., AND MARADUDIN, A. A. **Nonlinear electromagnetic waves guided by a single interface**. *Journal of Applied Physics 58*, 7 (Oct. 1985), 2453–2459.

[19] BLIOKH, K. Y., BLIOKH, Y. P., AND FERRANDO, A. **Resonant plasmon-soliton interaction**. *Physical Review A 79*, 4 (Apr. 2009), 041803.

[20] DAVOYAN, A. R., SHADRIVOV, I. V., AND KIVSHAR, Y. S. **Nonlinear plasmonic slot waveguides**. *Optics Express 16*, 26 (Dec. 2008), 21209–21214.

[21] GAO, L., TANG, L., HU, F., GUO, R., WANG, X., AND ZHOU, Z. **Active metal strip hybrid plasmonic waveguide with low critical material gain**. *Optics Express 20*, 10 (May 2012), 11487–11495.

[22] FEIGENBAUM, E., AND ORENSTEIN, M. **Plasmon-soliton**. *Optics Letters 32*, 6 (Mar. 2007), 674–676.

[23] DAVOYAN, A. R., SHADRIVOV, I. V., AND KIVSHAR, Y. S. **Self-focusing and spatial plasmon-polariton solitons**. *Optics Express 17*, 24 (Nov. 2009), 21732–21737.

[24] DEGIRON, A., AND SMITH, D. R. **Nonlinear long-range plasmonic waveguides**. *Physical Review A 82*, 3 (Sept. 2010), 033812.

[25] HUANG, C.-C. **Analysis of long-range surface plasmon polaritons in nonlinear plasmonic waveguides using pseudospectral method**. *Optics Express 20*, 17 (Aug. 2012), 18665–18678.

[26] WALASIK, W., NAZABAL, V., CHAUVET, M., KARTASHOV, Y., AND RENVERSEZ, G. **Low-power plasmon–soliton in realistic nonlinear planar structures**. *Optics Letters 37*, 22 (Nov. 2012), 4579–4581.

[27] FERRANDO, A., MILIÁN, C., AND SKRYABIN, D. V. **Variational theory of soliplasmon resonances**. *JOSA B 30*, 9 (Sept. 2013), 2507–2522.

[28] WALASIK, W., RENVERSEZ, G., AND KARTASHOV, Y. **Stationary plasmon-soliton waves in metal-dielectric nonlinear planar structures: modeling and properties**. *Physical Review A 89*, 2 (Feb. 2014). arXiv: 1311.7347.

[29] WALASIK, W. **Plasmon-soliton waves in metal-nonlinear dielectric planar structures**. PhD thesis, Aix-Marseille, Oct. 2014.

[30] ELSAWY, M. M. R., AND RENVERSEZ, G. **Improved nonlinear slot waveguides using dielectric buffer layers: properties of TM waves**. *Optics Letters 41*, 7 (Apr. 2016), 1542–1545.

[31] WALASIK, W., AND RENVERSEZ, G. **Plasmon-soliton waves in planar slot waveguides. I. Modeling**. *Physical Review A 93*, 1 (Jan. 2016), 013825.

[32] DIAZ, F. J., LI, G., STERKE, C. M. D., KUHLMEY, B. T., AND PALOMBA, S. **Kerr effect in hybrid plasmonic waveguides**. *JOSA B 33*, 5 (May 2016), 957–962.

[33] GARMIRE, E. **Nonlinear optics in daily life**. *Optics Express 21*, 25 (Dec. 2013), 30532–30544.

[34] NIE, W. **Optical Nonlinearity:Phenomena, applications, and materials**. *Advanced Materials 5*, 7-8 (July 1993), 520–545.

[35] JACKSON, J. D. **Classical Electrodynamics Third Edition**, 3 edition ed. Wiley, Hoboken, NY, Aug. 1998.

[36] GRIFFITHS, D. J. **Introduction to Electrodynamics**, 3rd ed ed. Prentice Hall, 1999.

[37] SALEH, B. E. A., AND TEICH, M. C. **Nonlinear Optics**. In *Fundamentals of Photonics*. John Wiley & Sons, Inc., 1991, pp. 737–798.

[38] AGRAWAL, G. P. **Nonlinear Fiber Optics**. Academic Press, 2013.

[39] NEW, G. **Introduction to Nonlinear Optics**. Cambridge University Press, Cambridge ; New York, 2011.

[40] SHEN, Y.-R. **Self-focusing: experimental**. *Progress in Quantum Electronics 4* (1975), 1–34.

[41] Zhang, Q., Cheng, X. M., Chen, H. W., He, B., Ren, Z. Y., Zhang, Y., and Bai, J. T. **Diffraction-free, self-reconstructing Bessel beam generation using thermal nonlinear optical effect**. *Applied Physics Letters 111*, 16 (Oct. 2017), 161103.

[42] Chiao, R. Y., Gustafson, T. K., and Kelley, P. L. **Self-focusing of optical beams**. In *Self-Focusing: Past and Present*. Springer, 2009, pp. 129–143.

[43] Murti, Y. V. G. S., and Vijayan, C. **Essentials of nonlinear optics**. Wiley, Chichester, 2014. OCLC: 915479355.

[44] Monot, P., Auguste, T., Gibbon, P., Jakober, F., Mainfray, G., Dulieu, A., Louis-Jacquet, M., Malka, G., and Miquel, J. L. **Experimental Demonstration of Relativistic Self-Channeling of a Multiterawatt Laser Pulse in an Underdense Plasma**. *Physical Review Letters 74*, 15 (Apr. 1995), 2953–2956.

[45] Borisov, A. B., Borovskiy, A. V., Korobkin, V. V., Prokhorov, A. M., Shiryaev, O. B., Shi, X. M., Luk, T. S., McPherson, A., Solem, J. C., Boyer, K., and Rhodes, C. K. **Observation of relativistic and charge-displacement self-channeling of intense subpicosecond ultraviolet (248 nm) radiation in plasmas**. *Physical Review Letters 68*, 15 (Apr. 1992), 2309–2312.

[46] Khrapko, R., Lai, C., Casey, J., Wood, W. A., and Borrelli, N. F. **Accumulated self-focusing of ultraviolet light in silica glass**. *Applied Physics Letters 105*, 24 (Dec. 2014), 244110.

[47] Menzel, R. **Photonics: linear and nonlinear interactions of laser light and matter**, 2nd ed ed. Springer, Berlin ; New York, 2007.

[48] Barthelemy, A., Maneuf, S., and Froehly, C. **Propagation soliton et autoconfinement de faisceaux laser par non linearité optique de kerr**. *Optics Communications 55*, 3 (Sept. 1985), 201–206.

[49] Lonngren, K. E. **Soliton experiments in plasmas**. *Plasma Physics 25*, 9 (1983), 943.

[50] Polturak, E., deVegvar, P. G. N., Zeise, E. K., and Lee, D. M. **Solitonlike Propagation of Zero Sound in Superfluid $ˆ{3}\mathrm{He}$**. *Physical Review Letters 46*, 24 (June 1981), 1588–1591.

[51] Burger, S., Bongs, K., Dettmer, S., Ertmer, W., Sengstock, K., Sanpera, A., Shlyapnikov, G. V., and Lewenstein, M. **Dark Solitons in Bose-Einstein Condensates**. *Physical Review Letters 83*, 25 (Dec. 1999), 5198–5201.

[52] ZABUSKY, N. J., AND KRUSKAL, M. D. **Interaction of "Solitons" in a Collisionless Plasma and the Recurrence of Initial States**. *Physical Review Letters 15*, 6 (Aug. 1965), 240–243.

[53] SHABAT, A., AND ZAKHAROV, V. **Exact theory of two-dimensional self-focusing and one-dimensional self-modulation of waves in nonlinear media**. *Soviet physics JETP 34*, 1 (1972), 62.

[54] MENHOFER, A., SMITH, R. K., REEDER, M. J., AND CHRISTIE, D. R. **"Morning-Glory" Disturbances and the Environment in which They Propagate**. *Journal of the atmospheric sciences 54*, 13 (1997), 1712–1725.

[55] **Solitary water waves: http://www.math.upatras.gr/˜weele/weelerecentresearch_solitarywaterwaves.htm**.

[56] CHEN, Z., SEGEV, M., AND CHRISTODOULIDES, D. N. **Optical spatial solitons: historical overview and recent advances**. *Reports on Progress in Physics 75*, 8 (Aug. 2012), 086401.

[57] STEGEMAN, G. I., CHRISTODOULIDES, D. N., AND SEGEV, M. **Optical spatial solitons: historical perspectives**. *IEEE Journal of Selected Topics in Quantum Electronics 6*, 6 (2000), 1419–1427.

[58] BJORKHOLM, J. E., AND ASHKIN, A. A. **cw Self-Focusing and Self-Trapping of Light in Sodium Vapor**. *Physical Review Letters 32*, 4 (Jan. 1974), 129–132.

[59] AITCHISON, J. S., WEINER, A. M., SILBERBERG, Y., OLIVER, M. K., JACKEL, J. L., LEAIRD, D. E., VOGEL, E. M., AND SMITH, P. W. E. **Observation of spatial optical solitons in a nonlinear glass waveguide**. *Optics Letters 15*, 9 (May 1990), 471–473.

[60] AITCHISON, J. S., SILBERBERG, Y., WEINER, A. M., LEAIRD, D. E., OLIVER, M. K., JACKEL, J. L., VOGEL, E. M., AND SMITH, P. W. E. **Spatial optical solitons in planar glass waveguides**. *JOSA B 8*, 6 (June 1991), 1290–1297.

[61] HODEL, W., AND WEBER, H. P. **Decay of femtosecond higher-order solitons in an optical fiber induced by Raman self-pumping**. *Optics Letters 12*, 11 (Nov. 1987), 924–926.

[62] LEDERER, F., AND SILBERBERG, Y. **Discrete solitons**. *Optics and Photonics News 13*, 2 (2002), 48–53.

[63] EISENBERG, H. S., SILBERBERG, Y., MORANDOTTI, R., BOYD, A. R., AND AITCHISON, J. S. **Discrete spatial optical solitons in waveguide arrays**. *Physical Review Letters 81*, 16 (1998), 3383.

[64] BRAMBILLA, M., LUGIATO, L. A., PRATI, F., SPINELLI, L., AND FIRTH, W. J. **Spatial soliton pixels in semiconductor devices**. *Physical review letters 79*, 11 (1997), 2042.

[65] **http://www.funfacs.org/Overview/**.

[66] XIE, X.-T., LI, W.-B., AND YANG, X. **Bright, dark, bistable bright, and vortex spatial-optical solitons in a cold three-state medium**. *JOSA B 23*, 8 (Aug. 2006), 1609–1614.

[67] KIVSHAR, Y. S., AND LUTHER-DAVIES, B. **Dark optical solitons: physics and applications**. *Physics reports 298*, 2 (1998), 81–197.

[68] DESYATNIKOV, A., DENZ, C., AND KIVSHAR, Y. **Nonlinear optical beams carrying phase dislocations**. *Journal of Optics A: Pure and Applied Optics 6*, 5 (2004), S209.

[69] SWARTZLANDER, G. A., AND LAW, C. T. **Optical vortex solitons observed in Kerr nonlinear media**. *Physical Review Letters 69*, 17 (Oct. 1992), 2503–2506.

[70] SEGEV, M., CROSIGNANI, B., YARIV, A., AND FISCHER, B. **Spatial solitons in photorefractive media**. *Physical Review Letters 68*, 7 (1992), 923.

[71] LAN, S., SHIH, M.-F., MIZELL, G., GIORDMAINE, J. A., CHEN, Z., ANASTASSIOU, C., MARTIN, J., AND SEGEV, M. **Second-harmonic generation in waveguides induced by photorefractive spatial solitons**. *Optics Letters 24*, 16 (Aug. 1999), 1145–1147.

[72] LAN, S., DELRE, E., CHEN, Z., SHIH, M.-F., AND SEGEV, M. **Directional coupler with soliton-induced waveguides**. *Optics Letters 24*, 7 (Apr. 1999), 475–477.

[73] KARAMZIN, Y. N., AND SUKHORUKOV, A. P. **Mutual focusing of high-power light beams in media with quadratic nonlinearity**. *Sov. Phys. JETP 41*, 414 (1976).

[74] TORRUELLAS, W. E., WANG, Z., HAGAN, D. J., VANSTRYLAND, E. W., STEGEMAN, G. I., TORNER, L., AND MENYUK, C. R. **Observation of Two-Dimensional Spatial Solitary Waves in a Quadratic Medium**. *Physical Review Letters 74*, 25 (June 1995), 5036–5039.

[75] FRANKEN, P. A., HILL, A. E., PETERS, C. W., AND WEINREICH, G. **Generation of Optical Harmonics**. *Physical Review Letters 7*, 4 (Aug. 1961), 118–119.

[76] SEGEV, M. **Optical spatial solitons**. *Optical and Quantum Electronics 30*, 7 (1998), 503–533.

[77] Falcão-Filho, E. L., de Araújo, C. B., Boudebs, G., Leblond, H., and Skarka, V. **Robust Two-Dimensional Spatial Solitons in Liquid Carbon Disulfide**. *Physical Review Letters 110*, 1 (Jan. 2013), 013901.

[78] Barnes, W. L., Dereux, A., and Ebbesen, T. W. **Surface plasmon subwavelength optics**. *nature 424*, 6950 (2003), 824.

[79] Wood, R. W. **On a Remarkable Case of Uneven Distribution of Light in a Diffraction Grating Spectrum**. *Philosophical Magazine Series 6* (1902), 396–402.

[80] P.R.S, L. R. O. M. **III. Note on the remarkable case of diffraction spectra described by Prof. Wood**. *The London, Edinburgh, and Dublin Philosophical Magazine and Journal of Science 14*, 79 (July 1907), 60–65.

[81] Pines, D., and Bohm, D. **A collective description of electron interactions: II. Collective vs individual particle aspects of the interactions**. *Physical Review 85*, 2 (1952), 338.

[82] Pines, D. **Collective energy losses in solids**. *Reviews of modern physics 28*, 3 (1956), 184.

[83] Ritchie, R. H. **Plasma losses by fast electrons in thin films**. *Physical Review 106*, 5 (1957), 874.

[84] Powell, C. J., and Swan, J. B. **Origin of the characteristic electron energy losses in aluminum**. *Physical Review 115*, 4 (1959), 869.

[85] Fano, U. **Atomic theory of electromagnetic interactions in dense materials**. *Physical Review 103*, 5 (1956), 1202.

[86] Stern, E. A., and Ferrell, R. A. **Surface plasma oscillations of a degenerate electron gas**. *Physical Review 120*, 1 (1960), 130.

[87] Kretschmann E and Raether H. **Radiative Decay of Non Radiative Surface Plasmons Excited by Light**. *Naturf 23 a* (1968), 2135–2136.

[88] Zhang, J., Zhang, L., and Xu, W. **Surface plasmon polaritons: physics and applications**. *Journal of Physics D: Applied Physics 45*, 11 (Mar. 2012), 113001.

[89] Han, Z., and Bozhevolnyi, S. I. **Radiation guiding with surface plasmon polaritons**. *Reports on Progress in Physics 76*, 1 (Jan. 2013), 016402.

[90] Barnes, W. L. **Surface plasmon–polariton length scales: a route to subwavelength optics**. *Journal of Optics A: Pure and Applied Optics 8*, 4 (Apr. 2006), S87–S93.

[91] Zayats, A. V., and Smolyaninov, I. I. **Near-field photonics: surface plasmon polaritons and localized surface plasmons**. *Journal of Optics A: Pure and Applied Optics 5* (2003), S16–S50.

[92] Zayats, A. V., Smolyaninov, I. I., and Maradudin, A. A. **Nano-optics of surface plasmon polaritons**. *Physics Reports 408*, 3-4 (Mar. 2005), 131–314.

[93] Abdulhalim, I., Zourob, M., and Lakhtakia, A. **Surface Plasmon Resonance for Biosensing: A Mini-Review**. *Electromagnetics 28*, 3 (Mar. 2008), 214–242.

[94] Kashyap, R., and Nemova, G. **Surface Plasmon Resonance-Based Fiber and Planar Waveguide Sensors**. *Journal of Sensors 2009* (2009), 1–9.

[95] Sharma, A. K., Jha, R., and Gupta, B. D. **Fiber-Optic Sensors Based on Surface Plasmon Resonance: A Comprehensive Review**. *IEEE Sensors Journal 7*, 8 (Aug. 2007), 1118–1129.

[96] Homola, J., Yee, S. S., and Gauglitz, G. **Surface plasmon resonance sensors**. *Sensors and Actuators B: Chemical 54*, 1 (1999), 3–15.

[97] Otto, A. **Excitation of nonradiative surface plasma waves in silver by the method of frustrated total reflection**. *Zeitschrift für Physik 216*, 4 (1968), 398–410.

[98] Hecht, B., Bielefeldt, H., Novotny, L., Inouye, Y., and Pohl, D. W. **Local excitation, scattering, and interference of surface plasmons**. *Physical review letters 77*, 9 (1996), 1889.

[99] Raether, H. **Springer tracts in modern physics**, vol. 111. Springer-Verlag., 1988.

[100] Gramotnev, D. K., and Bozhevolnyi, S. I. **Plasmonics beyond the diffraction limit**. *Nature Photonics 4*, 2 (Feb. 2010), 83–91.

[101] Fang, Y., and Sun, M. **Nanoplasmonic waveguides: towards applications in integrated nanophotonic circuits**. *Light: Science & Applications 4*, 6 (June 2015), e294.

[102] Zia, R., Selker, M. D., Catrysse, P. B., and Brongersma, M. L. **Geometries and materials for subwavelength surface plasmon modes**. *J. Opt. Soc. Am. A 21*, 12 (2004).

[103] Avrutsky, I., Salakhutdinov, I., Elser, J., and Podolskiy, V. **Highly confined optical modes in nanoscale metal-dielectric multilayers**. *Physical Review B 75*, 24 (June 2007).

[104] Pitarke, J. M., Silkin, V. M., Chulkov, E. V., and Echenique, P. M. **Theory of surface plasmons and surface-plasmon polaritons**. *Reports on Progress in Physics 70*, 1 (Jan. 2007), 1–87.

[105] Sarid, D. **Long-range surface-plasma waves on very thin metal films**. *Physical Review Letters 47*, 26 (1981), 1927.

[106] Berini, P., and De Leon, I. **Surface plasmon–polariton amplifiers and lasers**. *Nature Photonics 6*, 1 (Dec. 2011), 16–24.

[107] Bozhevolnyi, S. I., Volkov, V. S., Devaux, E., Laluet, J.-Y., and Ebbesen, T. W. **Channel plasmon subwavelength waveguide components including interferometers and ring resonators**. *Nature 440*, 7083 (Mar. 2006), 508–511.

[108] Willets, K. A., and Van Duyne, R. P. **Localized Surface Plasmon Resonance Spectroscopy and Sensing**. *Annual Review of Physical Chemistry 58*, 1 (May 2007), 267–297.

[109] Kawata, S., Inouye, Y., and Verma, P. **Plasmonics for near-field nano-imaging and superlensing**. *Nature Photonics 3*, 7 (July 2009), 388–394.

[110] Elsayed, I., Huang, X., and Elsayed, M. **Selective laser photo-thermal therapy of epithelial carcinoma using anti-EGFR antibody conjugated gold nanoparticles**. *Cancer Letters 239*, 1 (July 2006), 129–135.

[111] Fortina, P., Kricka, L. J., Graves, D. J., Park, J., Hyslop, T., Tam, F., Halas, N., Surrey, S., and Waldman, S. A. **Applications of nanoparticles to diagnostics and therapeutics in colorectal cancer**. *Trends in Biotechnology 25*, 4 (Apr. 2007), 145–152.

[112] Anker, J. N., Hall, W. P., Lyandres, O., Shah, N. C., Zhao, J., and Van Duyne, R. P. **Biosensing with plasmonic nanosensors**. *Nature materials 7*, 6 (2008), 442–453.

[113] Pendry, J. B. **Negative refraction makes a perfect lens**. *Physical review letters 85*, 18 (2000), 3966.

[114] Akimov, A. V., Mukherjee, A., Yu, C. L., Chang, D. E., Zibrov, A. S., Hemmer, P. R., Park, H., and Lukin, M. D. **Generation of single optical plasmons in metallic nanowires coupled to quantum dots**. *Nature 450*, 7168 (Nov. 2007), 402–406.

[115] Zijlstra, P., Chon, J. W. M., and Gu, M. **Five-dimensional optical recording mediated by surface plasmons in gold nanorods**. *Nature 459*, 7245 (May 2009), 410–413.

[116] Berini, P. **Long-range surface plasmon polaritons**. *Advances in Optics and Photonics 1*, 3 (Nov. 2009), 484.

[117] Fan, W., Zhang, S., Panoiu, N.-C., Abdenour, A., Krishna, S., Osgood, R. M., Malloy, K. J., and Brueck, S. R. J. **Second Harmonic Generation from a Nanopatterned Isotropic Nonlinear Material**. *Nano Letters 6*, 5 (May 2006), 1027–1030.

[118] Davoyan, A. R., Shadrivov, I. V., and Kivshar, Y. S. **Quadratic phase matching in nonlinear plasmonic nanoscale waveguides**. *Optics Express 17*, 22 (Oct. 2009), 20063–20068.

[119] Panoiu, N.-C., and Osgood, R. M. **Subwavelength Nonlinear Plasmonic Nanowire**. *Nano Letters 4*, 12 (Dec. 2004), 2427–2430.

[120] Eggleton, B. J., Luther-Davies, B., and Richardson, K. **Chalcogenide photonics**. *Nature Photonics 5*, 3 (Mar. 2011), 141.

[121] Leuthold, J., Koos, C., and Freude, W. **Nonlinear silicon photonics**. *Nature Photonics 4*, 8 (Aug. 2010), 535.

[122] Aitchison, J. S., Hutchings, D. C., Kang, J. U., Stegeman, G. I., and Villeneuve, A. **The nonlinear optical properties of AlGaAs at the half band gap**. *IEEE Journal of Quantum Electronics 33*, 3 (Mar. 1997), 341–348.

[123] Coda, V., Swain, R. D., Maillotte, H., Salamo, G. J., and Chauvet, M. **Wavelength, power and pulse duration influence on spatial soliton formation in AlGaAs**. *Optics Communications 251*, 1 (July 2005), 186–193.

[124] Jensen, W. B. **A Note on the Term ”Chalcogen”**. *Journal of Chemical Education 74*, 9 (Sept. 1997), 1063.

[125] Yamane, M., and Asahara, Y. **Glasses for Photonics**. Cambridge University Press, May 2000. Google-Books-ID: Ksit4QF8ja8C.

[126] Taeed, V. G., Baker, N. J., Fu, L., Finsterbusch, K., Lamont, M. R. E., Moss, D. J., Nguyen, H. C., Eggleton, B. J., Choi, D. Y., Madden, S., and Luther-Davies, B. **Ultrafast all-optical chalcogenide glass photonic circuits**. *Optics Express 15*, 15 (July 2007), 9205–9221.

[127] Hewak, D. W., Brady, D., Curry, R. J., Elliott, G., Huang, C.-C., Hughes, M., Knight, K., Mairaj, A., Petrovich, M. N., and Simpson, R. E. **Chalcogenide glasses for photonics device applications**. *Research Signpost, Kerala, India* (2010).

[128] Zakery, A., and Elliott, S. R. **Optical Nonlinearities in Chalcogenide Glasses and their Applications**, 2007 edition ed. Springer, New York, Aug. 2007.

[129] Calvez, L. **Chalcogenide glasses and glass-ceramics: Transparent materials in the infrared for dual applications**. *Comptes Rendus Physique 18*, 5 (May 2017), 314–322.

[130] Verger, F., Nazabal, V., Colas, F., Němec, P., Cardinaud, C., Baudet, E., Chahal, R., Rinnert, E., Boukerma, K., Peron, I., Deputier, S., Guilloux-Viry, M., Guin, J., Lhermite, H., Moreac, A., Compère, C., and Bureau, B. **RF sputtered amorphous chalcogenide thin films for surface enhanced infrared absorption spectroscopy**. *Optical Materials Express 3*, 12 (Dec. 2013), 2112.

[131] Adam, J.-L., and Zhang, X. **Chalcogenide Glasses: Preparation, Properties and Applications**. Woodhead Publishing, Feb. 2014. Google-Books-ID: IuN-RAwAAQBAJ.

[132] Vigreux-Bercovici, C., Ranieri, V., Labadie, L., Broquin, J. E., Kern, P., and Pradel, A. **Waveguides based on Te2as3se5 thick films for spatial interferometry**. *Journal of Non-Crystalline Solids 352*, 23 (July 2006), 2416–2419.

[133] Zhang, X., Bureau, B., Lucas, P., Boussard-Pledel, C., and Lucas, J. **Glasses for Seeing Beyond Visible**. *Chemistry – A European Journal 14*, 2 (Jan. 2008), 432–442.

[134] Baudet, E., Gutierrez-Arroyo, A., Němec, P., Bodiou, L., Lemaitre, J., Sagazan, O. D., Lhermitte, H., Rinnert, E., Michel, K., Bureau, B., Charrier, J., and Nazabal, V. **Selenide sputtered films development for MIR environmental sensor**. *Optical Materials Express 6*, 8 (Aug. 2016), 2616–2627.

[135] Němec, P., Nazabal, V., and Frumar, M. **Photoinduced phenomena in amorphous As4se3 pulsed laser deposited thin films studied by spectroscopic ellipsometry**. *Journal of Applied Physics 106*, 2 (July 2009), 023509.

[136] Meneghini, C., and Villeneuve, A. **As_2S_3 photosensitivity by two-photon absorption: holographic gratings and self-written channel waveguides**. *JOSA B 15*, 12 (Dec. 1998), 2946–2950.

[137] Shimakawa, K., Kolobov, A., and Elliott, S. R. **Photoinduced effects and metastability in amorphous semiconductors and insulators**. *Advances in Physics 44*, 6 (Dec. 1995), 475–588.

[138] Youden, K. E., Grevatt, T., Eason, R. W., Rutt, H. N., Deol, R. S., and Wylangowski, G. **Pulsed laser deposition of Ga-La-S chalcogenide glass thin film optical waveguides**. *Applied Physics Letters 63*, 12 (Sept. 1993), 1601–1603.

[139] Tikhomirov, V. K., and Elliott, S. R. **The anisotropic photorefractive effect in bulk As 2 S 3 glass induced by polarized subgap laser light**. *Journal of Physics: Condensed Matter 7*, 8 (1995), 1737.

[140] Owen, A. E., Firth, A. P., and Ewen, P. J. S. **Photo-induced structural and physico-chemical changes in amorphous chalcogenide semiconductors**. *Philosophical Magazine Part B 52*, 3 (Sept. 1985), 347–362.

[141] Olivier, M., Němec, P., Boudebs, G., Boidin, R., Focsa, C., and Nazabal, V. **Photosensitivity of pulsed laser deposited Ge-Sb-Se thin films**. *Optical Materials Express 5*, 4 (Apr. 2015), 781.

[142] Němec, P., Zhang, S., Nazabal, V., Fedus, K., Boudebs, G., Moreac, A., Cathelinaud, M., and Zhang, X.-H. **Photo-stability of pulsed laser deposited $Ge_xAs_ySe_{100\text{-}x\text{-}y}$ amorphous thin films**. *Optics Express 18*, 22 (Oct. 2010), 22944–22957.

[143] Shen, W. D., Cathelinaud, M., Lequime, M., Charpentier, F., and Nazabal, V. **Light trimming of a narrow bandpass filter based on a photosensitive chalcogenide spacer**. *Optics Express 16*, 1 (Jan. 2008), 373–383.

[144] Ohmachi, Y. **Acousto-optical light diffraction in thin films**. *Journal of Applied Physics 44*, 9 (Sept. 1973), 3928–3933.

[145] DeCorby, R. G., Ponnampalam, N., Pai, M. M., Nguyen, H. T., Dwivedi, P. K., Clement, T. J., Haugen, C. J., McMullin, J. N., and Kasap, S. O. **High index contrast waveguides in chalcogenide glass and polymer**. *IEEE Journal of Selected Topics in Quantum Electronics 11*, 2 (Mar. 2005), 539–546.

[146] Charrier, J., Brandily, M.-L., Lhermite, H., Michel, K., Bureau, B., Verger, F., and Nazabal, V. **Evanescent wave optical micro-sensor based on chalcogenide glass**. *Sensors and Actuators B: Chemical 173* (Oct. 2012), 468–476.

[147] j, T., V, L., and R, T. **Linear and non-linear optical properties of GeS2 doped with the elements from III and V group of the periodic table**. *Bulgarian Chemical Communications Volume 45*, Special Issue B (2013), (pp. 33–37).

[148] Olivier, M., Tchahame, J., Němec, P., Chauvet, M., Besse, V., Cassagne, C., Boudebs, G., Renversez, G., Boidin, R., Baudet, E., and Nazabal, V. **Structure, nonlinear properties, and photosensitivity of (GeSe_2)_100-x(Sb_2se_3)_x glasses**. *Optical Materials Express 4*, 3 (Mar. 2014), 525.

[149] Paivasaari, K., Tikhomirov, V. K., and Turunen, J. **High refractive index chalcogenide glass for photonic crystal applications**. *Optics Express 15*, 5 (Mar. 2007), 2336–2340.

[150] Vo, T. D., Pelusi, M. D., Schröder, J., Luan, F., Madden, S. J., Choi, D.-Y., Bulla, D. a. P., Luther-Davies, B., and Eggleton, B. J. **Simultaneous multi-impairment monitoring of 640 Gb/s signals using photonic chip based RF spectrum analyzer**. *Optics Express 18*, 4 (Feb. 2010), 3938–3945.

[151] Erps, J. V., Luan, F., Pelusi, M. D., Iredale, T., Madden, S., Choi, D.-Y., Bulla, D. A., Luther-Davies, B., Thienpont, H., and Eggleton, B. J. **High-Resolution Optical Sampling of 640-Gb/s Data Using Four-Wave Mixing in Dispersion-Engineered Highly Nonlinear As$_2$S$_3$ Planar Waveguides**. *Journal of Lightwave Technology 28*, 2 (Jan. 2010), 209–215.

[152] Pelusi, M. D., Luan, F., Madden, S., Choi, D. Y., Bulla, D. A., Luther-Davies, B., and Eggleton, B. J. **Wavelength Conversion of High-Speed Phase and Intensity Modulated Signals Using a Highly Nonlinear Chalcogenide Glass Chip**. *IEEE Photonics Technology Letters 22*, 1 (Jan. 2010), 3–5.

[153] Vo, T. D., Pant, R., Pelusi, M. D., Schröder, J., Choi, D.-Y., Debbarma, S. K., Madden, S. J., Luther-Davies, B., and Eggleton, B. J. **Photonic chip-based all-optical XOR gate for 40 and 160 Gbit/s DPSK signals**. *Optics Letters 36*, 5 (Mar. 2011), 710–712.

[154] Nguyen, H. C., Finsterbusch, K., Moss, D. J., and Eggleton, B. J. **Dispersion in nonlinear figure of merit of As2se3 chalcogenide fibre**. *Electronics Letters 42*, 10 (May 2006), 571–572.

[155] Lenz, G., Zimmermann, J., Katsufuji, T., Lines, M. E., Hwang, H. Y., Spälter, S., Slusher, R. E., Cheong, S.-W., Sanghera, J. S., and Aggarwal, I. D. **Large Kerr effect in bulk Se-based chalcogenide glasses**. *Optics Letters 25*, 4 (Feb. 2000), 254–256.

[156] Hilton, A. R. **Optical properties of chalcogenide glasses**. *Journal of Non-Crystalline Solids 2* (Jan. 1970), 28–39.

[157] Kanbara, H., Fujiwara, S., Tanaka, K., Nasu, H., and Hirao, K. **Third-order nonlinear optical properties of chalcogenide glasses**. *Applied Physics Letters 70*, 8 (Feb. 1997), 925–927.

[158] Bagrov, A. M., Baĭkalov, P. I., Vasil'ev, A. V., Devyatykh, G. G., Dianov, E. M., Plotnichenko, V. G., Skripachev, I. V., Sysoev, V. K., and Churbanov, M. F. **Fiber waveguides for the middle infrared range made of As–S and As–Se glasses with optical losses below 1 dB/m**. *Soviet Journal of Quantum Electronics 13*, 9 (1983), 1264.

[159] Gopinath, J. T., Soljačić, M., Ippen, E. P., Fuflyigin, V. N., King, W. A., and Shurgalin, M. **Third order nonlinearities in Ge-As-Se-based glasses for telecommunications applications**. *Journal of Applied Physics 96*, 11 (Nov. 2004), 6931–6933.

[160] Petit, L., Carlie, N., Adamietz, F., Couzi, M., Rodriguez, V., and Richardson, K. C. **Correlation between physical, optical and structural properties of sulfide glasses in the system Ge–Sb–S**. *Materials Chemistry and Physics 97*, 1 (May 2006), 64–70.

[161] Chauvet, M., Fanjoux, G., Huy, K. P., Nazabal, V., Charpentier, F., Billeton, T., Boudebs, G., Cathelinaud, M., and Gorza, S.-P. **Kerr spatial solitons in chalcogenide waveguides**. *Optics Letters 34*, 12 (June 2009), 1804–1806.

[162] Nazabal, V., Charpentier, F., Adam, J.-L., Nemec, P., Lhermite, H., Brandily-Anne, M.-L., Charrier, J., Guin, J.-P., and Moréac, A. **Sputtering and Pulsed Laser Deposition for Near- and Mid-Infrared Applications: A Comparative Study of Ge25sb10s65 and Ge25sb10se65 Amorphous Thin Films: Sputtering and Pulsed Laser Deposition for Near- and Mid-IR Applications**. *International Journal of Applied Ceramic Technology 8*, 5 (Sept. 2011), 990–1000.

[163] Němec, P., Olivier, M., Baudet, E., Kalendová, A., Benda, P., and Nazabal, V. **Optical properties of (GeSe2)100-x(Sb2se3)x glasses in near- and middle-infrared spectral regions**. *Materials Research Bulletin 51* (Mar. 2014), 176–179.

[164] Li, J., Shen, X., Sun, J., Vu, K., Choi, D.-Y., Wang, R., Luther-Davies, B., Dai, S., Xu, T., and Nie, Q. **Fabrication and characterization of Ge20sb15se65 chalcogenide glass rib waveguides for telecommunication wavelengths**. *Thin Solid Films 545* (Oct. 2013), 462–465.

[165] Gai, X., Madden, S., Choi, D.-Y., Bulla, D., and Luther-Davies, B. **Dispersion engineered $Ge_{11.5}As_{24}Se_{64.5}$ nanowires with a nonlinear parameter of $136w^{-1}m^{-1}$ at 1550nm**. *Optics Express 18*, 18 (Aug. 2010), 18866–18874.

[166] Baudet, E. **Micro-capteurs optiques fonctionnant dans l'infrarouge pour la détection de polluants émergents en eaux souterraines et marines**. PhD thesis, Université de Rennes 1, Rennes, France, 2015.

[167] Sharma, P., and Katyal, S. C. **Effect of deposition parameters on the optical energy gap and refractive index of a-Ge–Se–Te thin films**. *Philosophical Magazine 88*, 17 (June 2008), 2549–2557.

[168] Dai, S., Chen, F., Xu, Y., Xu, Z., Shen, X., Xu, T., Wang, R., and Ji, W. **Mid-infrared optical nonlinearities of chalcogenide glasses in Ge-Sb-Se ternary system**. *Optics Express 23*, 2 (Jan. 2015), 1300.

[169] Wang, T., Gai, X., Wei, W., Wang, R., Yang, Z., Shen, X., Madden, S., and Luther-Davies, B. **Systematic z-scan measurements of the third order nonlinearity of chalcogenide glasses**. *Optical Materials Express 4*, 5 (May 2014), 1011.

[170] Chen, L., Chen, F., Dai, S., Tao, G., Yan, L., Shen, X., Ma, H., Zhang, X., and Xu, Y. **Third-order nonlinearity in Ge–Sb–Se glasses at mid-infrared wavelengths**. *Materials Research Bulletin 70* (Oct. 2015), 204–208.

[171] Krogstad, M. R., Ahn, S., Park, W., and Gopinath, J. T. **Nonlinear characterization of Ge_28sb_12se_60 bulk and waveguide devices**. *Optics Express 23*, 6 (Mar. 2015), 7870.

[172] Huang, C. C., Hewak, D. W., and Badding, J. V. **Deposition and characterization of germanium sulphide glass planar waveguides**. *Optics Express 12*, 11 (May 2004), 2501–2506.

[173] González-Leal, J. M., Ledesma, A., Bernal-Oliva, A. M., Prieto-Alcón, R., Márquez, E., Angel, J. A., and Cárabe, J. **Optical properties of thin-film ternary Ge10as15se75 chalcogenide glasses**. *Materials Letters 39*, 4 (May 1999), 232–239.

[174] Charrier, J., Anne, M. L., Lhermite, H., Nazabal, V., Guin, J. P., Charpentier, F., Jouan, T., Henrio, F., Bosc, D., and Adam, J. L. **Sulphide GaxGe25-xSb10s65(x=0,5) sputtered films: Fabrication and optical characterizations of planar and rib optical waveguides**. *Journal of Applied Physics 104*, 7 (Oct. 2008), 073110.

[175] Magnetron Sputtering Technology, http://www.directvacuum.com/pdf/what_is_sputtering.pdf.

[176] WOOLLAM, J. A., JOHS, B. D., HERZINGER, C. M., HILFIKER, J. N., SYNOWICKI, R. A., AND BUNGAY, C. L. Overview of variable-angle spectroscopic ellipsometry (VASE): I. Basic theory and typical applications. In *SPIE* (July 1999), vol. 10294, International Society for Optics and Photonics, p. 1029402.

[177] WOOLLAM CO, J. A. Ellipsometry Measurements,https://www.jawoollam.com /resources/ellipsometry-tutorial/ellipsometry-measurements.

[178] CODY, G. D. Chapter 2 The Optical Absorption Edge of a-Si: H. In *Semiconductors and Semimetals*, J. I. Pankove, Ed., vol. 21 of *Hydrogenated Amorphous Silicon*. Elsevier, Jan. 1984, pp. 11–82.

[179] BAUDET, E., CARDINAUD, C., GIRARD, A., RINNERT, E., MICHEL, K., BUREAU, B., AND NAZABAL, V. Structural analysis of RF sputtered Ge-Sb-Se thin films by Raman and X-ray photoelectron spectroscopies. *Journal of Non-Crystalline Solids 444* (July 2016), 64–72.

[180] HUNSPERGER, R. G. Losses in Optical Waveguides. In *Integrated Optics*. Springer, New York, NY, 2009, pp. 107–128. DOI: 10.1007/b98730_6.

[181] TONG, X. C. Characterization Methodologies of Optical Waveguides. In *Advanced Materials for Integrated Optical Waveguides*, Springer Series in Advanced Microelectronics. Springer, Cham, 2014, pp. 53–102. DOI: 10.1007/978-3-319-01550-7_2.

[182] DRIVER, R. D., LESKOWITZ, G. M., CURTISS, L. E., MOYNIHAN, D. E., AND VACHA, L. B. The characterization of infrared transmitting optical fibers. *MRS Online Proceedings Library Archive 172* (1989).

[183] WATTS, R. K., DE WIT, M., AND HOLTON, W. C. Nonoxide chalcogenide glass films for integrated optics. *Applied optics 13*, 10 (1974), 2329–2332.

[184] LIANG, T.-K., AND TSANG, H.-K. Nonlinear absorption and Raman scattering in silicon-on-insulator optical waveguides. *IEEE Journal of Selected Topics in Quantum Electronics 10*, 5 (Sept. 2004), 1149–1153.

[185] SUTHERLAND, R. L. Handbook of Nonlinear Optics, 2 edition ed. CRC Press, New York, NY, Apr. 2003.

[186] RUMI, M., AND PERRY, J. W. Two-photon absorption: an overview of measurements and principles. *Advances in Optics and Photonics 2*, 4 (Dec. 2010), 451.

[187] Petit, L., Carlie, N., Chen, H., Gaylord, S., Massera, J., Boudebs, G., Hu, J., Agarwal, A., Kimerling, L., and Richardson, K. **Compositional dependence of the nonlinear refractive index of new germanium-based chalcogenide glasses**. *Journal of Solid State Chemistry 182*, 10 (Oct. 2009), 2756–2761.

[188] Tseng, K. Y., and Wong, K. S. **Femtosecond time-resolved Z-scan measurements of optical nonlinearities in solids and liquids**. In *Quantum Electronics and Laser Science Conference (1995), paper QWD13* (May 1995), Optical Society of America, p. QWD13.

[189] Asobe, M., Suzuki, K., Kanamori, T., and Kubodera, K. **Nonlinear refractive index measurement in chalcogenide-glass fibers by self-phase modulation**. *Applied Physics Letters 60*, 10 (Mar. 1992), 1153–1154.

[190] Boudebs, G., Chis, M., and Phu, X. N. **Third-order susceptibility measurement by a new Mach–Zehnder interferometry technique**. *JOSA B 18*, 5 (2001), 623–627.

[191] Tanaka, K. **Two-photon absorption spectroscopy of As2s3 glass**. *Applied Physics Letters 80*, 2 (Jan. 2002), 177–179.

[192] Asobe, M., Kanamori, T., and Kubodera, K. **Ultrafast all-optical switching using highly nonlinear chalcogenide glass fiber**. *IEEE photonics technology letters 4*, 4 (1992), 362–365.

[193] Sheik-Bahae, M., Said, A. A., Wei, T.-H., Hagan, D. J., and Van Stryland, E. W. **Sensitive measurement of optical nonlinearities using a single beam**. *IEEE journal of quantum electronics 26*, 4 (1990), 760–769.

[194] Ule, E. **Measurement of The Nonlinear Refractive Index by Z-scan Technique**. Tech. rep., University of Ljubljana, Slovenia, 2015.

[195] Nalda, R. d., Coso, R. d., Requejo-Isidro, J., Olivares, J., Suarez-Garcia, A., Solis, J., and Afonso, C. N. **Limits to the determination of the nonlinear refractive index by the Z-scan method**. *JOSA B 19*, 2 (Feb. 2002), 289–296.

[196] Thylen, L. **The beam propagation method: an analysis of its applicability**. *Optical and quantum electronics 15*, 5 (1983), 433–439.

[197] Falconieri, M., and Salvetti, G. **Simultaneous measurement of pure-optical and thermo-optical nonlinearities induced by high-repetition-rate, femtosecond laser pulses: application to CS2**. *Applied Physics B 69*, 2 (Aug. 1999), 133–136.

[198] Burkins, P., Kuis, R., Basaldua, I., Johnson, A. M., Swaminathan, S. R., Zhang, D., and Trivedi, S. **Thermally managed Z-scan methods investigation of the size-dependent nonlinearity of graphene oxide in various solvents**. *JOSA B 33*, 11 (Nov. 2016), 2395–2401.

[199] Gnoli, A., Razzari, L., and Righini, M. **Z-scan measurements using high repetition rate lasers: how to manage thermal effects**. *Optics Express 13*, 20 (Oct. 2005), 7976–7981.

[200] Akhmediev, N. N., and Ankiewicz, A. **Solitons : nonlinear pulses and beams / Nail N. Akhmediev and Adrian Ankiewicz**. Optical and quantum electronics series ; 5. Chapman & Hall, London ; New York, 1997.

[201] Silberberg, Y. **Solitons and two-photon absorption**. *Optics Letters 15*, 18 (Sept. 1990), 1005–1007.

[202] Choi, J. W., Han, Z., Sohn, B.-U., Chen, G. F. R., Smith, C., Kimerling, L. C., Richardson, K. A., Agarwal, A. M., and Tan, D. T. H. **Nonlinear characterization of GeSbS chalcogenide glass waveguides**. *Scientific Reports 6*, 1 (Dec. 2016).

[203] Harbold, J. M., Ilday, F. ., Wise, F. W., Sanghera, J. S., Nguyen, V. Q., Shaw, L. B., and Aggarwal, I. D. **Highly nonlinear As–S–Se glasses for all-optical switching**. *Optics Letters 27*, 2 (Jan. 2002), 119–121.

[204] Baudet, E., Sergent, M., Němec, P., Cardinaud, C., Rinnert, E., Michel, K., Jouany, L., Bureau, B., and Nazabal, V. **Experimental design approach for deposition optimization of RF sputtered chalcogenide thin films devoted to environmental optical sensors**. *Scientific Reports 7*, 1 (Dec. 2017).

[205] Kuriakose, T., Baudet, E., Halenkovič, T., Elsawy, M. M. R., Němec, P., Nazabal, V., Renversez, G., and Chauvet, M. **Measurement of ultrafast optical Kerr effect of Ge–Sb–Se chalcogenide slab waveguides by the beam self-trapping technique**. *Optics Communications 403*, Supplement C (Nov. 2017), 352–357.

[206] Zheltikov, A. M. **Let there be white light: supercontinuum generation by ultrashort laser pulses**. *Physics-Uspekhi 49*, 6 (2006), 605.

[207] Lin, Y.-Y., Lee, R.-K., and Kivshar, Y. S. **Transverse instability of transverse-magnetic solitons and nonlinear surface plasmons**. *Optics Letters 34*, 19 (Oct. 2009), 2982–2984.

[208] MALENDEVICH, R., JANKOVIC, L., STEGEMAN, G., AND AITCHISON, J. S. **Spatial modulation instability in a Kerr slab waveguide**. *Optics Letters 26*, 23 (Dec. 2001), 1879–1881.

[209] GRIGORENKO, A. N., POLINI, M., AND NOVOSELOV, K. S. **Graphene plasmonics**. *Nature Photonics 6*, 11 (Nov. 2012), 749–758.

LIST OF FIGURES

LIST OF TABLES

Document generated with LaTeX and:
the LaTeX style for PhD Thesis created by S. Galland — http://www.multiagent.fr/ThesisStyle
the `tex-upmethodology` package suite — http://www.arakhne.org/tex-upmethodology/

Titre : Démonstration de l'autofocalisation d'une onde plasmonique

Mots clés : Optique nonlinéaire, Plasmonique, Solitons spatiaux Kerr, Guide plan en chalcogénure

Résumé : Cette thèse est une contribution au domaine de recherche de la plasmonique nonlinéaire, domaine émergent de l'optique. L'objectif principal est de démontrer expérimentalement l'autofocalisation d'une onde plasmonique.

L'étude débute avec la fabrication et la caractérisation de guides plans en verre de chalcogénure de composition Ge-Sb-Se. Une technique basée sur la formation de solitons spatiaux est développée afin d'estimer leurs non-linéarités Kerr. Les propriétés optiques linéaires et non linéaires de ces guides sont étudiées aux longueurs d'onde de 1200 nm et 1550 nm.

Des structures plasmoniques sont ensuite conçues pour propager des ondes hybrides plasmon-solitons avec des pertes de propagation modérées. Elles sont constituées des guides précédents recouverts de nanocouches de silice et d'or.

Les caractérisations optiques par couplage plasmon-soliton révèlent une forte autofocalisation subie par l'onde qui se propage à l'intérieur de la structure plasmonique. Comme prévu par la théorie, le comportement est présent uniquement pour une lumière polarisée TM. Des résultats expérimentaux détaillés de cette autofocalisation exaltée par effet plasmonique sont présentés pour différentes configurations. Des simulations confirment les résultats expérimentaux obtenus.

Cette démonstration fondamentale vient confirmer le concept d'autofocalisation assistée par plasmon tout en révélant un effet nonlinéaire très efficace. Cela ouvre de nouvelles perspectives pour le développement de dispositifs photoniques non linéaires intégrés ainsi que de nouveaux phénomènes physiques.

Title: Demonstration of the spatial self-trapping of a plasmonic wave

Keywords: Nonlinear optics, Plasmonics, Kerr spatial solitons, Planar chalcogenide waveguides

Abstract: This dissertation contributes to the research area of nonlinear plasmonics an emerging field of optics. The main goal is to demonstrate experimentally the spatial self-trapping of a plasmonic wave.

The study begins with the fabrication and the characterization of slab Ge-Sb-Se chalcogenide waveguides. A technique based on the formation of spatial solitons is developed to estimate their Kerr nonlinearities. Linear and nonlinear optical properties of the waveguides are studied at the wavelengths of 1200 nm and 1550 nm.

Plasmonic structures are then designed to propagate hybrid plasmon-soliton waves with moderate propagation losses. They are constituted of the previous waveguides covered with nanolayers of silica and gold.

Optical characterizations reveal a giant self-focusing undergone by the wave that propagates inside the plasmonic structure. The behavior is present only for TM polarized light as expected from theory. Detailed experimental results of this plasmon enhanced nonlinear self-trapping corresponding to different configurations are presented. Simulations confirm the obtained experimental results.

This fundamental demonstration confirms the concept of plasmon-assisted self-focusing while revealing a very efficient nonlinear effect. This opens new perspectives for the development of integrated nonlinear photonic devices as well as new physical phenomena.

Université Bourgogne Franche-Comté
32, avenue de l'Observatoire
25000 Besançon